



저작자표시-비영리-변경금지 2.0 대한민국

이용자는 아래의 조건을 따르는 경우에 한하여 자유롭게

- 이 저작물을 복제, 배포, 전송, 전시, 공연 및 방송할 수 있습니다.

다음과 같은 조건을 따라야 합니다:



저작자표시. 귀하는 원저작자를 표시하여야 합니다.



비영리. 귀하는 이 저작물을 영리 목적으로 이용할 수 없습니다.



변경금지. 귀하는 이 저작물을 개작, 변형 또는 가공할 수 없습니다.

- 귀하는, 이 저작물의 재이용이나 배포의 경우, 이 저작물에 적용된 이용허락조건을 명확하게 나타내어야 합니다.
- 저작권자로부터 별도의 허가를 받으면 이러한 조건들은 적용되지 않습니다.

저작권법에 따른 이용자의 권리는 위의 내용에 의하여 영향을 받지 않습니다.

이것은 [이용허락규약\(Legal Code\)](#)을 이해하기 쉽게 요약한 것입니다.

[Disclaimer](#)

Ph.D. THESIS

Real-time Hybrid Simulation System for the
Aeroelastic Phenomena of the Bridge Deck

교량데크 공탄성 현상 재현을 위한
실시간 하이브리드 시뮬레이션 시스템

2019 년 8 월

서울대학교 대학원

건설환경공학부

황 유 찬

ABSTRACT

Hybrid Simulation System for the Aeroelastic Phenomena of the Bridge Deck

You Chan Hwang

Department of Civil and Environmental Engineering

Seoul National University

To overcome the technical challenges in numerical analysis over the responses of the wind-structure interactions, the dynamic response of long-span bridges subjected to wind loads has been primarily evaluated through appropriate wind tunnel tests. The wind tunnel tests, especially spring-supported tests, require calibration of springs, masses, and the damping properties of an experimental specimen. This calibration work requires considerable time and efforts. In fact, it is impossible to set up the experimental processes to precisely meet the target value.

To solve this issue, the following approach is newly proposed in this dissertation. The hybrid simulation approach mainly applied to simulate the vibration issues for the earthquake events have certain advantages to assess the responses of the winds. In this hybrid simulation, noted as the Real-time Hybrid Simulation(RTHS) system, a numerical model and a physical specimen are tightly integrated. Then, a component that is difficult to be represented with a traditional numerical model is assessed experimentally, while the rest

of the structural system is analyzed numerically. In this dissertation, designs and validation of experimental apparatus for the RTHS system to simulate wind tunnel tests are developed. The experimental apparatus, composed with four linear motors, is designed for the section model tests for a long-span bridge.

Before developing the real RTHS system, it is necessary to verify the feasibility of the RTHS system. For this mission, using the numerical simulation method, the RTHS system is simulated. Then, the results are verified with the results from the traditional aeroelastic analysis. Results show the good agreement between two approaches. It leads to the conclusion that the RTHS system is a feasible option to assess the responses of the system by winds.

The proposed RTHS system is composed of two features; one for the proper hardware development and the other for software applications. For a comprehensive design of the proposed system, the integration of the key hardware components such as a linear motor, a load cell, and a frame system is needed. To identify the proper capacity of experimental apparatus, the numerical analyses are performed. In this study, the actual cross sections from Mankyung Bridge and Old Tacoma Bridge are applied for the worst-case scenario analysis. In this extreme case study, the maximum values of the displacements and forces are used to set the capacity of experimental apparatus. The results show that the maximum displacement in the vertical direction is 50 mm and the maximum load per each motor is 408 N.

For the optimum control program, the numerical integration loop, the time-delay compensation loop, and the PID loop are systematically inter-linked. The central difference approximation method is applied for the numerical integration. To avoid any potential numerical diverges, the time step for controls is set to be 5 ms through the experiments. The total time-delay of the proposed RTHS system is 34 ms. To reduce errors caused by time-delay, the adaptive compensation approach proposed by Chen(2009, 2010; 2012) is applied.

To identify the available range of input parameter values in the proposed RTHS system, the series of test cases are performed with the different input values of the key parameters such as the mass, the damping ratio, and the natural frequency. The validity of the experiments is checked with realized damping, frequency, and the relative root mean square error(rRMSE) values with displacement values from the numerical studies.

Finally, to assure the validity of the proposed RTHS system, the combinations of the analytical force simulations and experiments are performed. Three different test cases are proposed for this final validation. The sinusoidal and the white noise forces are numerically added in the control program as a virtual force to simulate the responses of the vortex-induced and buffeting vibrations respectively. Results indicate that there is good agreement between the analytical values from the numerical analysis and the actual measured values from the RTHS system. Results give an additional credit to prove the validity of the proposed RTHS system for the wind tunnel tests.

Keywords: Real-Time Hybrid Simulation; Bridge Deck; Wind Tunnel Test;
Aeroelastic Analysis; Time-Delay Compensation

Student Number: 2011-21008

TABLE OF CONTENTS

1. INTRODUCTION	1
1.1 Key Issues in a Current Wind Tunnel Test	1
1.2 Motivation of the New Approach: Application of a Hybrid Simulation Method in Other Studies.....	8
1.3 Application of the RTHS System to Wind Tunnel Tests	9
2. FEASIBILITY STUDIES FOR THE PROPOSED RTHS SYSTEM.....	12
2.1 Numerical Simulation Methods for a Feasibility Study of the RTHS System	12
2.2 Time Domain Analysis Method to Estimate Wind-induced Forces in a Numerical Simulation Method and an Aeroelastic Analysis	15
2.3 Cases for Feasibility Studies of the RTHS System	20
2.3.1 Analysis Conditions for the Case Studies.....	20
2.3.2 Analysis Results	23
3. DESIGN AND CONSTRUCTION OF HARDWARE AND SOFTWARE FOR THE RTHS SYSTEM.....	26
3.1 Design of Hardware Components of the RTHS System	26
3.1.1 Methods for Describing the 2DOF Motion in the RTHS System	26
3.1.2 Numerical Analysis Conditions.....	28
3.1.3 Analysis Results	31

3.1.4 Selection of the Experimental Apparatus	34
3.2 Development of the Control Software of the RTHS System.....	39
3.2.1 The Schematic of the Control Software	39
3.2.2 Numerical Integration Loops.....	41
3.2.3 Time-delay Compensation Methods.....	44
4. VERIFICATION OF THE APPLICABLE RANGE OF THE RTHS SYSTEM	54
4.1 Determination of the Target Range of Input Variables in the RTHS Process.....	54
4.2 Preliminary Tests for Setting the Feasible Conditions of the RTHS System	57
4.2.1 Objects and Analysis Methods for Preliminary Tests	57
4.2.2 Experimental Results with Given Mass Ratios	58
4.2.3 Experimental Results with Target Damping	62
4.2.4 Experimental Results with Given Target Frequencies	66
4.2.5 Experimental Results with Different Values of Frequency Ratio in the 2DOF Movement.....	70
4.2.6 Analyses of the Results in Terms of the Velocity of the RTHS System	74
5. SIMULATION OF THE VIBRATION IN WIND TUNNEL TESTS	77
5.1 Design of Three Experimental Cases for Simulating the Vibration in Wind Tunnel Tests	77

5.2 Simulation Cases (1): Free-vibration Tests.....	79
5.3 Simulation Cases (2): Sinusoidal Force Excitation Tests	83
5.4 Simulation Cases (3): White Noise Force Excitation Tests.....	85
CONCLUSIONS AND RECOMMENDATIONS FOR FURTHER STUDY	
.....	88
REFERENCES	91

LIST OF FIGURES

Figure 1. A Spring Support System	7
Figure 2. Changes in Damping Ratio by Vibration Magnitudes in a Section Model Tests.....	7
Figure 3. The Concept of the Application of the RTHS System in the Wind Tunnel Tests	11
Figure 4. Concept of the Numerical Hybrid Simulation Method	13
Figure 5. Deck Section Shape of the 2 nd Jindo Bridge	20
Figure 6. Time Series of the Generated Wind Data (b) Comparison of the Von Karman Spectrum and the Spectrum of the Generated Wind...21	
Figure 7. (a) Aerostatic Coefficients and (b) Flutter Derivatives of 2 nd Jindo Bridge Obtained by Experiments	22
Figure 8. Wind-induced force for Different Noise Ratios at 5 m/s Wind Speed (a) Lift Force and (b) Moment.....	22
Figure 9. Analysis Results at 5 m/s (Noise Ratio = 10%) (a)Vertical Response at 0 to 60 sec (b)Torsional Response at 0 to 60 sec (c)Vertical Response at 30 to 35 sec (d) Torsional Response at 30 to 35 sec	23
Figure 10. Analysis Results at 15 m/s (Noise Ratio = 10%) (a)Vertical Response at 0 to 60 sec (b)Torsional Response at 0 to 60 sec (c)Vertical Response at 30 to 15 sec (d) Torsional Response at 30 to 35 sec	24

Figure 11. (a) Vertical Direction Movement (b) Torsional Direction Movement in the RTHS System	26
Figure 12. Details about Rotational Joint and Force Measurement Part in the RTHS System	27
Figure 13. Target Bridge Section (a) TN Bridge (b) MK Bridge Section	30
Figure 14. Analysis Results for Case 3: (a) Vertical Displacement (b) Torsional Displacement (c) Vertical Velocity (d) Torsional Velocity (e) Vertical Acceleration (f) Torsional Acceleration...	31
Figure 15. Force Results in Case 4: (a) Lift force (b) Moment	33
Figure 16. Variation of Linear Motor Target Displacements by Different R Values	34
Figure 17. Maximum Values by Different R Values: (a) Displacement (b) Velocity (c) Acceleration	35
Figure 18. Manufactured Linear Motor	35
Figure 19. Selected Load Cell (Futek, MBA400)	36
Figure 20. Frame System of the RTHS System.....	37
Figure 21. Frame Used for a Dynamic Analysis	38
Figure 22. Frame Shape and Mesh Setup in the ANSYS Program	38
Figure 23. Harmonic Response Result	39
Figure 24. Schematic of the Control Program.....	40
Figure 25. Concept of Time-Delay Compensation Methods Proposed by C. Chen and Ricles (2009)	45
Figure 26. Setup for Verifying System Operation	48

Figure 27. Comparison of Target and Measured Displacements before Applying the Compensation Method (a) 0~60 sec Region (b) 0~2 sec Region (c) 50~52 sec Region	49
Figure 28. Bode Plots (a) Magnitude (b) Phase.....	49
Figure 29. Comparison of Target and Measured Displacement Values after Applying the Compensation Method (a) 0~60 sec Region (b) 0~2 sec Region (c) 50~52 sec Region	51
Figure 30. The Possible Process Causing a Time-Delay in a Control Program	52
Figure 31. Measurement of the Time-Lag between the Host PC and the PID Loop Using the ACR Program.....	52
Figure 32. Results of Phase Analysis to Identify the Time-Delay by the 2nd Factor	53
Figure 33. The Window of the LabVIEW Program to Run the Cases for the RTHS System	55
Figure 34. Illustration of the System Components Determining the Experimental Mass of the RTHS System	56
Figure 35. Displacements in the Vertical Direction for Different Values of mR	59
Figure 36. Realized Damping Ratios in the Vertical Direction for Different Values of mR for a Given Target Damping Ratio of 0.6 %....	60
Figure 37. rRMSE in the Vertical Direction for Different Values of mR for a Given Target Damping Ratio of 0.6 %	60

Figure 38. Responses in the Torsional Displacements for Different IR	61
Figure 39. Responses in the Realized Damping Ratios for Different IR in the Torsional Direction for a Given Target Damping Ratio of 0.6 %	62
Figure 40. rRMSE in the Realized Damping Ratios for Different IR in the Torsional Direction for a Given Target Damping Ratio of 0.6 %	62
Figure 41. Responses in Displacements for Different Target Damping Ratios in the Vertical Direction.....	63
Figure 42. Responses in Realized Damping Ratios for Different Target Damping Ratios in the Vertical Direction.....	64
Figure 43. rRMSE for Different Target Damping Ratios in the Vertical Direction	64
Figure 44. Responses in Displacements for Different Target Damping Ratios in the Torsional Direction	65
Figure 45. Realized Damping Ratios for Different Target Damping Ratios in the Torsional Direction	65
Figure 46. rRMSE Values for Different Target Damping Ratios in the Torsional Direction	66
Figure 47. Responses in Vertical Displacements for Different Target Vertical Frequencies.....	67

Figure 48. Realized Damping Ratios for Different Target Frequencies in the Vertical Direction for a Given Target Damping Ratio of 0.6 %	67
Figure 49. rRMSE Values for Different Target Frequencies in the Vertical Direction for a Given Target Damping Ratio of 0.6 %.....	68
Figure 50. Responses in Displacements for Different Target Frequencies in the Torsional Direction	69
Figure 51. Realized Damping Ratios for Different Target Frequencies in the Torsional Direction for a Given Target Damping Ratio of 0.6 %	69
Figure 52. rRMSE Values for Different Target Frequencies in the Torsional Direction for a Given Target Damping Ratio of 0.6 %.....	70
Figure 53. Responses in Displacements for Different fR in the Vertical Direction	71
Figure 54. Responses in Torsional Displacements for Different fR	71
Figure 55. Realized Damping Ratios for Different fR Frequencies for a Given Target Damping Ratio of 0.6 % (a) in the Vertical Direction and (b) in the Torsional Direction.....	73
Figure 56. rRMSE Values for Different fR Frequencies for a Given Target Damping Ratio of 0.6 % (a) in the Vertical Direction and (b) in the Torsional Direction	73
Figure 57. Velocities in the Vertical Direction for Different Values of mR	75

Figure 58. Responses in Velocities for Different Target Damping Ratios in the Vertical Direction.....	75
Figure 59. rRMSE Values in Terms of Velocities for Different Values of mR for a Given Target Damping Ratios of 0.6 % in the Vertical Direction	76
Figure 60. rRMSE Values in Terms of Velocities for Different Target Damping Ratios in the Vertical Direction	76
Figure 61. General Velocity-Amplitude Curves Attained in the Wind Tunnel Experiments	77
Figure 62. Setup for Simulation Tests	78
Figure 63. Comparison of Analytical and Measured Vertical Displacements in the Free-Vibration Tests (Initial Displacement)	80
Figure 64. Comparison of Analytical and Measured Torsional Displacements in the Free-Vibration Tests (Initial Displacement)	81
Figure 65. Comparison of Analytical and Measured Vertical Displacements in the Free-Vibration Tests (Initial Velocity)	82
Figure 66. Comparison of Analytical and Measured Torsional Displacements in the Free-Vibration Tests (Initial Velocity)	82
Figure 67. Comparison of Analytical and Measured Vertical Displacements in the Sinusoidal Excitation Tests.....	84
Figure 68. Comparison of Analytical and Measured Torsional Displacements in the Sinusoidal Excitation Tests.....	84

Figure 69. White Noise Signals for Simulation Case 3 (a) Lift Force (b)	
Moment.....	86
Figure 70. Comparison of Analytical and Measured Vertical Displacements	
in the White Noise Excitation Tests.....	86
Figure 71. Comparison of Analytical and Measured Torsional Displacements	
in the White Noise Excitation Tests.....	87

LIST OF TABLES

Table 1. Dynamic Properties of 2nd Jindo Bridge Section Model	20
Table 2. rRMSE between Results from Aeroelastic Analyses and Numerical Simulations	25
Table 3. Dynamic Properties of an Actual Bridges Section Model for Wind Tunnel Tests	28
Table 4. Dynamic Parameters for Numerical Analysis Case	30
Table 5. Maximum Values in the Numerical Analysis Results	32
Table 6. Maximum and Minimum Forces at Each Analysis Case	33
Table 7. Comparison of Transmissibility for Different Time Steps	43

ABBREVIATIONS

RTHS	Real-time Hybrid Simulation
VIV	Vortex-induced Vibration
rRMSE	Relative Root Mean Square Error
CFD	Computational Fluid Dynamic
FSA	Fourier Series Approach
PID	Proportional–Integral–Derivative
FFT	Fast Fourier Transform

GLOSSARY

\mathbf{M}	Mass matrix of the structure
\mathbf{M}_N	Numerical mass matrix
\mathbf{M}_E	Experimental mass matrix
\mathbf{C}	Damping matrix of the structure
\mathbf{K}	Stiffness matrix of the structure
\mathbf{R}	Restoring force vector matrix
\mathbf{X}	Displacement of the system
$\dot{\mathbf{X}}$	Velocity of the system
\mathbf{l}	Influence matrix
\mathbf{F}_W	Wind-induced force
$\mathbf{u}(t)$	Time-varying wind component
x_i^m	Measured displacement at the i^{th} step
x_i^c	Numerically calculated/target displacement at the i^{th} step
x_i^p	Predicted displacement at the i^{th} step
\bar{x}^c	Average value of numerically calculated displacement
\mathbf{F}_{se}	Self-excited force
\mathbf{F}_{buff}	Buffeting force
\mathbf{F}_{ex}	External force
h	Vertical displacement
α	Torsional displacement

$F_{h_{se}}$	Self-excited lift force
$F_{\alpha_{se}}$	Self-excited moment force
$F_{h_{buff}}$	Buffeting lift force
$F_{\alpha_{buff}}$	Buffeting moment force
$\Phi_{kl}(t)$	Impulse response function by the inverse Fourier transform of the transfer function, and k is the direction of force induced by l direction motion
ϕ_{kl}^I	Imaginary part of transfer function
ϕ_{kl}^R	Real part of transfer function
ρ	Air density
B	Width of the bridge deck
U	Mean wind speed
K	reduced frequency $[\frac{\omega B}{U}]$
H_i^*	Flutter derivatives for lift force
A_i^*	Flutter derivatives for moment
$\tilde{\Phi}_{kl}$	Modified transfer function
K_{max}	Maximum reduced frequency
a_{kl}^i, b_{kl}^i	Coefficients for approximation in the FSA
χ_{kl}^*	Aerodynamic admittance function of k component force induced by the l component of the wind velocity fluctuation

C_D^0	Static coefficient of the drag force when the attack angle is zero
C'_L, C'_M	First derivative of the lift and moment static coefficients at the zero degree
$S_{F_{hbuff}}$	Power spectral densities of lift forces induced by wind
$S_{F_{\alpha buff}}$	Power spectral densities of moment induced by wind
S_w	Power spectral density of the vertical component of the wind fluctuation
\hat{f}_w	$= f \cdot L_w / U,$
σ_w	Standard deviation of the vertical wind component
I_u	Turbulence intensity for wind-flow direction
I_w	Turbulence intensity for vertical direction
L_u	Turbulence length scale for wind-flow direction
L_w	Turbulence length scale for vertical direction
Δt	Time step for numerical analysis
R	Distance between the linear actuators
R_{load}	Distance between the load cell
F_{load}	Maximum load applied to load cell
\mathbf{F}_{Int}	Inertial force caused by experimental mass
\mathbf{F}_M	Measured force by load cell
t_d	Time delay
$G_d(z)$	Discrete transfer function

$X_d^m(z)$	Discrete z -transforms of x_{i+1}^m
$X_c^m(z)$	Discrete z -transforms of x_{i+1}^c
$X_p^m(z)$	Discrete z -transforms of x_{i+1}^p
α_{es}	Estimated actuator delay
$\Delta\alpha$	Adaptive parameter for phase error
k_{est}	Initial estimate of the proportional gain for the motor response
Δk	Adaptive parameter for the amplitude error
$X_p^m(z)$	Discrete z -transforms of x_{i+1}^p
k_p, k_p^k	Proportional adaptive gains of the adaptive control law
k_i, k_i^k	Integrative adaptive gains of the adaptive control law
TI	Tracking indicator
AI	Amplitude indicator
m	Mass
I	Mass moment of the inertia
f	Natural frequency
ξ	Damping ratio
\mathbf{M}_R	Mass ratio
ξ_h^*, ξ_α^*	Realized damping ratio
f_h^*, f_a^*	Realized vibration frequency
f_R	The ratio of the target natural frequency in 2DOF set-up

CHAPTER 1

INTRODUCTION

1.1 Key Issues in a Current Wind Tunnel Test

For a long-span cable-supported bridge, the aerodynamic properties of the bridge deck are the main parameters affecting the vibration and stability of a bridge by wind loads. Therefore, it is required to consider the wind effect when constructing a long-span cable-supported bridge. To assess the stability of a bridge by wind, in general, analytic and experimental approaches are applied. For typical analytic approaches, Computational Fluid Dynamic (CFD) analysis and buffeting ones in time-domain/frequency-domain are adopted. For experimental approaches, 2D and full-scale bridge section model tests using wind tunnels are assessed.

Numerical evaluations on the effects of wind loads through a CFD analysis (Huang et al., 2009; Larsen & Walther, 1998; Sarwar et al., 2008; Zhu et al., 2007) are feasible. Larsen and Walther (1998) reported the applicability of the 2D discrete vortex method to predict the flutter characteristics of some general configuration and then extended it to some practical bridge cross section applications. However, this study overestimated the flutter critical velocity. To overcome this limitation, Huang et al. (2009) estimated flutter deriva-

tives using the improved models including accessory structures such as guard-rails and inspecting vehicle rails which are not considered in the traditional CFD analyses. However, the results from Huang's model did not completely match the experimental values. For these reasons, the traditional and the modified CFD analyses still have remaining disadvantage to obtain reliable results and reduce the extensive computational time. Due to this limitation, this still makes the wind tunnel tests necessary.

Other numerical approaches are applied to overcome the issues from the CFD approaches. The quasi-steady aerodynamic theory (Bisplinghoff & Ashley, 2013; X. Z. Chen & Kareem, 2002; Davenport, 1962; Dowell et al., 1989; Strømmen, 2010) assumes that the aerodynamic forces acting on the structure are calculated from the instantaneous velocity and the load coefficients. To express the instantaneous velocity mathematically, the fluctuating part of the wind is linearized, with a certain assumption of the local displacements. Based on the quasi-steady theory, the aerodynamic forces are represented as assume of the self-excited and buffeting force components.

The self-excited forces are created by the interaction between the motions of fluid and a structure. They are influenced primarily by the mean speed of the incoming wind. The self-excited force theory over the thin airfoil was developed by Theodorsen and Mutchler (1935). Theodorsen and Mutchler (1935) provided an analytical method for the self-excited loads, including a lift force and a pitching moment, on an idealized thin plate under sinusoidal heaving or pitching vibration in steady incompressible flow.

The following studies were performed to apply this approach mathematically over the bridge deck section, a type of a bluff body (Falco et al., 1992; Jensen, 1997; RH Scanlan, 1971). Among these approaches, the flutter equation driven by Robert H Scanlan and Tomo (1971) is widely accepted in the modeling analyses. Robert H Scanlan and Tomo (1971) proposed the definition of the self-excited forces on a bridge deck with flutter derivatives for modeling of unsteady aerodynamic forces. Currently, it is quite general to perform the use the aeroelastic analysis over the long-span bridges with the definitions by Robert H Scanlan and Tomo (1971) and identification of the flutter derivatives from the wind tunnel tests.

The fundamental difficulty in aeroelastic analysis arises from the frequency dependence of self-excited forces. Although they are defined in the time domain, the self-excited forces are based on transfer functions between deck motions. And the self-excited forces are set in the frequency domain. Therefore, an aeroelastic analysis in the frequency domain (Agar, 1989; Jain et al., 1996; Katsuchi et al., 1999; R. Scanlan, 1978a, 1978b; R. H. Scanlan, 1993; R. H. Scanlan & Jones, 1990) is more widely accepted than those in the time domain (Borri & Hoffer, 2000; Bucher & Lin, 1988; X. H. Chen et al., 2000; Costa & Borri, 2006; Ding & Lee, 2000; Kim et al., 2004; Lin & Yang, 1983).

Recently, to include frequency dependent characteristics in time domain, the various approaches using the convolution integrals are proposed. Among them, the rational function approximation (Borri & Hoffer, 2000; Bucher & Lin, 1988; X. H. Chen et al., 2000; Costa & Borri, 2006; Ding & Lee, 2000;

Thang et al., 2008) are generally applied. Also, to satisfy the causality conditions, the penalty function approach (Jung et al., 2011) or the Fourier series approach (Park et al., 2013) is applied.

To identify the flutter derivatives, proper series of the corresponding experiments are required. In general, the free vibration tests or the forced vibration tests are recommended for this mission. In a free vibration test (BogunovićJakobsen & Hjorth-Hansen, 1995; Brownjohn & Jakobsen, 2001; Chowdhury & Sarkar, 2003; Sarkar et al., 1994; R. Scanlan, 1978a), the bridge section model is installed with a spring-supported system in the wind tunnel. The initial displacement is set for free vibration. The flutter derivatives are calculated by the change of the frequency and the damping ratios of the system according to the reduced velocity.

On the other hand, in the forced vibration tests (Cao & Sarkar, 2012; Z. Q. Chen et al., 2005; G. Diana et al., 2004; G. Diana et al., 2010; Giorgio Diana et al., 2014; Falco et al., 1992; Han et al., 2014; Q. C. Li, 1995; Matsumoto, 1996; Matsumoto et al., 1993; Neuhaus et al., 2009; Sarkar et al., 2009), the section model is excited by a sinusoidal motion by motor. The flutter derivatives are extracted from the relation between the force induced by the vertical or torsional harmonic oscillations of the section model and the corresponding displacement.

Both of the free and forced vibration tests have certain advantages and disadvantages. The free vibration tests are easy to perform. In addition, it is able

to simulate the interaction between the bridge deck and the wind. But its vibration is not for the steady state. In fact, the vibration signals are easily decayed out. Secondly, the forced vibration approaches are good to identify the flutter derivatives for the targeting reduced velocity. But its equipment is heavy to handle and costly. In addition, the forced model is not able to include the interaction between the wind and the section model.

There are other issues in the assumptions to define flutter derivatives. Following conditions are basic assumptions for defining flutter derivatives;

1. The self-excited forces are expressed as linear combinations of bridge section motions.
2. Flutter derivatives are functions of the reduced wind speed. It is independent of the vibration amplitude and the frequency.
3. Flutter derivatives are not related to vibration modes.

The detailed study shows that the above assumptions are not always correct. For example, flutter derivatives are strongly affected by torsional amplitudes (Noda et al., 2003; Sarkar et al., 2009). This effect is caused by the movement of the reattaching point in the separation flow. These derivatives also depend on the mean angle of attack (G. Diana et al., 2004; Mannini & Bartoli, 2008). The experimental results by Matsumoto et al. (1993) confirm that the values of the flutter derivatives change with the forced vibration mode.

The bridge sections where hybrid flutter phenomena occur are strongly influenced by the vibrational mode. G. Diana et al. (2010) measure the non-linear components from the wind induced force and express these components

by the instantaneous attack angle between a deck and the wind direction. To overcome the limitation of the current experiment system, Siedziako et al. (2017) develop the new forced vibration system which controls the bridge section model with the random displacement signal. But this system fails to take into account of vibrations due to the natural frequency of the system. In addition, it has a limitation to consider the interaction between the wind and the section model.

Wind tunnel tests are widely applied not only to identify the flutter derivatives but also to evaluate the stability of the bridge section model up to the limit wind velocity using a spring-supported system. In a spring-supported test as shown in Figure 1, the wind-induced vibration of the section model is the major engineering issue. To assess the wind-induced vibration, several parameters, such as stiffness, mass and damping, are to be scaled to match the Cauchy number. The calibration of these dynamic properties, however, requires significant time and effort especially when the experiments are repeatedly with various alternative design shapes and dynamic properties. For a case of damping, as illustrated in Figure 2, due to the installation of an oil damper, there is a non-linear trend so that it is hard to install the equipment precisely. In addition, a spring-supported test has a certain limitation to measure the wind-induced force in real time in a vibration test.

Therefore, a new approach is needed to simulate the aerodynamic properties of the bridge deck through a wind tunnel. Without the complicated assumptions on the wind-induced force, target dynamic properties are precisely

set along with the proper consideration of the interaction. This is the main academic motivation for developing the new approach throughout the study in this dissertation.

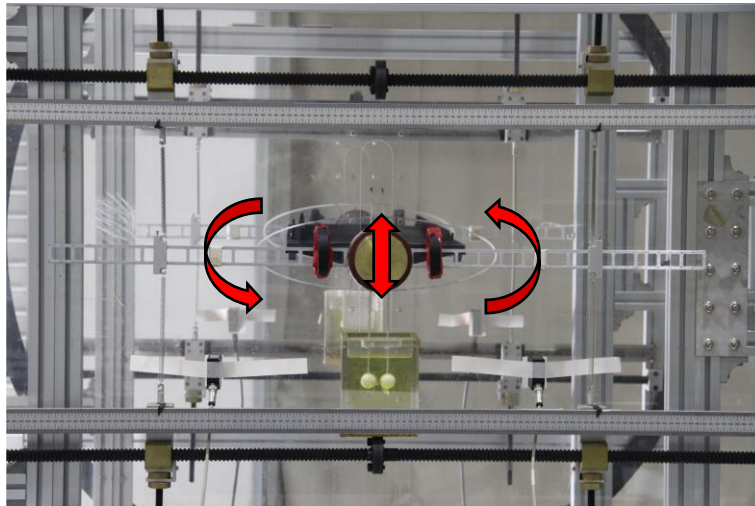


Figure 1. A Spring Support System

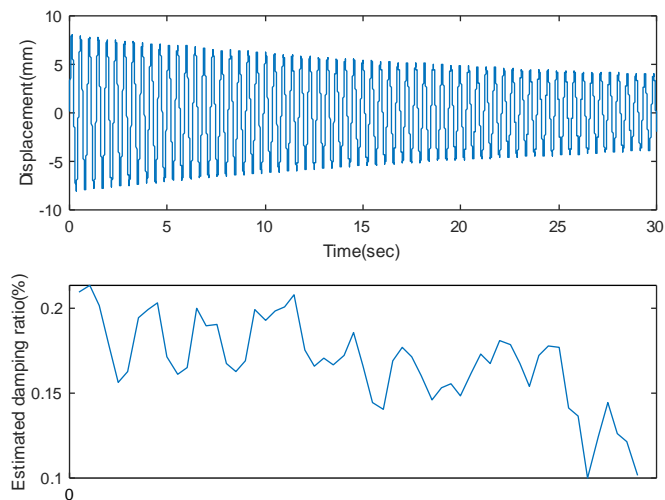


Figure 2. Changes in Damping Ratio by Vibration Magnitudes in a Section Model Tests

1.2 Motivation of the New Approach: Application of a Hybrid Simulation Method in Other Studies

Hybrid simulation methods widely applied in the earthquake engineering is used to solve the problems in the conventional wind tunnel tests. The hybrid simulation method has been actively developed in the field of the earthquake engineering since 1969 (Hirata et al., 2003). In the earthquake applications, the main challenge is to predict the non-linear hysteretic behaviors of reinforcement bars, cracking, crushing or sliding of concrete, buckling of steel, etc. The governing equation for the seismic analysis is written as Eq. (1)

$$\mathbf{M}\ddot{\mathbf{X}} + \mathbf{C}\dot{\mathbf{X}} + \mathbf{R}(\mathbf{X}, \dot{\mathbf{X}}) = -\mathbf{M}\mathbf{I}\ddot{\mathbf{X}}_g \quad (1)$$

where \mathbf{M} and \mathbf{C} represent the mass and the damping matrixes of the structure respectively, $\mathbf{R}(\mathbf{X}, \dot{\mathbf{X}})$ describes a restoring force vector matrix that is a function of the velocity ($\dot{\mathbf{X}}$) and/or the displacement(\mathbf{X}), and \mathbf{I} denotes the influence matrix.

In this equation, the restoring force vector is difficult to be defined through numerical models. To solve this issue, the hybrid simulation methods divide structures into two parts; the numerical model and the experimental specimen. Then, the Eq. (1) can be rearranged as

$$\mathbf{M}\ddot{\mathbf{X}} + \mathbf{C}\dot{\mathbf{X}} + \mathbf{R}_E(\mathbf{X}, \dot{\mathbf{X}}) + \mathbf{R}_N(\mathbf{X}, \dot{\mathbf{X}}) = -\mathbf{M}\mathbf{I}\ddot{\mathbf{X}}_g \quad (2)$$

where the subscripts E and N denote the restoring forces obtained from an experimental specimen and a numerical model, respectively.

An explicit integration scheme is normally used to solve the Eq. (2). In real-time tests where the velocity needs to be imposed accurately for rate-dependent elements, the delay in the actuator's response may create a stability issue. To solve this time-delay problem, various actuator delay compensation methods have been proposed (e.g. Chae et al. (2013); C. Chen and Ricles (2009, 2010); C. Chen et al. (2012); Mercan and Ricles (2007); Mosqueda et al. (2007); Ogawa et al. (2002)).

The similar concept has been adopted for simulations in other wind engineering fields. For example, Hirata et al. (2003); Kanda et al. (2006); Kato and Kanda (2014); Wu and Song (2019) attempted to simulate building vibration with hybrid simulations. Kato and Kanda (2014) performed the vibration experiments to understand the single-degree-of-freedom in three-dimensional flows and the multi-degree-of-freedom under the base isolation. Based on the experimental analysis, the impact of a mass-damping parameter on the vibration has been assessed. To understand the effect of the damping system, Wu and Song (2019) develop the hybrid system prescribing the motion of dampers through an actuator.

1.3 Application of the RTHS System to Wind Tunnel Tests

In the same manner, the hybrid simulation is applied to simulate wind tunnel tests. In the earthquake simulation works, the non-linearity of the material is the big issue for the numerical simulations. But in the wind engineering,

the wind-induced force is the real issue for the actual numerical simulations. Therefore, the RTHS system approach is developed in this dissertation. Firstly, the direct experimental measurements are developed for this wind-induced force. And all remaining parts are performed by the numerical studies using the governing equation prescribed as the Eq. (3).

$$\mathbf{M}\ddot{\mathbf{X}} + \mathbf{C}\dot{\mathbf{X}} + \mathbf{K}\mathbf{X} = \mathbf{F}_W(\mathbf{X}, \dot{\mathbf{X}}, \mathbf{u}(t)) \quad (3)$$

where, \mathbf{K} represents a stiffness matrix of the system, \mathbf{F}_W is the wind-induced force, and $\mathbf{u}(t)$ is a time-varying wind component. The concept of the new hybrid simulation system is depicted in Figure 3.

The wind-induced force, which is determined by the deck shape and the motion of the deck, is directly measured through a set of load cells attached to both ends of the deck section model. The position of the deck section model is determined by a basic dynamic equation in the control program. The application of the hybrid simulation does not create any critical error caused by assumptions because the proposed approach solves basic dynamic equations precisely without any assumption. In the control program, \mathbf{M} , \mathbf{C} , and \mathbf{K} are constant values. Traditionally, the calibration of these parameters requires a trial-error approach. However, unlike the conventional wind tunnel test, these values do not require any calibration. The advantage of the proposed approach is to exactly describe the wind-induced force without trial-errors.

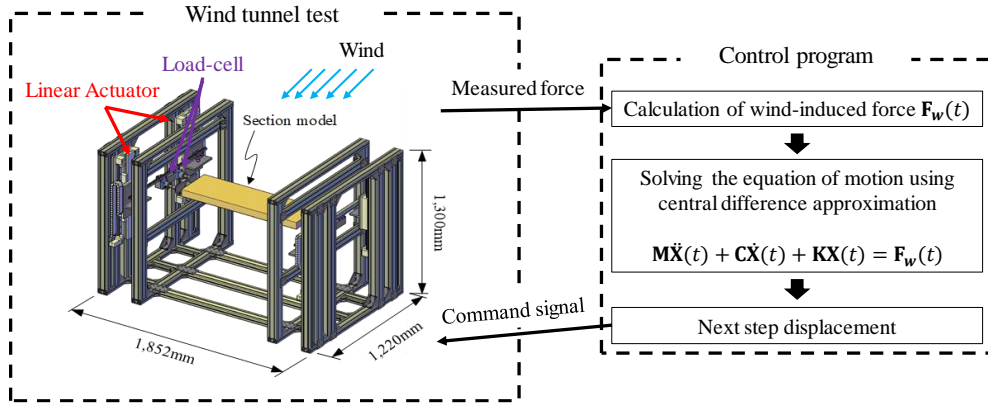


Figure 3. The Concept of the Application of the RTHS System in the Wind Tunnel Tests

CHAPTER 2

FEASIBILITY STUDIES FOR THE PROPOSED RTHS SYSTEM

2.1 Numerical Simulation Methods for a Feasibility Study of the RTHS System

Before conducting the RTHS system development in lab scales, it is essential to check the feasibility of the system first. If this system satisfies the following three conditions, it confirms that the feasibility of the proposed RTHS system. Firstly, at given sampling rate, the RTHS system sufficiently simulates real-world behavior when it solves the equation of motion. Secondly, the one step delay caused by limitation of the transmission system doesn't pollute the accuracy or tendency of the results. Thirdly, the noise in the measured force doesn't affect the displacement results significantly.

To assure the feasibility of the proposed RTHS system, the numerical simulation for the entire RTHS system is performed ahead of the real experiments are performed. In numerical simulations, instead of measuring the wind force through the wind tunnel test as depicted in Figure 3, the wind-induced force is numerically calculated separately with two forces, the buffeting force and the self-excited force, as shown in Figure 4.

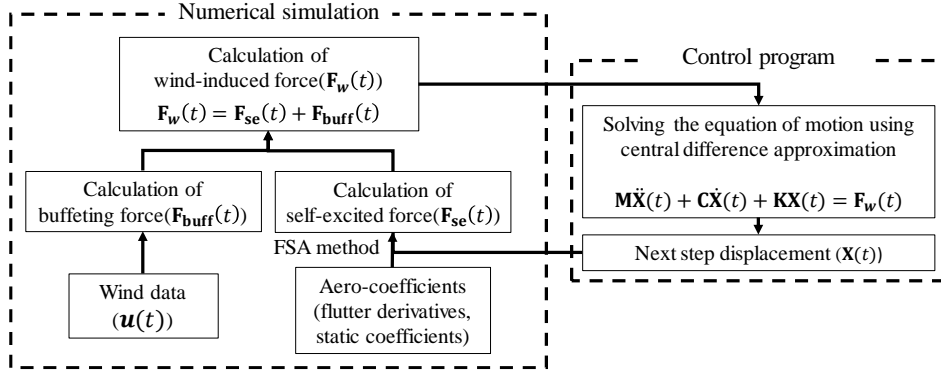


Figure 4. Concept of the Numerical Hybrid Simulation Method

The convolution integral and the Fourier series approaches (FSA, Park et al. (2013)) are used to estimate the self-excited force in the wind-induced force. The buffeting force is calculated using the turbulent wind data following the Von Karman spectrum. The central difference approximation method is conducted to solve the dynamic equation.

The results from an aeroelastic analysis are used as reference values to determine the accuracy of the actual RTHS system process using numerical simulation results. The applied aeroelastic analysis is more accurate even though it uses the same theoretical equations to simulate the wind-induced forces; (1) there is no time-delay and a noise in the wind-induced forces and (2) the sampling rate is arbitrary set to enhance the accuracy of the analysis. In this sense, the results from the aeroelastic analyses are chosen as reference values to check the accuracy of the numerical simulations. The accuracy of the result is checked by the relative root mean square error (rRMSE, %) defined in Eq. (4).

$$\text{rRMSE} = \sqrt{\frac{\sum_{i=1}^N (x_i^m - x_i^c)^2}{\sum_{i=1}^N (x_i^c - \bar{x}^c)^2}} \quad (4)$$

where, x_i^m is a measured displacement at the i^{th} step, x_i^c is a numerically calculated displacement at the i^{th} step and \bar{x}^c means an average value of a numerically calculated displacement

The accuracy by the rRMSE value is categorized as follows (Despotovic et al., 2016; M.-F. Li et al., 2013).

- (1) Excellent: When the value of rRMSE is less than 10%, the results are categorized as excellent ones,
- (2) Good: When the value of rRMSE lies between 10 and 20% the results are categorized as good ones,
- (3) Fair: When the value of rRMSE lies between 20 and 30% the results are categorized as fair ones, and
- (4) Poor: When the value of rRMSE is greater than 30% the results are categorized as poor ones, disqualified to simulate the actual wind tunnel experiments.

The target bridge for the feasibility study is selected for the 2nd Jindo Bridge. The sampling frequency in numerical simulations is set to be 200 Hz. The target wind speed is set to be 5 and 15m/s in the wind tunnel scale to simulate the actual field wind speeds of 36 and 108 m/s. To see the effect of the noise in the measured force, 1,2,5 and 10 % of random noises to the wind-induced force term are added.

When the results from this numerical simulation match the ones from the aeroelastic analysis within a preset range ($rRMSE < 30\%$), it verifies that the proposed RTHS system is qualified as a practical new approach to simulate the vibration in wind tunnel tests.

2.2 Time Domain Analysis Method to Estimate Wind-induced Forces in a Numerical Simulation Method and an Aeroelastic Analysis

The response of a bridge section model by wind can be expressed by the Eq. (5).

$$\mathbf{M}\ddot{\mathbf{X}} + \mathbf{C}\dot{\mathbf{X}} + \mathbf{K}\mathbf{X} = \mathbf{F}_{se}(\mathbf{X}, \dot{\mathbf{X}}) + \mathbf{F}_{buff}(\mathbf{u}) \quad (5)$$

where \mathbf{F}_{se} and \mathbf{F}_{buff} are the self-excited force and the buffeting force respectively. To develop the RTHS system in this dissertation, only two degrees of freedom are considered; the vertical and torsional motions. Therefore, Eq. (5) is rewritten in the 2×2 matrix form as summarized in Eq. (6). Hereafter, all proposed mathematical equations are expressed with the vertical and torsional motions only.

$$\begin{bmatrix} M_h & 0 \\ 0 & M_\alpha \end{bmatrix} \begin{bmatrix} \ddot{h} \\ \ddot{\alpha} \end{bmatrix} + \begin{bmatrix} C_h & 0 \\ 0 & C_\alpha \end{bmatrix} \begin{bmatrix} \dot{h} \\ \dot{\alpha} \end{bmatrix} + \begin{bmatrix} K_h & 0 \\ 0 & K_\alpha \end{bmatrix} \begin{bmatrix} h \\ \alpha \end{bmatrix} = \begin{bmatrix} F_{h_{se}} \\ F_{\alpha_{se}} \end{bmatrix} + \begin{bmatrix} F_{h_{buff}} \\ F_{\alpha_{buff}} \end{bmatrix} \quad (6)$$

where h and α are vertical and torsional degrees of freedom respectively, $F_{h_{se}}$ and $F_{\alpha_{se}}$ are the self-excited lift force and the moment induced by the

motion, respectively, and $F_{h_{buff}}$ and $F_{\alpha_{buff}}$ are the buffeting lift force and the moment induced by incoming turbulence, respectively.

The self-excited force in a stationary wind flow is expressed as follows in Eq. (7), using the impulse response function.

$$\begin{aligned} F_{h_{se}} &= \frac{1}{2} \rho U^2 B \left[\int_0^t \Phi_{hh}(t - \tau) \frac{h(\tau)}{B} d\tau + \int_0^t \Phi_{h\alpha}(t - \tau) \alpha(\tau) d\tau \right] \\ F_{\alpha_{se}} &= \frac{1}{2} \rho U^2 B^2 \left[\int_0^t \Phi_{\alpha h}(t - \tau) \frac{h(\tau)}{B} d\tau + \int_0^t \Phi_{\alpha\alpha}(t - \tau) \alpha(\tau) d\tau \right] \end{aligned} \quad (7)$$

where $\Phi_{kl}(t)$ is the impulse response function by the inverse Fourier transform of the transfer function and k is the direction of the force induced by the I direction motion. Each component of the impulse response function is defined as the inverse Fourier transform of the corresponding component of the self-excited force in the frequency domain as depicted in Eq. (8).

$$\Phi_{kl}(t) = \frac{1}{2\pi} \int_{-\infty}^{\infty} (i\phi_{kl}^I + \phi_{kl}^R) d\omega \quad (8)$$

where ϕ_{kl}^I, ϕ_{kl}^R are the imaginary and the real parts of the transfer function, respectively and the k is the direction force induced by the I direction motion.

Robert H Scanlan and Tomo (1971) proposed the flutter derivatives which are a function of the frequency, to define the self-excited force as shown in Eq.(9).

$$F_{h_{se}} = \frac{1}{2} \rho U^2 B \left[KH_1^* \frac{\dot{h}}{U} + KH_2^* \frac{\dot{\alpha}}{U} + K^2 H_3^* \alpha + K^2 H_4^* \frac{h}{B} \right] \quad (9-1)$$

$$F_{\alpha_{se}} = \frac{1}{2} \rho U^2 B^2 \left[K A_1^* \frac{\dot{h}}{U} + K A_2^* \frac{B \dot{\alpha}}{U} + K^2 A_3^* \alpha + K^2 A_4^* \frac{h}{B} \right] \quad (9-2)$$

where ρ is the air density, B is the width of the bridge deck, U is the mean wind speed, K is the reduced frequency $[\frac{\omega B}{U}]$, and H_i^*, A_i^* are the flutter derivatives for the lift force and the moment, respectively.

By using the Eq. (9-2), the aerodynamic transfer function is expressed in terms of the flutter derivatives identified through the wind tunnel tests.

$$\begin{aligned} i\phi_{hh}^I + \phi_{hh}^R &= iK^2 H_1^* + K^2 H_4^* & i\phi_{h\alpha}^I + \phi_{h\alpha}^R &= iK^2 H_2^* + K^2 H_3^* \\ i\phi_{\alpha h}^I + \phi_{\alpha h}^R &= iK^2 A_1^* + K^2 A_4^* & i\phi_{\alpha\alpha}^I + \phi_{\alpha\alpha}^R &= iK^2 A_2^* + K^2 A_3^* \end{aligned} \quad (9)$$

Here, the FSA is used to approximate an aerodynamic transfer function in a frequency domain with a trigonometric function as illustrated in Eq. (10)

$$\begin{aligned} \phi_{kl}^R &\approx \tilde{\phi}_{kl}^R = a_{kl}^0 + \sum_{n=1}^N a_{kl}^n \cos \frac{n\pi}{K_{max}} K \\ \phi_{kl}^I &\approx \tilde{\phi}_{kl}^I = b_{kl}^0 + \sum_{n=1}^N b_{kl}^n \sin \frac{n\pi}{K_{max}} K \end{aligned} \quad (10)$$

where, $\tilde{\phi}_{kl}$ is the kl component of the modified transfer function, K_{max} is the maximum reduced frequency, and a_{kl}^0 , b_{kl}^0 , a_{kl}^n are the coefficients for the approximation in the FSA. These modified transfer functions are restricted to maintain the causality condition. The causality condition, which states that the impulse response functions vanish for the negative time domain, is required to satisfy the Eq. (11).

$$\Phi_{kl} = \frac{1}{\pi} \int_0^{\infty} [\phi_{kl}^R(\omega) \cos \omega t - \phi_{kl}^I(\omega) \sin \omega t] d\omega \quad \text{for } t \geq 0 \quad (11)$$

$$\Phi_{kl} = \frac{1}{\pi} \int_0^{\infty} [\phi_{kl}^R(\omega) \cos \omega t - \phi_{kl}^I(\omega) \sin \omega t] d\omega \equiv 0 \quad \text{for } t < 0$$

Substituting the causality condition (Eq. (11)) into Eq. (10) yields Eq.(12).

Finally, the self-excited force is expressed as Eq.(13).

$$\bar{\Phi}_{kl}(t) = a_{kl}^0 \delta(t) + \frac{B}{U} b_{kl}^0 \dot{\delta}(t) + \sum_{n=1}^N a_{kl}^n \delta\left(t - \frac{B}{U} \frac{n\pi}{K_{max}}\right) \quad (12)$$

$$\begin{aligned} F_{h_{se}}(t) = & \frac{1}{2} \rho U^2 B [a_{hh}^0 \frac{h(t)}{B} + b_{hh}^0 \frac{\dot{h}(t)}{U} + \frac{1}{B} \sum_{n=1}^N a_{hh}^n h\left(t - \frac{B}{U} \frac{n\pi}{K_{max}}\right) \\ & + a_{h\alpha}^0 \alpha(t) + \frac{U}{B} b_{h\alpha}^0 \dot{\alpha}(t) + \sum_{n=1}^N a_{h\alpha}^n \alpha\left(t - \frac{B}{U} \frac{n\pi}{K_{max}}\right)] \end{aligned} \quad (13)$$

$$\begin{aligned} F_{\alpha_{se}}(t) = & \frac{1}{2} \rho U^2 B^2 [a_{\alpha h}^0 \frac{h(t)}{B} + b_{\alpha h}^0 \frac{\dot{h}(t)}{U} + \frac{1}{B} \sum_{n=1}^N a_{\alpha h}^n h\left(t - \frac{B}{U} \frac{n\pi}{K_{max}}\right) \\ & + a_{\alpha\alpha}^0 \alpha(t) + \frac{U}{B} b_{\alpha\alpha}^0 \dot{\alpha}(t) + \sum_{n=1}^N a_{\alpha\alpha}^n \alpha\left(t - \frac{B}{U} \frac{n\pi}{K_{max}}\right)] \end{aligned}$$

A frequency dependent characteristic of the buffeting force is considered with the aerodynamic admittance function. It is assumed that there is no phase lag between the buffeting force and the wind velocity fluctuation. This means the imaginary part of the aerodynamic admittance function is equal to zero. The aerodynamic admittance function is then simply multiplied in the frequency-domain. Finally, the buffeting force in the time-domain is easily obtained by the Inverse-Fourier transform of the calculated buffeting force in a frequency-domain.

The power spectral density of the buffeting force in 2DOF is expressed as Eq. (14). In this dissertation, only the vertical component of the wind velocity fluctuation is considered in the buffeting force.

$$\begin{bmatrix} S_{F_{hbuff}} \\ S_{F_{\alpha buff}} \end{bmatrix} = \left(\frac{1}{2} \rho U B \right)^2 \begin{bmatrix} \left(\chi_{F_{hw}}^* \right)^2 (C_L' + C_D^0)^2 \\ \left(\chi_{F_{\alpha w}}^* \right)^2 (C_M')^2 \end{bmatrix} S_w \quad (14)$$

where χ_{kl}^* is the aerodynamic admittance function of the k component force induced by the l component of the wind velocity fluctuation, C_D^0 is the static coefficient of the drag force when the attack angle is zero, C_L' , C_M' are the first derivatives of the lift and the moment static coefficients at the zero degree, $S_{F_{hbuff}}$, $S_{F_{\alpha buff}}$ are the power spectral densities of lift forces and the moment induced by wind respectively, and S_w is the power spectral density of the vertical component of the wind fluctuation.

The Davenport's formula (Davenport, 1962) is used for the aerodynamic admittance function. The buffeting force in a time-domain is simply obtained by the inverse transform of Eq. (14) as shown in Eq. (15).

$$\begin{bmatrix} F_{hbuff} \\ F_{\alpha buff} \end{bmatrix} = \frac{1}{2} \rho U^2 B \begin{bmatrix} \chi_{F_{hw}}^* (C_L' + C_D^0) \\ \chi_{F_{\alpha w}}^* C_M' \end{bmatrix} w \quad (15)$$

2.3 Cases for Feasibility Studies of the RTHS System

2.3.1 Analysis Conditions for the Case Studies

The 2nd Jindo Bridge is used for the feasibility study. The general shape of the deck section is illustrated in Figure 5. The 1/36 length scale model is proposed to simulate the prototype bridge. The dynamic properties for the tests are summarized in Table 1.

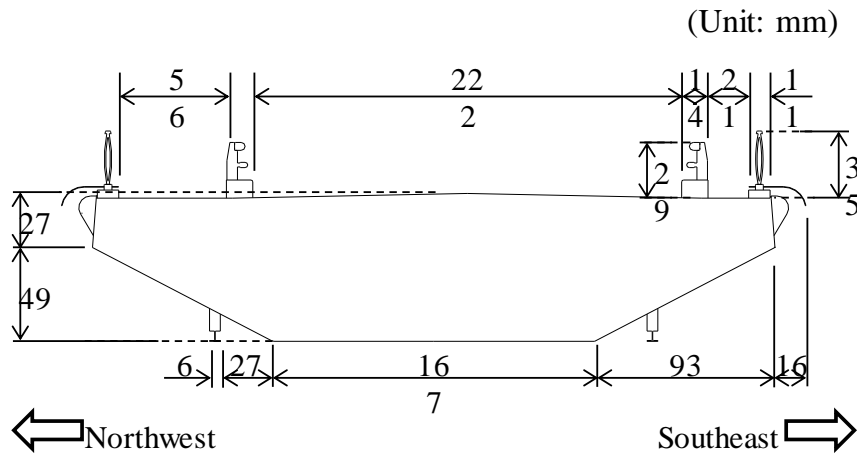


Figure 5. Deck Section Shape of the 2nd Jindo Bridge

Table 1. Dynamic Properties of 2nd Jindo Bridge Section Model

Parameters	Value	Unit
Length of the model	0.90	m
Width of the model	0.35	m
Mass	6.96	kg/m
Mass moment of the inertia	0.09	kg·m ² /m
1st vertical frequency	2.18	Hz
1st torsional frequency	9.17	Hz

The turbulence components are generated based on the Von Karman spectrum (von Karman, 1948). The Von Karman spectrum is mathematically prescribed as Eq. (16).

$$S_w = \frac{\sigma_w^2}{f} \times \frac{4\hat{f}_w(1 + 755.2\hat{f}_w^2)}{(1 + 283.2\hat{f}_w^2)^{11/6}} \quad (16)$$

where $\hat{f}_w = f \cdot L_w/U$, σ_w is the standard deviation of the vertical wind component. In the feasibility tests, the turbulence intensity, I_w and the turbulence length scale, L_w of the vertical wind component are set to be 5 % and 0.2 m, respectively. The wind information is generated by applying a random phase angle to each frequency component of the Von Karman spectrum. The time step in the simulations is 5 ms and the total simulation time is 60 sec. The case studies are done with the mean wind speed of 5 and 15 m/s in the wind tunnel scale. These wind speed values are converted to 36 and 108 m/s in the prototype scale. The static coefficients and flutter derivatives extracted from the experiment in the Seoul National University are used for the analysis as illustrated in Figure 7.

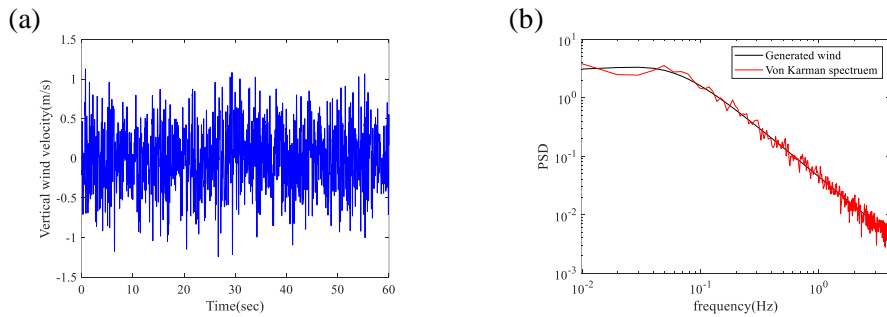


Figure 6. Time Series of the Generated Wind Data (b) Comparison of the Von Karman Spectrum and the Spectrum of the Generated Wind

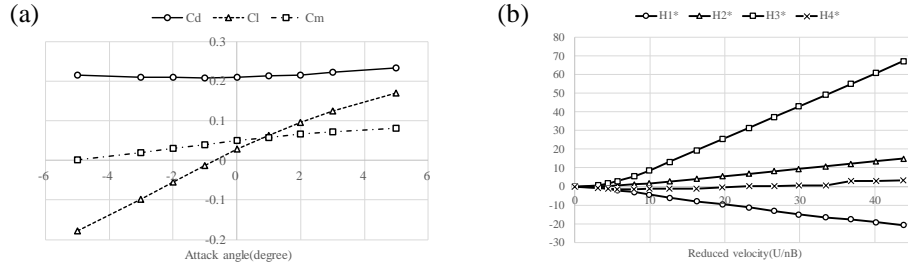


Figure 7. (a) Aerostatic Coefficients and (b) Flutter Derivatives of 2nd Jindo Bridge Obtained by Experiments

To understand the effect of the measured force over the signal to noise level, the additional random noise values of 1, 2, 5, and 10 % of the maximum values of the calculated wind-induced force are applied. Figure 8 shows the calculated wind-induced forces in the numerical simulation for different noise ratios for the 5 m/s case.

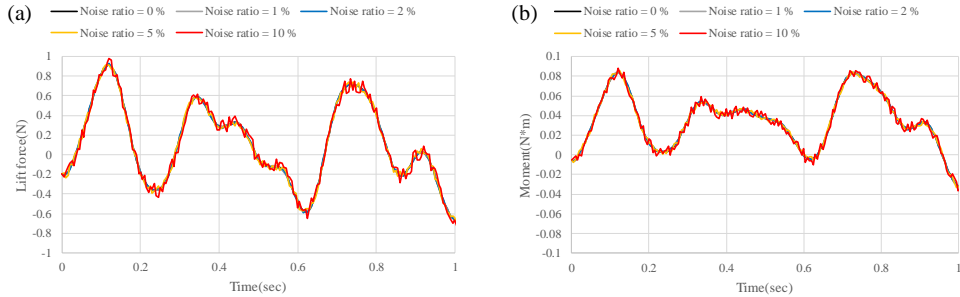


Figure 8. Wind-induced force for Different Noise Ratios at 5 m/s Wind Speed (a) Lift Force and (b) Moment

2.3.2 Analysis Results

Figure 9 and Figure 10 illustrate the results from the numerical simulations and the traditional aeroelastic analysis approaches. The results in Figure 9 are at the wind speed of 5 m/s. And those in Figure 10 are for the case of 15 m/s.

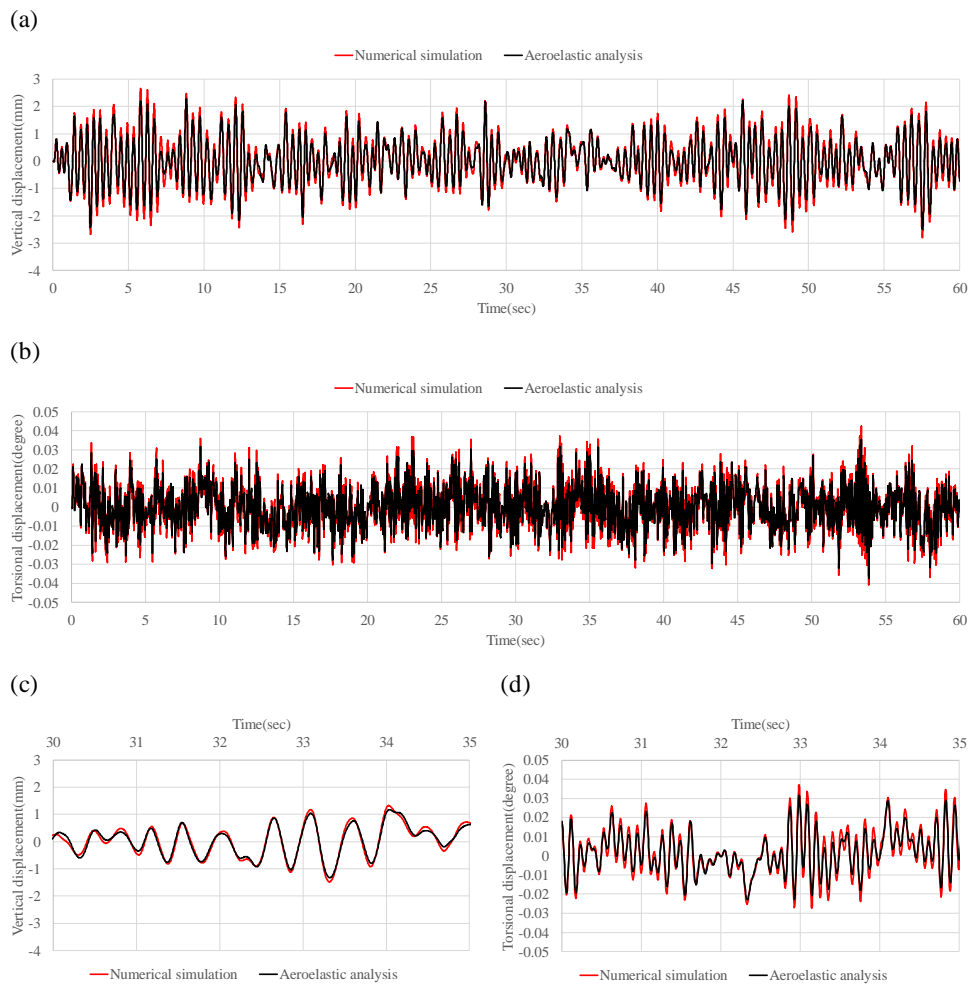


Figure 9. Analysis Results at 5 m/s (Noise Ratio = 10%) (a) Vertical Response at 0 to 60 sec (b) Torsional Response at 0 to 60 sec (c) Vertical Response at 30 to 35 sec (d) Torsional Response at 30 to 35 sec

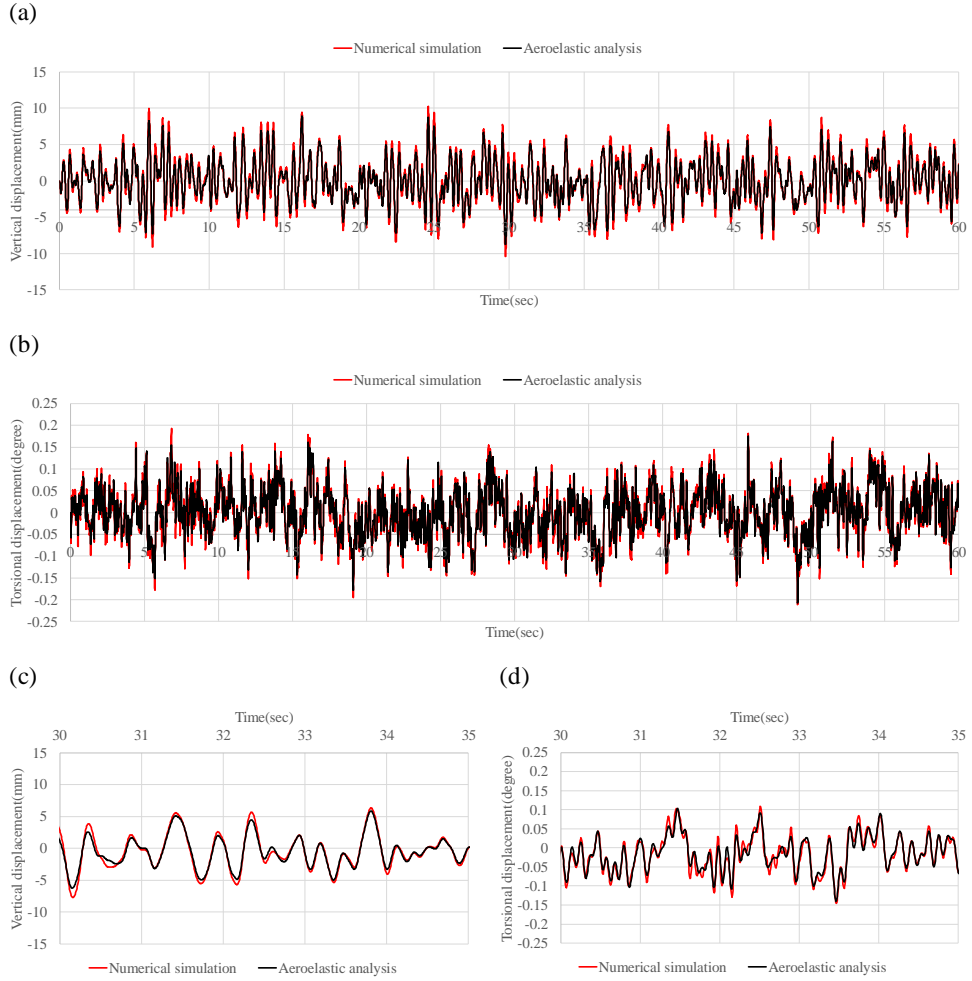


Figure 10. Analysis Results at 15 m/s (Noise Ratio = 10%) (a)Vertical Response at 0 to 60 sec (b)Torsional Response at 0 to 60 sec (c)Vertical Response at 30 to 35 sec (d) Torsional Response at 30 to 35 sec

As shown in Figure 9 and Figure 10, when the noise ratio is 10 %, even though there is a certain difference in absolute values, the tendency of the results is identical. For more accurate analyses, the rRMSE values between the numerical simulations and the corresponding aeroelastic analyses are summarized in Table 2.

Table 2. rRMSE between Results from Aeroelastic Analyses and Numerical Simulations

Noise ratio	Response at 5m/s		Response at 15m/s	
	Vertical	Torsional	Vertical	Torsional
0%	23.5	24.7	20.7	14.8
1%	23.5	24.7	20.7	14.9
2%	23.3	24.7	20.7	15.1
5%	23.4	25.2	20.9	15.8
10%	23.5	26.4	21.3	20.8

As summarized in Table 2, the impact of the noise in the measured force is negligible when the noise level is less than 10 %. Instead of the noise, the effects from the one-step delay and the predefined sampling frequency give more influence. All the values of the rRMSE in Table 2 are less than 30% so that they are in the category of the Fair. This leads to the conclusion that the proposed RTHS system well describes the reference aeroelastic analysis. In summary, the outcomes from the feasibility studies checked by the numerical simulations prove the validity of applying the RTHS system procedure so that the proposed RTHS system is able to be applied to simulate the actual bridge deck wind behaviors.

CHAPTER 3

DESIGN AND CONSTRUCTION OF HARDWARE AND SOFTWARE FOR THE RTHS SYSTEM

3.1 Design of Hardware Components of the RTHS System

3.1.1 Methods for Describing the 2DOF Motion in the RTHS System

Conventional 2D wind tunnel tests generally allow to displace the bridge deck section model in the vertical and the torsional directions as illustrated in Figure 1. To simulate these motions, four linear motors are used in the RTHS system. Each 2 linear actuators are installed in the same section. If these two motors move together, it initiates the vertical motion. If these motors move independently, it enables the system torsional movement of the system as illustrated Figure 11.

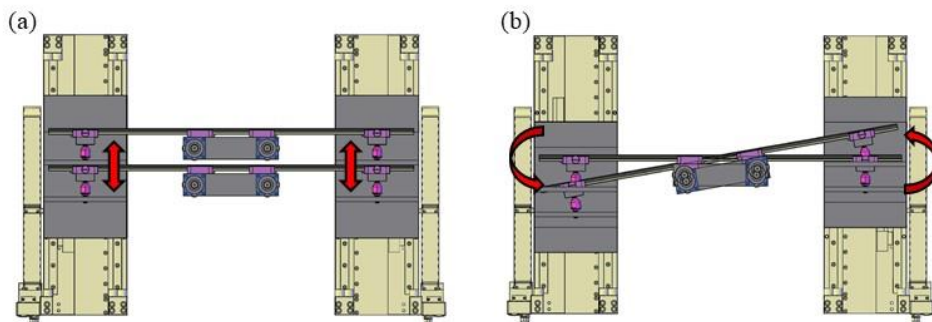


Figure 11. (a) Vertical Direction Movement (b) Torsional Direction Movement in the RTHS System

Between the moving part of the linear motor and the guide rail, a locking sleeve bearing carriage and an inline ball joint linkage are positioned as shown in Figure 12. These components allow the relative rotation between the guide rail and the moving part of the linear motor up to 17.5° . The slight change in the length between two linear motors occurs when the torsional motion is imposed. One of the locking sleeve bearing carriages in each side is always locked. The other locking sleeve bearing carriages are loosened so that the lateral directional displacement and the proper motion are allowed between two motors. Two bi-axial load cells are attached between the guid-rail and the section model mounting plate to measure two components of the forces such as the vertical and torsional forces.

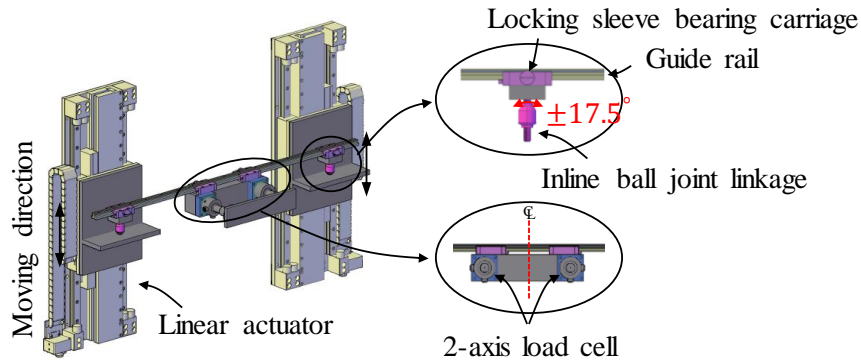


Figure 12. Details about Rotational Joint and Force Measurement Part in the RTHS System

3.1.2 Numerical Analysis Conditions

As summarized in the previous section, to develop the RTHS system, four linear motors and the load cells are required. Before making the final decision on the specific linear motors and load cells, the design values for these parts are to be determined by the numerical aeroelastic analysis. For numerical analysis, the proper bridge sections are to be selected. For this mission, the dynamic property data from the previous actual wind tunnel tests are scrutinized. The data set is summarized in Table 3. The data shows that the range of the mass for the wind tunnel tests is between 4.2 and 11.2 kg/m. It also illustrates the range for the mass moment of the inertia lies between 0.050 and 0.165 kg·m²/m. The traditional value ranges of the natural frequency for the wind tunnel experiments in the vertical direction is between 1.1 and 3.8 Hz. And ones in the torsional direction is between 2.5 and 9.0 Hz.

Table 3. Dynamic Properties of an Actual Bridges Section Model for Wind Tunnel Tests

Bridge Case	Length scale	Mass (kg/m)	Mass moment of inertia (kg·m ² /m)	Vertical frequency (Hz)	Torsional frequency (Hz)	Frequency ratio
Hwayang	1/60	10.0	0.066	2.1	9.0	4.3
Jido-Imja	1/40	11.2	0.148	2.2	4.5	2.0
YiSunsin	1/70	4.5	0.098	1.1	2.5	2.2
Jangbogo	1/45	10.2	0.165	1.9	3.9	2.1
1st Jindo	1/36	5.4	0.050	2.1	6.1	2.9
2nd Jindo	1/36	6.9	0.091	2.1	8.8	4.2
Mankyung	1/100	8.4	0.076	3.8	4.4	1.2
Old Tacoma	1/35	6.8	0.071	2.5	4.6	1.8
Total Range	1/35~1/100	4.2~11.2	0.050~0.165	1.1~3.8	2.5~9.0	1.2~4.3

For the actual design of the RTHS system, the so-called worst case approaches are adopted with the extreme parameter values to assure the safety of the system. The maximum values of the wind-induced force and the response are applied. The Old Tacoma Narrow(TN) Bridge which collapsed due to the occurrence of flutter phenomena with about the speed of 14 m/s and Mankyung(MK) Bridge, where a large buffeting response occurs by a flutter phenomenon with about the speed of 128 m/s are chosen as analysis cases for design parameter setting.

The actual cross section shape for these two study cases are illustrated in Figure 13. When the length scale of MK Bridge is increased from the 1/100 to the 1/70, the corresponding setting mass and the mass moment of the inertia are changed to the values of 17.1 kg and 0.317 kg·m²/m, which are two times higher than the range of commonly used values in Table 3 .

The numerical analysis is implemented for these two cases, (1) modified MK Bridge and (2) TN Bridge. The vertical natural frequency for each analysis case is set to be in the range of 6 and 10 Hz for this worst-case scenario studies.

Turbulence information for the analysis is generated in the same manner as described in Section 2.3.1. The following characteristics values are used for the generating times series of the wind data; $I_u = 12 \%$, $I_w = 6 \%$, $L_u = 140$ m, $L_w = 12$ m and the duration of time = 60 sec. The length of the bridge section model in the numerical analysis is set to be 2 m. The flutter

derivatives which were identified by the series of experiments in Seoul National University are used for the numerical analysis. Five different cases are studied for the numerical analysis. The dynamic parameters for the studies are summarized in Table 4.

The analysis conditions are designed to assure the highest response within the maximum allowable wind tunnel velocity of 18 m/s. The analysis is performed by defining the wind-induced force using the self-excited force and the buffeting force defined in Section 2.2. The Newmark's method with $\beta = \frac{1}{4}$, $\gamma = \frac{1}{2}$ and $\Delta t = 2$ ms is used for the numerical evaluation of the dynamic responses.

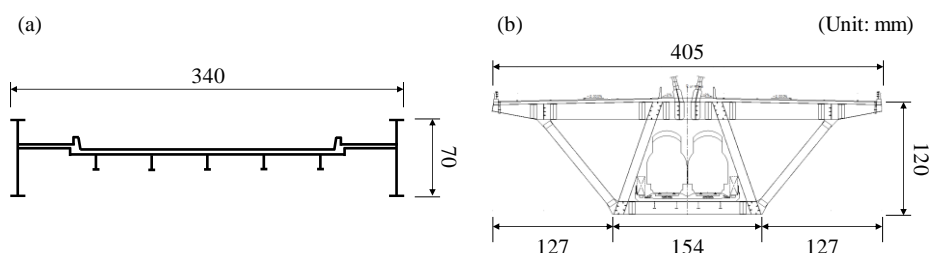


Figure 13. Target Bridge Section (a) TN Bridge (b) MK Bridge Section

Table 4. Dynamic Parameters for Numerical Analysis Case

# of case	Bridge name	Mass (kg/m)	Mass moment of inertia (kg·m ² /m)	Vertical Frequency (Hz)	Torsional Frequency (Hz)	Time scale	Wind speed in the wind tunnel(m/s)	Wind speed in the prototype bridge(m/s)
1	Old Tacoma	6.79	0.071	6.0	11.1	46.2	18.0	12.1
2		6.79	0.071	8.0	14.8	61.5		10.2
3	Modified Mankyung	17.08	0.317	6.0	6.9	10.1		124.5
4		17.08	0.317	8.0	9.3	13.5		93.4
5		17.08	0.317	10.0	11.6	16.9		74.7

3.1.3 Analysis Results

The displacement, the velocity, and the acceleration results are obtained as shown in Figure 14.

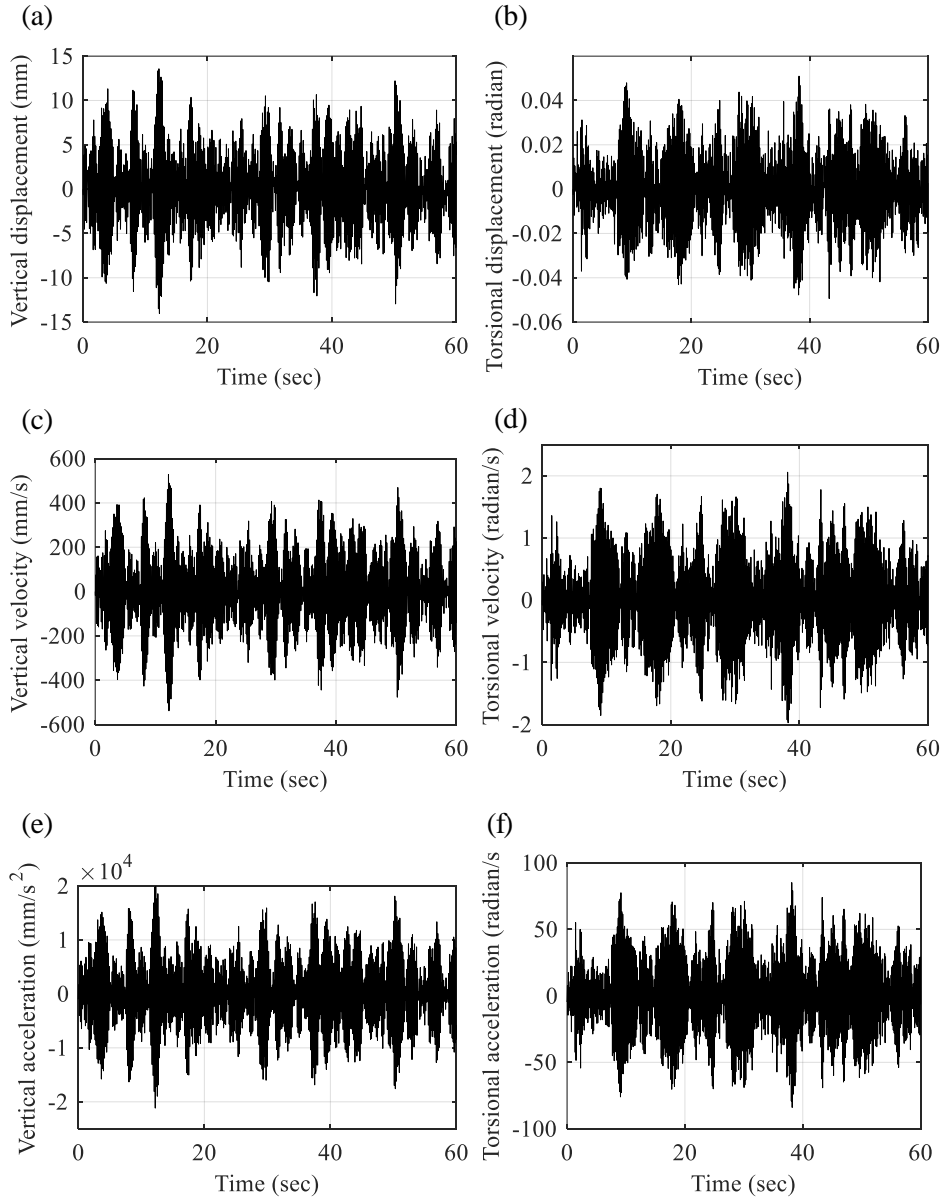


Figure 14. Analysis Results for Case 3: (a) Vertical Displacement (b) Torsional Displacement (c) Vertical Velocity (d) Torsional Velocity (e) Vertical Acceleration (f) Torsional Acceleration

Table 5 shows the comparison of the maximum values extracted from the analysis. The maximum values for each direction are marked in bold. The maximum values for the vertical direction are derived from the TN Bridge cases. And the maximum values for the torsional direction are derived from the MK Bridge cases. In the case for the torsional direction, the maximum values of the displacement and the acceleration are generated from the different test cases. This is due to the fact that the acceleration increases in proportion to the square of the frequency. As the time scale increases, the natural frequency also increases proportionally. Therefore, the case with the highest displacement and the acceleration is different.

To calculate the total maximum force, cases 1, 3, and 4 providing the maximum values in terms of the movements are analyzed. The total force is expressed as the sum of the four force components; (1) the static force, (2) the buffeting force, (3) the self-excited force, and (4) the inertia force. Figure 15 shows the force results in Case 4 as an example. As shown in Figure 15, the inertia force occupies the largest portion in the total force. This inertia force is

Table 5. Maximum Values in the Numerical Analysis Results

# of test case	Vertical direction			Torsional direction		
	Displacement (mm)	Velocity (m/s)	Acceleration (m/s ²)	Displacement (radian)	Velocity (radian/s)	Acceleration (radian/s ²)
1	14.66	555.4	21130	0.01	0.46	25.0
2	8.51	381.9	18684	0.01	0.17	10.3
3	14.06	538.8	21190	0.05	2.06	85.2
4	8.03	412.3	21020	0.03	1.67	90.9
5	3.31	187.8	10901	0.01	0.23	13.0

the case when the target mass is assumed to be in motion. In real RTHS systems, the value of the target mass is numerically given so that there is no need to actually realize the target mass with the additional weight. Therefore, the actual inertia force is less than the numerical analysis value in the RTHS experiments. But the maximum inertia force is supposed to be in the design process for the conservative approach.

Table 6 shows the minimum and the maximum values of the lift force and the moment for each case. As a result, the maximum range of the lift and the moment are set to be at 900 N and 140N·m, respectively.

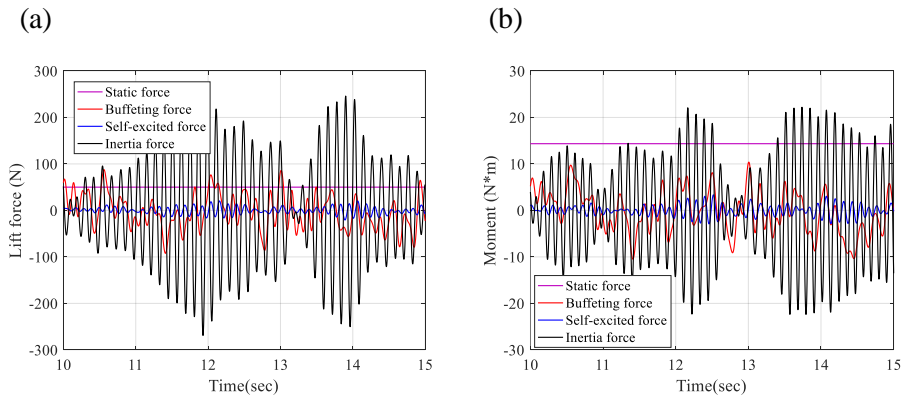


Figure 15. Force Results in Case 4: (a) Lift force (b) Moment

Table 6. Maximum and Minimum Forces at Each Analysis Case

# of experiment case	Lift force(N)		Moment(N·m)	
	Maximum value	Minimum value	Maximum value	Minimum value
1	473.5	-383.9	80.9	-50.5
3	471.7	-365.7	77.4	-59.4
4	441.7	-446.9	6.5	-6.9

3.1.4 Selection of the Experimental Apparatus

The elements of the RTHS system are determined by the analysis results in the previous section. The basic components of the RTHS system are the linear motor, the load cell, and the frame elements.

The results from the displacement analysis in the previous section are based on the center point of both ends. Therefore, to excite the motion with four linear actuators, it is necessary to convert the motion at each linear actuator position. The converted value depends on the distance, R , between the linear actuators because of the torsional motion. Figure 16 shows the motion of the linear actuator for different R values in the Case 4 study.

The maximum required linear displacement, the velocity, and the acceleration from the analytical results for the different R values are illustrated in Figure 17. The maximum values are expressed in the double amplitude. In the current RTHS system, the maximum R value is limited up to 800 mm for easy installation and the overall system size limitation.

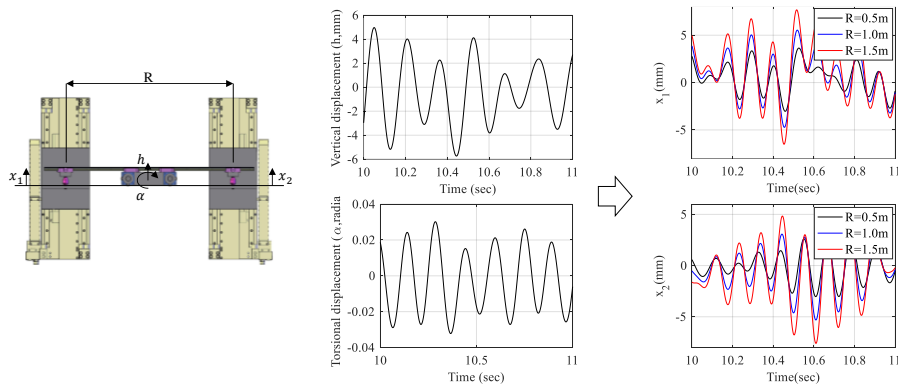


Figure 16. Variation of Linear Motor Target Displacements by Different R Values

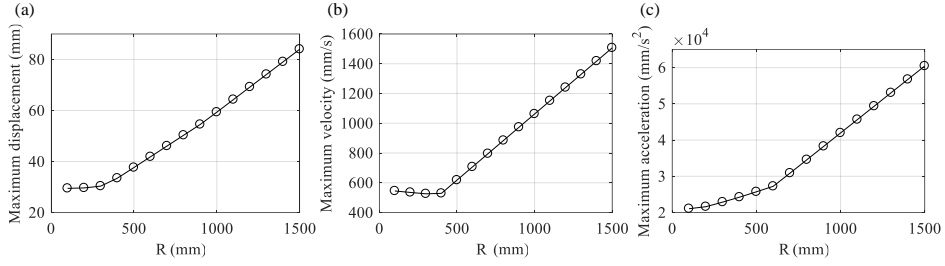


Figure 17. Maximum Values by Different R Values: (a) Displacement (b) Velocity (c) Acceleration

For the $R = 800$ mm condition, the required displacement and the acceleration are 50 mm and 5000 mm/s^2 , respectively. The required peak force including the moving mass is 408 N per one linear motor. To satisfy this requirement, special linear motors are manufactured. The manufactured linear motor moves up to the acceleration of $50,000 \text{ mm/s}^2$ after loading 9 kg of the mass. The corresponding moving range is about 80 mm. The peak force of this motor is over 1800 N. The position feedback of the linear motor is from a high-resolution of $5 \text{ } \mu\text{m}$. And the magnetic encoder and the rail is a bearing-rail type. This motor is able to be updated every 100 to 500 ms through the controller. The overall shape is shown in Figure 18.

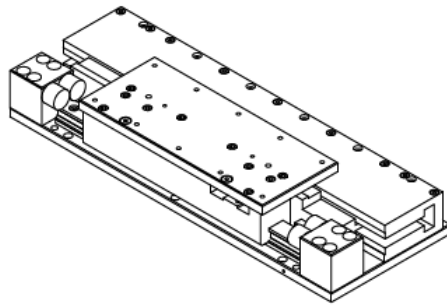


Figure 18. Manufactured Linear Motor

The force obtained in the time-domain analysis is required to be converted to the force at the load cell installation point to obtain the proper capacity since the analytical point is the center of the bridge section. If the gap distance between the load cells(R_{load}) is fixed at 0.3 m, the maximum load (F_{load}) applied at each of the four load cells is 251.4 N. This value is obtained by Eq. (17).

$$F_{load} = [(F_{h_{max}} - F_{h_{min}}) + (F_{\alpha_{max}} - F_{\alpha_{min}}) \div 0.5R_{load}] \div 4 + F_{Int} \quad (17)$$

where, the lift force and the moment with the subscriptions *max* and *min* refer to the maximum and the minimum forces obtained from a time-domain analysis, respectively and F_{Int} is the inertia force. Futek's MBA400 products adequately meet the above requirements. This product is a 2-axis load cell capable of measuring up to 890 N (=200 lb). The sampling frequency is available up to 1300 Hz. The shape of the load cell is shown in Figure 19.

The frame system connects four linear motors and load cells with a bridge section model in a wind tunnel as shown in Figure 20. The central part of the frame system is changeable so that the length of the section model is freely adjusted.



Figure 19. Selected Load Cell (Futek, MBA400)

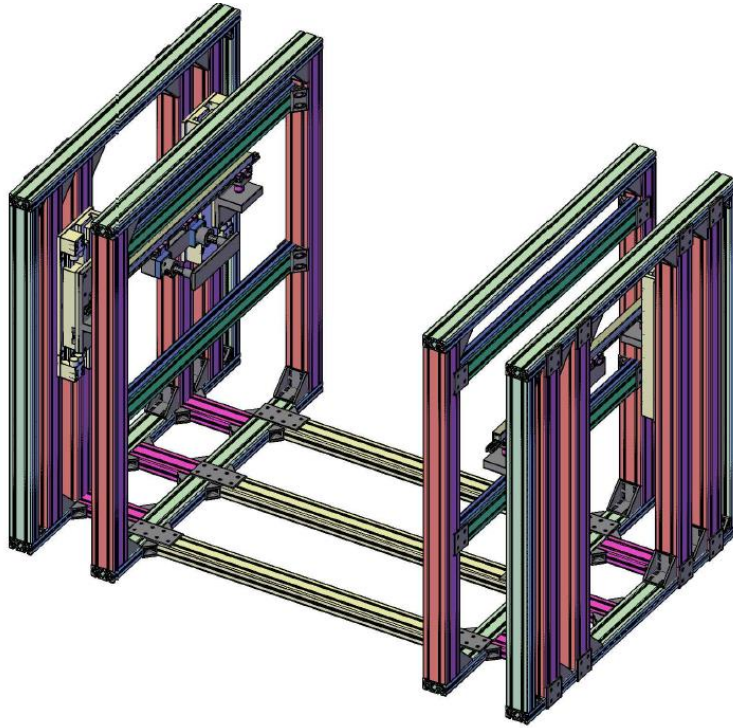


Figure 20. Frame System of the RTHS System

The moving part of the linear motor and the connecting parts are blocked by acrylic to prevent the wind effect. And the distributing plate is installed at the wind direction so that the vortex is not generated at the frame plane.

During the system operation, the aluminum frame part where the linear motor is attached, as shown in Figure 21, is subjected to be a significant force. If the vibration of this frame is great, the whole system is not able to be controlled accurately. This part is designed with the 80×80 aluminum profile at the initial stage. The dynamic analysis is performed with the maximum force periodically acting. The ANSYS student version is used for the dynamic analysis. The meshes are composed, as shown in Figure 22, with 5426 nodes and 1027 elements. Boundary conditions are fixed at both ends.

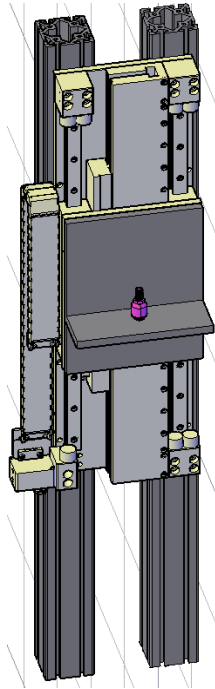


Figure 21. Frame Used for a Dynamic Analysis

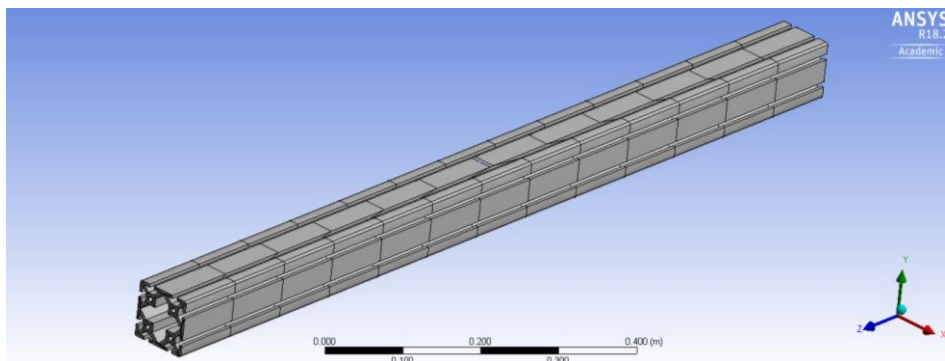


Figure 22. Frame Shape and Mesh Setup in the ANSYS Program

The results show that the frequency of the 1st mode is around 300 Hz. In the wind tunnel tests, there is no resonance issue between the frame model and the system because the system frequency range is set to be between 2 and 10 Hz.

The dynamic analysis is performed at the center point with a harmonic force equivalent to 225 N. The result is shown in Figure 23. The displacement comes out about 10^{-7} m scale. It is concluded that the designed frame system is stable against vibration.

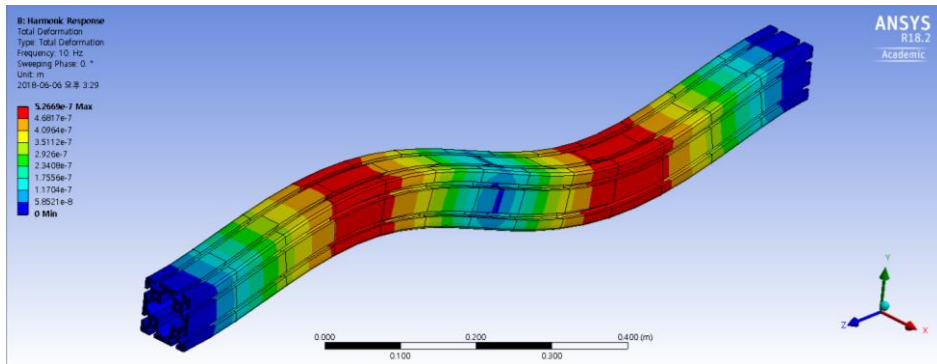


Figure 23. Harmonic Response Result

3.2 Development of the Control Software of the RTHS System

3.2.1 The Schematic of the Control Software

For the comprehensive application of the RTHS system, both hardware machines and control programs are required to be developed. The development of control software of the RTHS system is carried out with three loops: (1) the numerical integration loop, (2) the time-delay compensation loop, and (3) the PID control loop as illustrated in Figure 24.

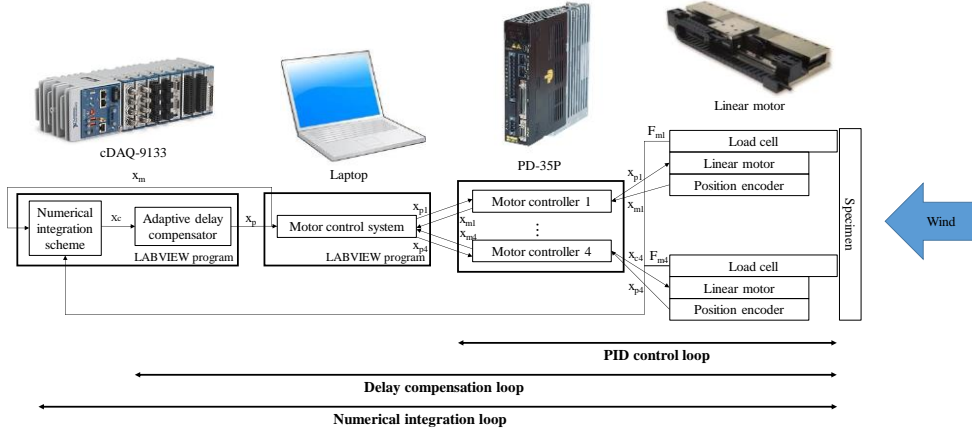


Figure 24. Schematic of the Control Program

The numerical integration loop solves the basic dynamic equation with the central difference approximation scheme. The numerical integration loop determines the target displacement, x_i^c , at each time step. The delay compensation loop compensates the lag and the amplitude difference between the measured displacement, x_i^m , and the target displacement, x_i^c . A proportional–integral–derivative (PID) controller continuously calculates an error value using the difference between a desired target value and a measured one. Then, it corrects the values based on the proportional, the integral, and the derivative terms. Among these, only the parameters related to the position control are used in the proposed RTHS system.

In the essential program of the RTHS system, the time-delay compensation loop and the numerical integration one operate in the cDAQ NI-9133. By operating the two loop programs in the cDAQ rather than in the host computer, the non-deterministic portion of the process, such as system updates, is minimized. The host computer transmits the signal received from the cDAQ to the

motor driver and receives the encoder signal from the motor driver. The motor driver operates the linear motor through the PID loop by the received signal from the host PC. It receives the encoder signal as feedback. In Figure 24, there are 4 sets of a motor controller, a linear motor, and a position encoder. It is due to the fact that the apparatus for a bridge deck section test requires four sets of control systems to simulate the 2DOF motion.

3.2.2 Numerical Integration Loops

To calculate the target displacement in the next time step, the numerical integration loop is needed to be chosen. The numerical integration loop approach is designed to solve the governing equation with the real time measured force and the current system position. Therefore, the first mission in this approach is to define the governing equation of the RTHS system.

The governing equation in the RTHS system is a simple basic dynamic equation as stated in Eq.(18). In this equation, the mass term consists of the numerical mass \mathbf{M}_N and the experimental mass \mathbf{M}_E . The reason why the only mass term is divided into two parts is because the experimental mass creates the inertia force.

$$(\mathbf{M}_E + \mathbf{M}_N)\ddot{\mathbf{X}} + \mathbf{C}\dot{\mathbf{X}} + \mathbf{K}\mathbf{X} = \mathbf{F}_W \quad (18)$$

As mentioned in Section 3.1.3, the measured force by the load cell, \mathbf{F}_M , contains the wind-induced force and the inertia force. Therefore, the measured force is written as Eq.(19).

$$\mathbf{F}_M = \mathbf{F}_W + \mathbf{F}_{Int} = \mathbf{F}_W - \mathbf{M}_E \ddot{\mathbf{X}} \quad (19)$$

where, \mathbf{F}_{Int} is the inertia force caused by movement of the bridge section model. The governing equation turns to be Eq.(20) if the right side of the equation is set to be the measured force term.

$$\mathbf{M}_N \ddot{\mathbf{X}} + \mathbf{C} \dot{\mathbf{X}} + \mathbf{K} \mathbf{X} = \mathbf{F}_M \quad (20)$$

The central difference approximation method is applied to numerically solve the governing equation. This method is based on a finite difference approximation of the time derivatives of displacement. Taking constant time steps, the central difference expressions for the velocity and the acceleration at i^{th} step are described in Eq.(21).

$$\begin{aligned} \dot{\mathbf{X}}_i &\cong \frac{1}{2\Delta t} (-\mathbf{X}_{i-1} + \mathbf{X}_{i+1}) \\ \ddot{\mathbf{X}}_i &\cong \frac{1}{\Delta t^2} (\mathbf{X}_{i-1} - 2\mathbf{X}_i + \mathbf{X}_{i+1}) \end{aligned} \quad (21)$$

where Δt is the time step. Substituting the above equations into the governing equations, Eq.(22) is derived.

$$\mathbf{M}_N \frac{1}{\Delta t^2} (\mathbf{X}_{i-1} - 2\mathbf{X}_i + \mathbf{X}_{i+1}) + \mathbf{C} \frac{1}{2\Delta t} (-\mathbf{X}_{i-1} + \mathbf{X}_{i+1}) + \mathbf{K} \mathbf{X}_i = \mathbf{F}_{M_i} \quad (22)$$

To operate the linear motor with the position control, it is needed that the displacement of the $i + 1^{\text{th}}$ step is represented by the i^{th} and $i - 1^{\text{th}}$ step displacement. Then, the final equation for calculating the $i + 1^{\text{th}}$ step displacement is driven as Eq.(23).

$$\begin{aligned} \mathbf{X}_{i+1} = & \left(\mathbf{M}_N + \mathbf{C} \frac{\Delta t}{2} \right)^{-1} (\Delta t^2 \mathbf{F}_{M_i} + (2\mathbf{M}_N - \Delta t^2 \mathbf{K}) \mathbf{X}_i \\ & - \left(\mathbf{M}_N - \mathbf{C} \frac{\Delta t}{2} \right) \mathbf{X}_{i-1}) \end{aligned} \quad (23)$$

The central difference method sometimes creates numerical “blow up”, giving meaningless results, in the presence of numerical round-off if the time step is not properly short enough. The requirement for the numerical stability is expressed in Eq.(24).

$$\frac{\Delta t}{T_n} < \frac{1}{\pi} \quad (24)$$

In the RTHS system, the interest frequency region is about up to 10 Hz. Then, the minimum requirement for the time step is recommended to be 0.01 sec to avoid any potential stability issue.

The available time step of the control program depends on each hardware system. Therefore, the proper time step is evaluated by corresponding experiment. By changing the time step values in the range between 2 to 10 ms in the control program, the transmissibility of the receiving control signal in a linear motor driver for the two-minute time period is identified. The results are summarized in Table 7.

Table 7. Comparison of Transmissibility for Different Time Steps

Time step(ms)	Updating frequency of control program(Hz)	Number of missing loop per 2 minutes	Transmissibility to linear motor(%)
10	100	4	99.97
5	200	21	99.91
4	250	36	99.88
3.3	300	1358	96.23
2	500	21346	64.42

As shown in Table 7, the transmissibility of 99% is maintained up to the 4 ms time step interval. It is observed that the transmission rate drops sharply in a time interval of less than 4 ms. Obviously, the application of a cDAQ

assures the minimization of the non-deterministic signal loss. However, the use of the host PC for the simple signal transmission between a cDAQ and a motor driver sometimes creates the delay of the signal transmission resulting in relatively poorer values of the transmissibility of signals. In the actual implementation of the RTHS application, the time step value of 5 ms is adopted.

3.2.3 Time-delay Compensation Methods

It is necessary to identify the time-delay characteristic of the total RTHS system itself and to apply for an appropriate time-delay compensation method. A linear motor introduces an inevitable time delay when applying command displacements to a system during a real-time test due to their inherent dynamics. In addition, the signal delay in a motor along with the needed computation time in a control program inevitably creates the time delay. This time delay affects the stability problem and system damping. Therefore, it is necessary to compensate the time delay as much as possible for an accurate experiment. In this dissertation, the time-delay compensation method of Chen et al. (2009, 2010; 2012) is applied.

The basic concept to compensate the time delay by C. Chen and Ricles (2009) is summarized in Figure 25. When the time delay t_d happens, the target signal x_{i+1}^c transmissions to a linear motor arrives at a motor at the i^{th} step plus t_d . The actual motion of a linear motor(x_{i+1}^m) at the $i+1^{\text{th}}$ step happens between the motion (x_i^m) at the i^{th} time step and the motion(x_{i+1}^c) at

the $i+1^{\text{th}}$ time step. The relation between these two motions is linked together as stated in Eq.(25).

$$x_{i+1}^m = x_i^m + \frac{1}{\alpha}(x_{i+1}^c - x_i^m) \quad (25)$$

where $t_d = \alpha\Delta t$, the actual time delay is equal to be $(\alpha - 1)\Delta t$.

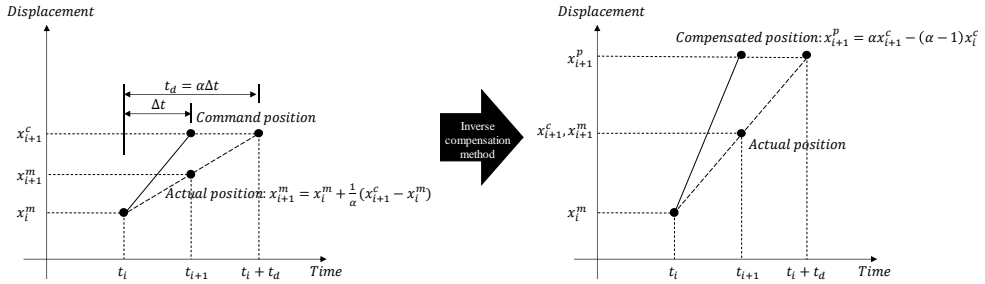


Figure 25. Concept of Time-Delay Compensation Methods Proposed by C. Chen and Ricles (2009)

Applying the discrete z -transform to Eq.(25) leads to a discrete transfer function $G_d(z)$ in Eq.(26).

$$G_d(z) = \frac{X_d^m(z)}{X_c^c(z)} = \frac{1}{(\alpha - (\alpha - 1)z^{-1})} = \frac{z}{\alpha \cdot z - (\alpha - 1)} \quad (26)$$

where $X_d^m(z)$ and $X_c^c(z)$ are the discrete z -transforms of x_{i+1}^m and x_{i+1}^c , respectively. Chen proposed to use the inverse of the above equation for the actuator delay compensation in a real-time testing, whereby the equivalent discrete transfer function for the resulting the inverse compensation method is summarized in Eq.(27).

$$G_c(z) = \frac{X_d^p(z)}{X_c^c(z)} = \frac{\alpha \cdot z - (\alpha - 1)}{z} \quad (27)$$

where $X_p^m(z)$ is the discrete z-transform of x_{i+1}^p , and x_{i+1}^p are the predicted displacements. Applying the inverse discrete z-transform to the above equation, the extrapolation form corresponding to the inverse compensation in the time domain is expressed as Eq.(28).

$$x_{i+1}^p = \alpha x_{i+1}^c - (\alpha - 1)x_i^c \quad (28)$$

This time delay compensation approach corrects the time delay with the constant time delay value already pre-set before the actual computation. Therefore, this approach is not adequate to correct an inadvertent error caused by wrong values of the pre-set values and time-variant errors from the experiments. To overcome this limitation, Chen et al. (2010; 2012) introduced the adaptive term for the amplitude and the phase. With this adaptive compensation, Eq.(27) is modified as Eq.(29) with the new addition of the adaptive term $\Delta\alpha$ for the phase and Δk for the amplitude respectively.

$$G_c(z) = \frac{X_d^p(z)}{X_d^c(z)} = \frac{(k_{est} + \Delta k)[(\alpha_{es} + \Delta\alpha) \cdot z - (\alpha_{es} + \Delta\alpha - 1)]}{z} \quad (29)$$

where α_{es} is the estimated actuator delay, $\Delta\alpha$ is an adaptive parameter for the phase error, k_{est} is the initial estimate of the proportional gain for the motor response with the usual value of 1.0. and Δk is an adaptive parameter for the amplitude error. An adaptive control law is used to determine $\Delta\alpha$ and Δk based on the TI and AI , where $\Delta\alpha$ and Δk are defined in Eqs. (30) and (31).

$$\Delta\alpha(t) = k_p \cdot TI(t) + k_i \cdot \int_0^t TI(\tau) dt \quad (30)$$

$$\Delta k(t) = k_p^k \cdot AI(t) + k_i^k \cdot \int_0^t AI(\tau)dt \quad (31)$$

where k_p and k_p^k are the proportional adaptive gains of the adaptive control law, and k_i and k_i^k are the integrative adaptive gains of the adaptive control law. The calculation of the tracking indicator, TI , formulated by Mercan and Ricles (2007) and the amplitude indicator, AI , are defined by Eqs. (32) and (33).

$$TI_{i+1} = 0.5(A_{i+1} - TA_{i+1}) \quad (32)$$

$$AI_{i+1} = 0.5(B_{i+1} - TB_{i+1}) \quad (33)$$

where A_{i+1} and TA_{i+1} are the enclosed and the complementary enclosed areas at the time step of $i + 1^{\text{th}}$, and B_{i+1} and TB_{i+1} are the difference in the amount of the change between the $i + 1^{\text{th}}$ step and the i^{th} step of the target value and the actual measured value as defined in Eqs.(34) to (37).

$$A_{i+1} = A_i + 0.5(x_{i+1}^c + x_i^c)(x_{i+1}^m - x_i^m) \quad (34)$$

$$TA_{i+1} = TA_i + 0.5(x_{i+1}^c - x_i^c)(x_{i+1}^m + x_i^m) \quad (35)$$

$$B_{i+1} = B_i + 0.5(x_{i+1}^c - x_i^c)(x_{i+1}^c - x_i^c) \quad (36)$$

$$TB_{i+1} = TB_i + 0.5(x_{i+1}^c - x_i^c)(x_{i+1}^m - x_i^m) \quad (37)$$

Before direct applying the adaptive time-delay compensation method to the RTHS system at once, it is needed to optimize the values for the time-delay compensation and check the feasibility of the compensation method to the RTHS system. The preliminary setting to measure the value is illustrated in Figure 26. In addition to a linear motor, a driver, a cDAQ and a host computer, a circuit breaker, and a noise filter along with the 3-phase power system are

applied to eliminate any potential electrical noise. The time-delay value is estimated by the bode plot between the target command displacement value and the actual measured one using the white noise signal as a force in a numerical integration loop. The white noise signal is normalized to be 2 N. The band filtered signal at the range of 0.1 and 6 Hz is used during the time frame of 100 seconds. The input values of the mass is equal to 5 kg, the damping ratio set to be 0.3 %, and the natural frequency of 2 Hz is used for the system analysis.

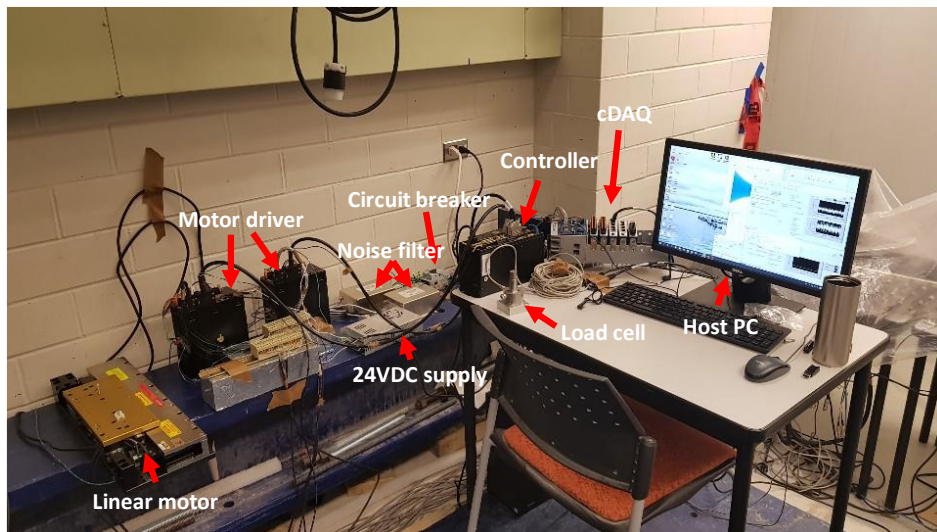


Figure 26. Setup for Verifying System Operation

Experimental results are summarized in Figure 27 and Figure 28. As shown in Figure 27, there is a consistent time delay between the target and the measured displacement values. The same results are summarized in Figure 28. The results from the Bode plots show the error in the magnitudes and the phase by the frequency. Figure 28 (a) shows that amplitude error increases as

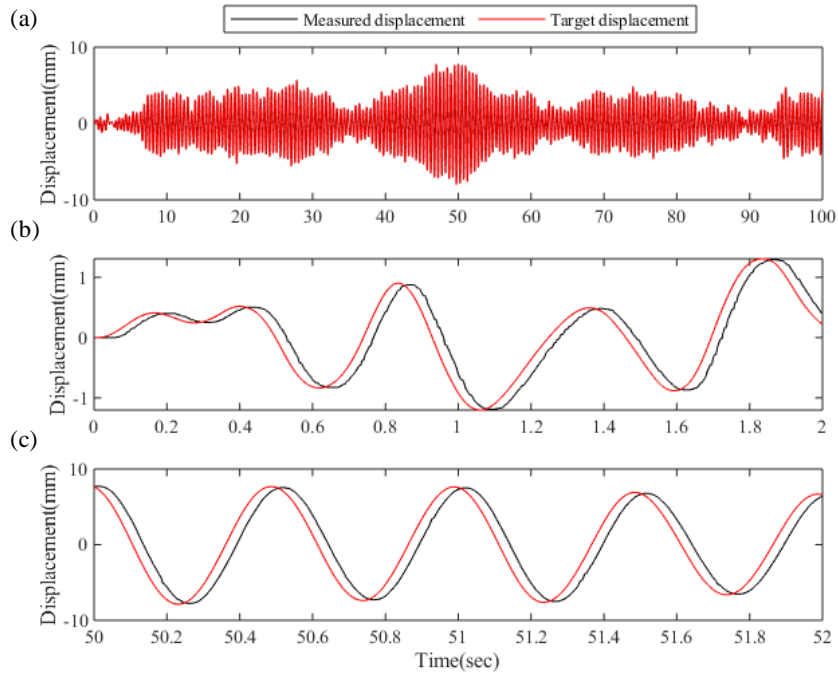


Figure 27. Comparison of Target and Measured Displacements before Applying the Compensation Method (a) 0~60 sec Region (b) 0~2 sec Region (c) 50~52 sec Region

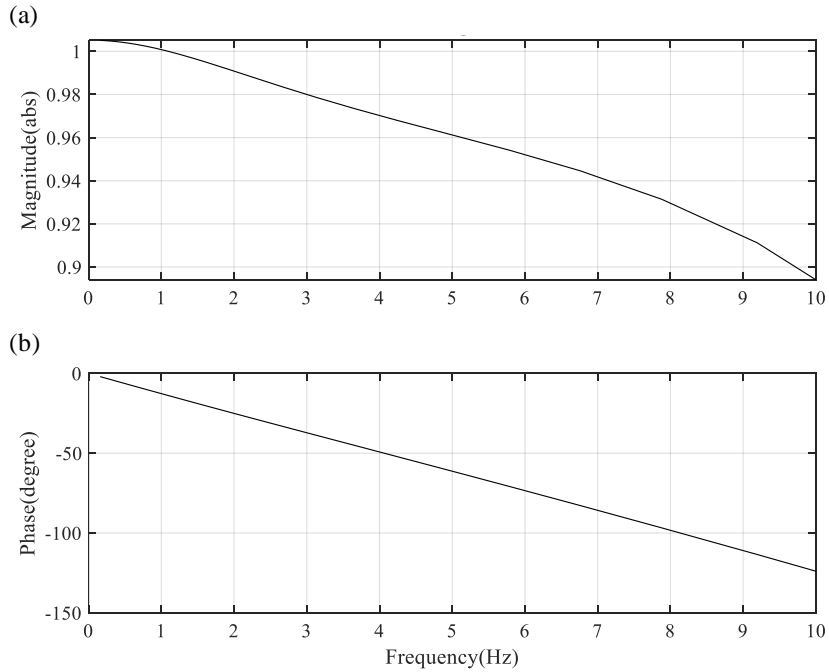


Figure 28. Bode Plots (a) Magnitude (b) Phase

the frequency increases. The results for the phase indicate that the linear trend results in the constant time delay regardless of frequencies. Since there is a phase of about -110 degrees at 9 Hz, it indicates that 34 ms time-delay happens in the RTHS system.

The time-delay compensation method is applied for the same experiment conditions. The same values of the system properties and the white noise forces are used with the time-delay values of $\alpha_{es} = 32$ ms, $k_{est} = 1.0$, $k_p = 0.4$, $k_p^k = 1$, $k_i = 0.04$ and $k_i^k = 0.1$ to compensate the corresponding time-delay.

The results are summarized in Figure 29. In early time steps, there is slight difference between the target and measured displacement values since enough adaptive terms are not developed yet. However, as time passes all adaptive terms are properly acted to find the true time-delay values. As illustrated in Figure 29, after a sufficient time, it is confirmed that the time delay compensation method acts adequately for the RTHS system.

Even those proposed time-delay compensation method corrects the impact from the time-delay, the relatively high value time-delay leads to experimental errors and limits the available experiment conditions. Therefore, it is highly recommended to fully understand the detailed reasons to create the time-delay in the RTHS systems. As summarized in Figure 30, three issues for the time-delay are identified. These three factors are (1) the time which takes to send the command signal in the host PC to the motor driver and to

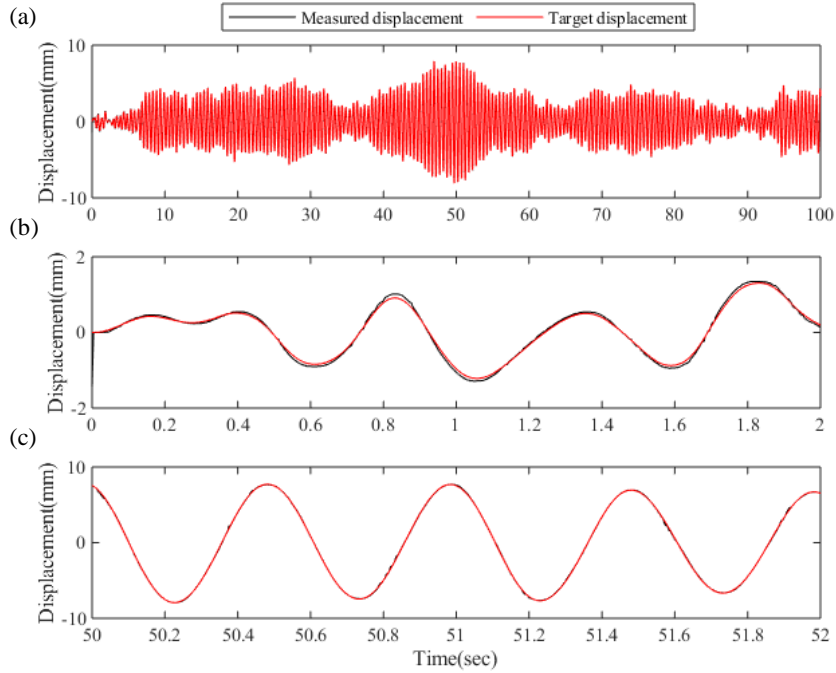


Figure 29. Comparison of Target and Measured Displacement Values after Applying the Compensation Method (a) 0~60 sec Region (b) 0~2 sec Region (c) 50~52 sec Region

operate the PID loop in the driver, (2) the time to actually activate the LabVIEW program in the host PC, and (3) the communication time between the cDAQ and the host PC.

To quantify the time delay by the 1st factor, the actual time for the signal communication is measured by the ACR program with the direct connection between the host PC and the driver. As shown in Figure 31, there is one-time step, 10 ms, the time gap between the command signal and the measured one. This in practice creates the actual 5 to 15 ms time-delay in the proposed RTHS system.

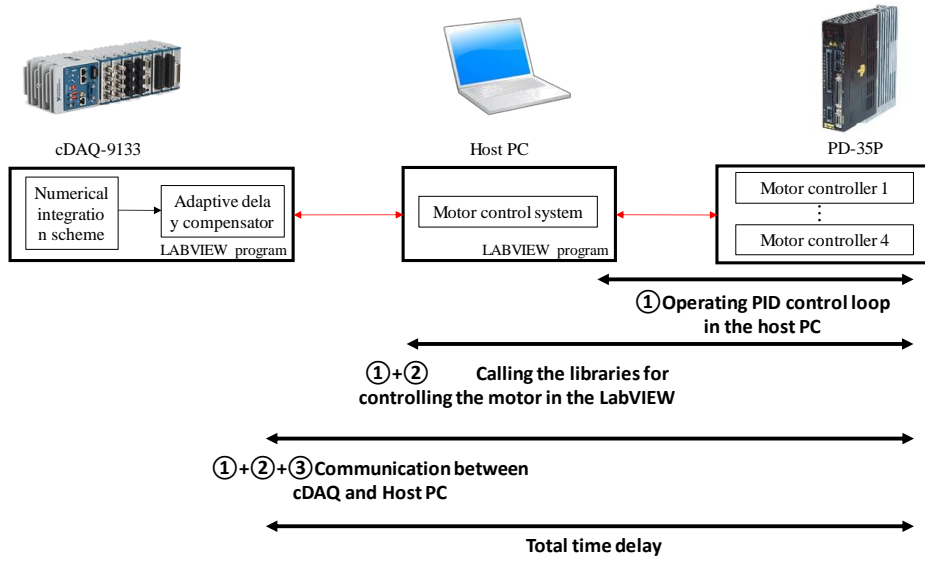


Figure 30. The Possible Process Causing a Time-Delay in a Control Program

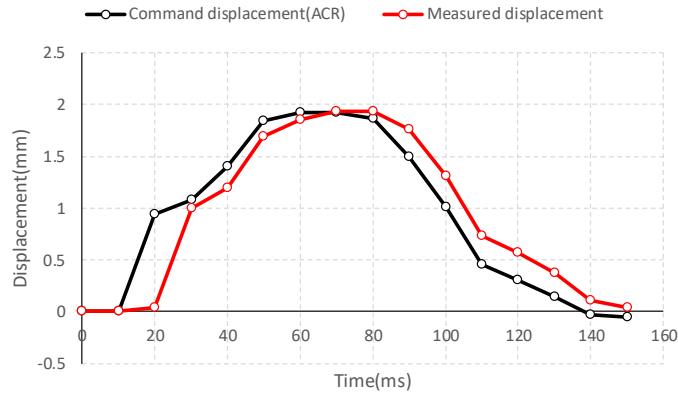


Figure 31. Measurement of the Time-Lag between the Host PC and the PID Loop Using the ACR Program

To identify the time-delay by the 2nd factor, the time required to run the PID loop in a motor driver using the LabVIEW program in the main host PC program is measured. As shown in Figure 32, the results for the phase indicate

that the linear trend results in the constant time delay regardless of frequencies. The results show that the time-delay by the 2nd factor is within the range of 13 to 23 ms.

The total delay-time from three factors is 34 ms. Therefore, with the quantitative results for the time-delays from the 1st and the 2nd factors, the impact of the 3rd factor is easily estimated as 6 ms. To minimize the total time-delay of the signals, the contributions from these three factors are recommended to be eliminated or reduced in future studies.

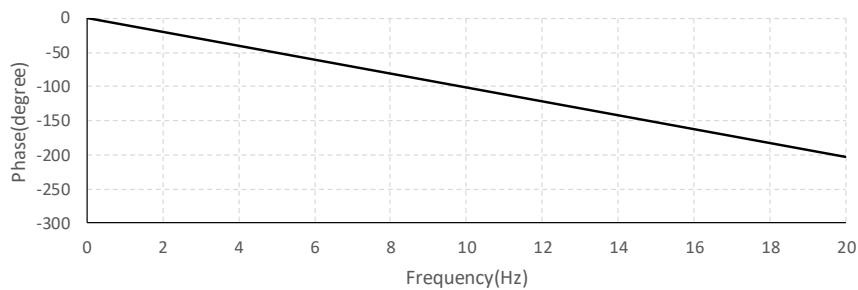


Figure 32. Results of Phase Analysis to Identify the Time-Delay by the 2nd Factor

CHAPTER 4

VERIFICATION OF THE APPLICABLE RANGE OF THE RTHS SYSTEM

4.1 Determination of the Target Range of Input Variables in the RTHS Process

The governing equation of the RTHS system is summarized as Eq. (20). It is re-written as Eq. (38) since there is no coupled term for the mass, the damping, and the stiffness.

$$\begin{aligned} \begin{bmatrix} \bar{m}_N & 0 \\ 0 & 2I_E + \bar{I}_N \end{bmatrix} \begin{bmatrix} \ddot{h} \\ \ddot{\alpha} \end{bmatrix} + \begin{bmatrix} 4\pi\bar{m}_N\bar{f}_h\bar{\xi}_h & 0 \\ 0 & 4\pi(I_E + \bar{I}_N)\bar{f}_\alpha\bar{\xi}_\alpha \end{bmatrix} \begin{bmatrix} \dot{h} \\ \dot{\alpha} \end{bmatrix} \\ + \begin{bmatrix} \bar{m}_N(2\pi\bar{f}_h)^2 & 0 \\ 0 & (I_E + \bar{I}_N)(2\pi\bar{f}_\alpha)^2 \end{bmatrix} \begin{bmatrix} h \\ \alpha \end{bmatrix} = \begin{bmatrix} F_{h_M} \\ F_{\alpha_M} \end{bmatrix} \end{aligned} \quad (38)$$

where, the subscripts E , N and M mean the experimental, the numerical, and the measured values, respectively, the subscripts h and α denote the vertical and the torsional components, respectively, the symbol ‘—’ denotes the numerically input value in the program, m and I are the mass and the mass moment of the inertia, respectively, f is the natural frequency, and ξ is the damping ratio.

The key inputs for testing a RTHS program are the natural frequency, the numerical mass, and the target damping value. These values are required as inputs of the LabVIEW program as illustrated in Figure 33.

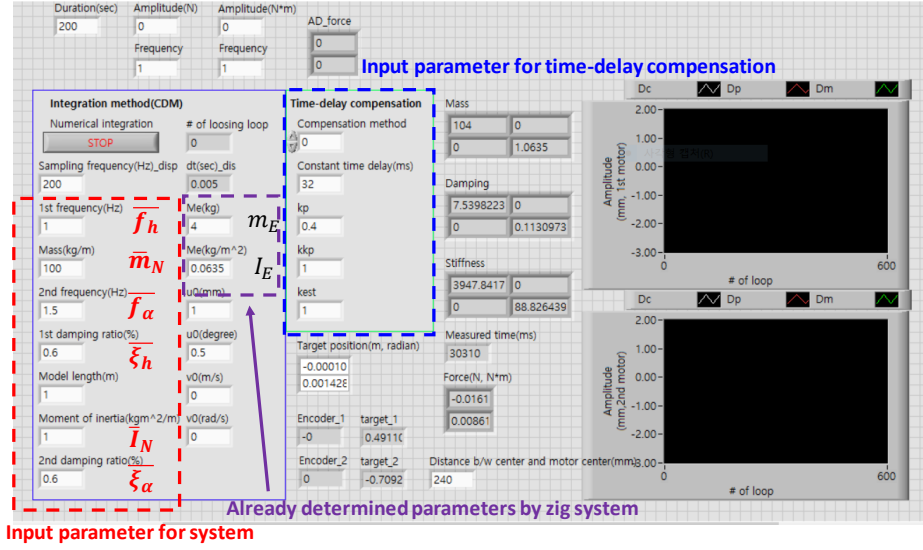


Figure 33. The Window of the LabVIEW Program to Run the Cases for the RTHS System

As already described, the mass is classified into two subjects, the numerical mass, \bar{M}_N , and the experimental mass, M_E . Here the numerical mass is defined as the target mass value minus the experimental mass one. Therefore, the numerical mass value is affected by the absolute value of the experimental mass. In addition, as explained in the previous section, the measured force includes the inertia force by the experimental mass. Therefore, the impact of the measured force to the entire system depends on the ratio of the experimental mass to the total target mass. The contributions of the experimental mass to the total target mass are defined as the Mass ratio, M_R , which contains with m_R and I_R in Eq.(39).

$$m_R = \frac{m_E}{m_E + \bar{m}_N}, \quad I_R = \frac{I_E}{I_E + \bar{I}_N} \quad (39)$$

where the experimental mass is set by the design of the experimental system. As illustrated in Figure 34, it is determined by the connecting zig system and the section model. The currently assumed values for the experimental mass and the mass moment of the inertia of the section model and the proposed zig systems are as follows; $m_E = 1.5$ kg, and $I_E = 0.007$ kg·m². Then, the actual ranges of the mass ratio and the mass moment of the inertia for the RTHS system to simulate wind tunnel tests are calculated to be in the ranges of $m_R = 6.1 \sim 18.1$ and $I_R = 0.4 \sim 7.0$ when listed values in Table 3 are utilized.

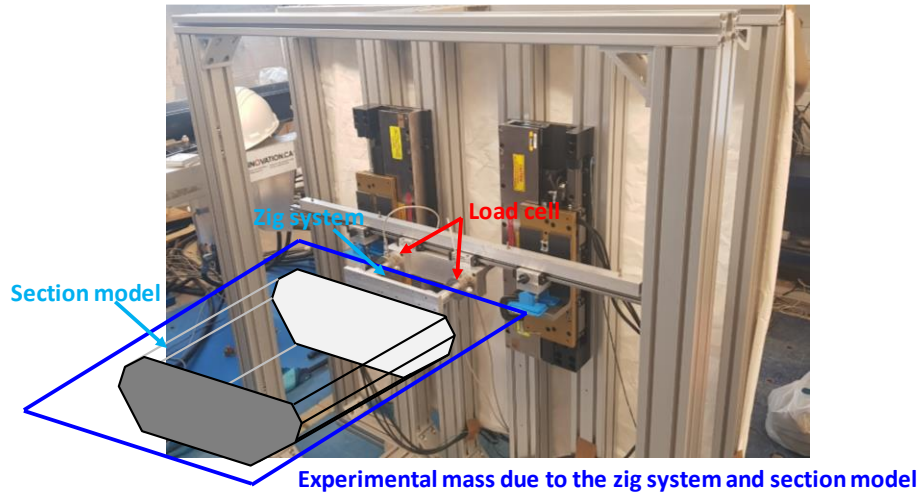


Figure 34. Illustration of the System Components Determining the Experimental Mass of the RTHS System

For given input parameter values prescribed in Table 3, the ranges of the target natural frequencies, applicable to the wind tunnel tests are estimated as; $f_h = 2,3$ Hz and $f_\alpha = 2,3,4,5$ Hz.

For the experiment on the two-degree of the freedom, the values of the target frequency ratio, f_R , representing the ratio between the target vertical natural frequency and the torsional frequency are set to be within the range of 1.2~2.0. Also, the target damping ratio is determined to be within the range of 0.2~1.0% to represent all feasible damping cases in the wind tunnel tests.

4.2 Preliminary Tests for Setting the Feasible Conditions of the RTHS System

4.2.1 Objects and Analysis Methods for Preliminary Tests

To test the proper functioning of the RTHS system under the input parameter values given in Section 4.1, a series of the experiments are proposed. Throughout these experiments, the available ranges of the following parameters are determined; (1) the mass ratio, \mathbf{M}_R (2) the target damping ratio, $\bar{\xi}$ (3) the target natural frequency, \bar{f} , and (4) the frequency ratio, f_R , for the 2DOF system

Each experiment is performed with different values of the four parameters. Then, the results of the displacements are evaluated with the realized damping ratios, ξ_h^* and ξ_a^* , the realized vibration frequencies, f_h^* and f_a^* , and the rRMSE values.

All these experiments assume the free-vibration with decaying for given values of the initial displacement. The damping ratio is determined by the application of the modified Ibrahim Time Domain(MITD) method (Sarkar et al. (1994). The damping ratio is measured by the data with the displacement values within the 20 to 80 % range of the maximum displacement values. Then, the frequency is calculated by the Fast Fourier Transform (FFT) method. The rRMSE values are estimated by comparing the displacement values from the actual measurements and the numerically calculations with the corresponding input parameters. In this assessment, the results satisfying the criteria of $\text{rRMSE} < 30\%$ are solely applied to assure the validity of RTHS system.

4.2.2 Experimental Results with Given Mass Ratios

The impact of the mass ratio is scrutinized by vertical/ torsional direction experiments. Firstly, the effect of the mass ratio, m_R , in the vertical direction is performed. The values of the input parameters are $m_E = 4$ kg, $\bar{\xi}_h = 0.6\%$, $\bar{f}_h = 2$ Hz, and the initial displacement set to be 3 mm.

The results are illustrated in Figure 35 to Figure 37. In Figure 36, the 10% error line is plotted as the dotted one, based on the value of the target damping of 0.6 %. The experiments are done with the values of m_R in the ranges 1~20 %. The realized damping results indicate that the stable value of the realized damping ratio is achieved with the m_R values up to the 8% as illustrated in Figure 36. The following experiments conducted with higher m_R

values, produce the high damping ratios compared with the target values. Also, it shows the subtle difference in the realized variation frequency for the higher value of m_R such as 13 % as shown in Figure 35. As illustrated in Figure 37, if the values of the target m_R are less than 13%, those data are categorized into fair condition one. The actual test results from the RTHS system application show the value range up to 8% in terms of the realized damping, the frequency, and the rRMSE values. In actual implementations, this limitation is eliminated by reducing the experimental mass, which in turn minimizes the value of m_R .

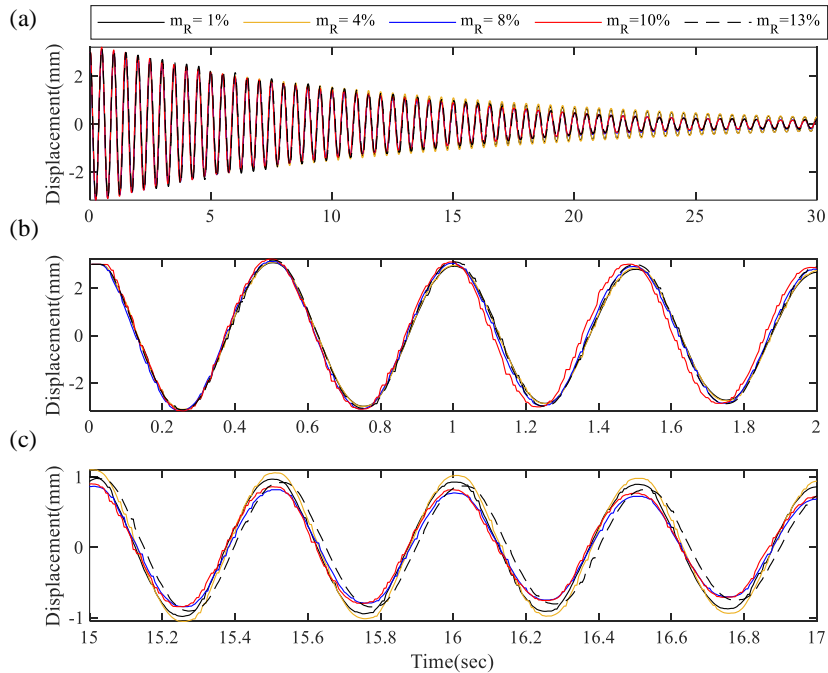


Figure 35. Displacements in the Vertical Direction for Different Values of m_R

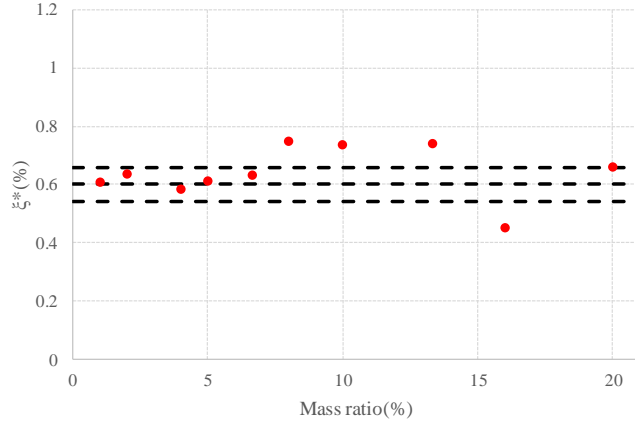


Figure 36. Realized Damping Ratios in the Vertical Direction for Different Values of m_R for a Given Target Damping Ratio of 0.6 %

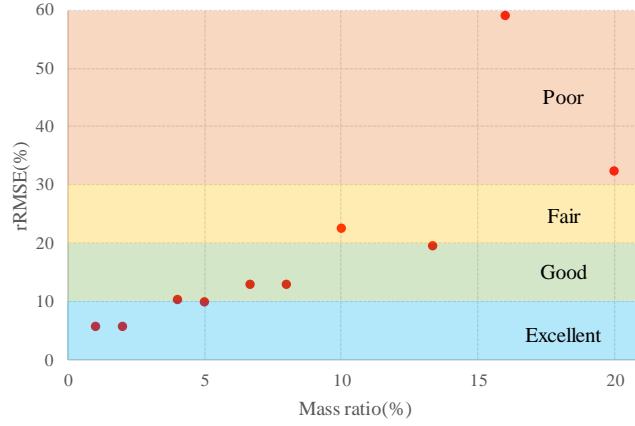


Figure 37. rRMSE in the Vertical Direction for Different Values of m_R for a Given Target Damping Ratio of 0.6 %

To assess the impact of I_R in the torsional direction, the experiments are designed with the following input parameter values; $I_E = 0.041 \text{ kg} \cdot \text{m}^2$, $\bar{\xi}_\alpha = 0.6 \text{ %}$, $\bar{f}_\alpha = 2 \text{ Hz}$, and the initial displacement= 1.5° .

The experimental results are illustrated in Figure 38 to Figure 40. As illustrated in Figure 39, all the experimental values of the realized damping ratios successfully lie within the 10 % error bound. However, the results illustrated in Figure 38 show the slight discrepancies between the realized vibration frequency and the target values for the I_R values greater than $I_R = 8\%$. For the rRMSE value studies, the results with $I_R = 13\%$ are not practically applicable. In summary, when the value of I_R is less than 8%, the proposed RTHS system works fine. In fact, in the real experimental conditions, all the target values of I_R are within the range of 0.4 to 7.0% so that all the experimental results are well matched with the target values.

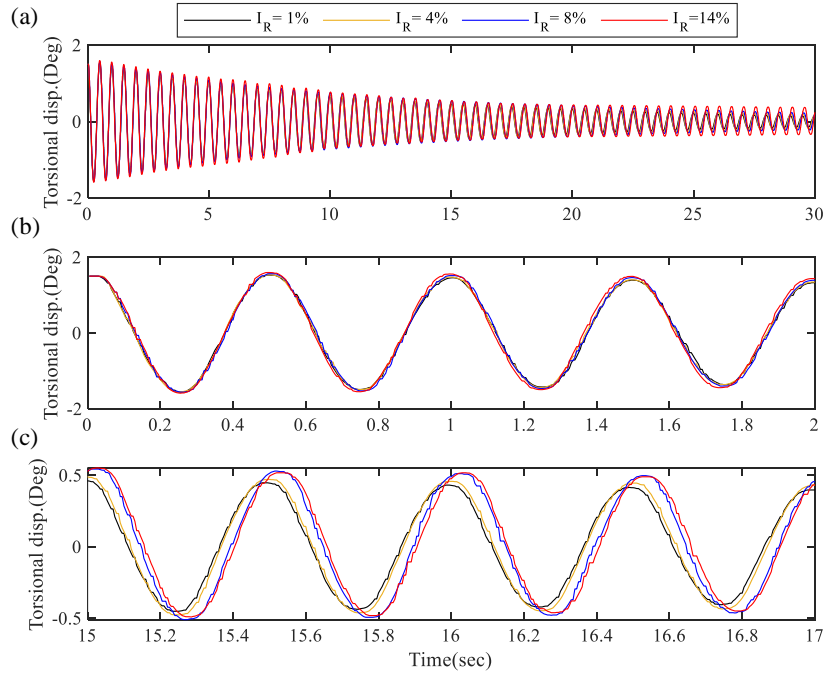


Figure 38. Responses in the Torsional Displacements for Different I_R

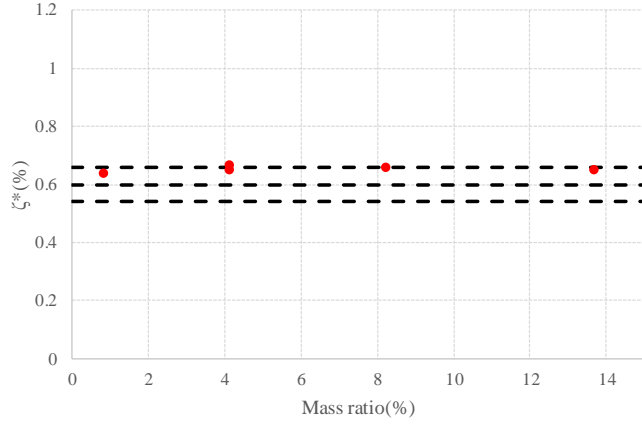


Figure 39. Responses in the Realized Damping Ratios for Different I_R in the Torsional Direction for a Given Target Damping Ratio of 0.6 %

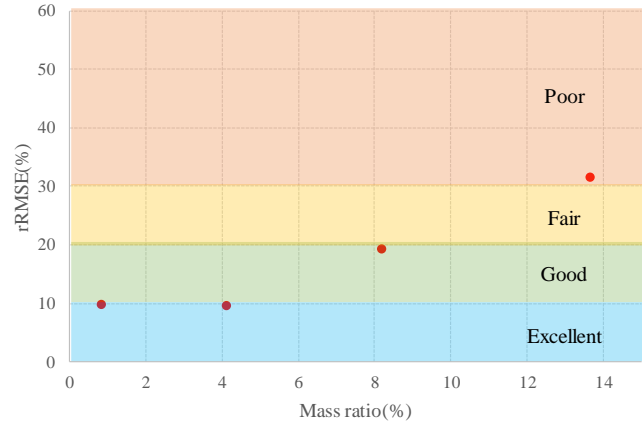


Figure 40. rRMSE in the Realized Damping Ratios for Different I_R in the Torsional Direction for a Given Target Damping Ratio of 0.6 %

4.2.3 Experimental Results with Target Damping

To assess the impact of the target damping in the vertical/torsional direction to the RTHS system, the experiments are designed with the following input parameter values. Firstly, the experiments are done in the vertical direction

with the following input parameter values; $m_E = 4$ kg, $\bar{m}_N = 96$ kg, $m_R = 4\%$, $\bar{f}_h = 2$ Hz, and the initial displacement= 3 mm.

These experiments are done with the input parameter of $m_R = 4\%$ to get the stable results. As shown in Figure 41 to Figure 43, all stable results for the realized vibration frequency, the realized damping ratio and the rRMSE values are estimated. This assures that for the given damping ratios within the range of 0.2~1.0% in the vertical direction. All designed experiments are successfully functioned.

To understand the impact of the target damping ratios in the torsional direction, the following parameter values are applied in the analysis; $I_E = 0.041$ kg·m², $\bar{I}_N = 0.459$ kg·m², $I_R = 8.2\%$, $\bar{f}_\alpha = 2$ Hz, and the initial displacement= 1.5°.

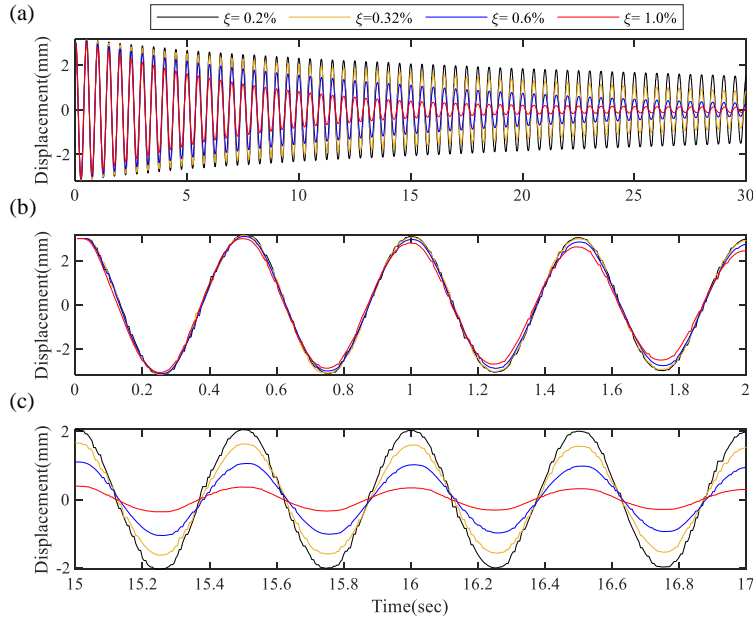


Figure 41. Responses in Displacements for Different Target Damping Ratios in the Vertical Direction

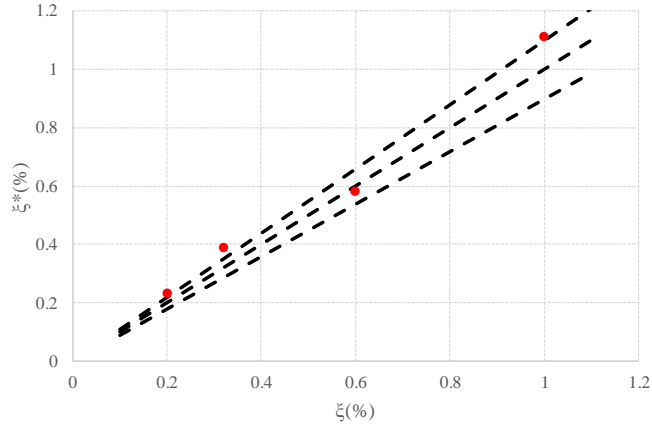


Figure 42. Responses in Realized Damping Ratios for Different Target Damping Ratios in the Vertical Direction

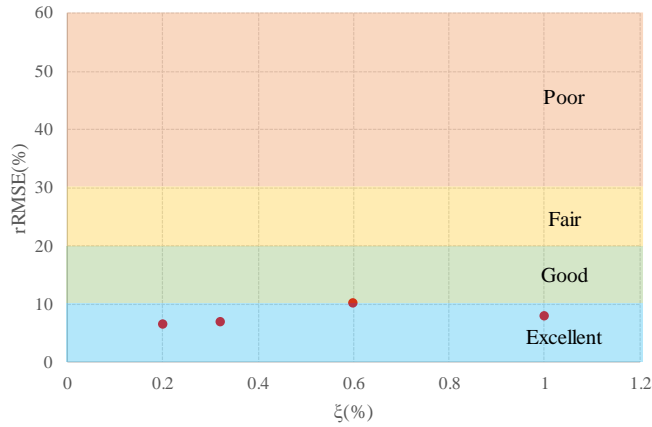


Figure 43. rRMSE for Different Target Damping Ratios in the Vertical Direction

Results are illustrated in Figure 44 to Figure 46. Similar to the results for the vertical direction, the similar stable results are produced for both the realized damping ratios and the rRMSE values. This leads to the conclusion that proposed design of the RTHS system is good enough for the further applications within the range of the damping ratio values between 0.2 and 1.0%.

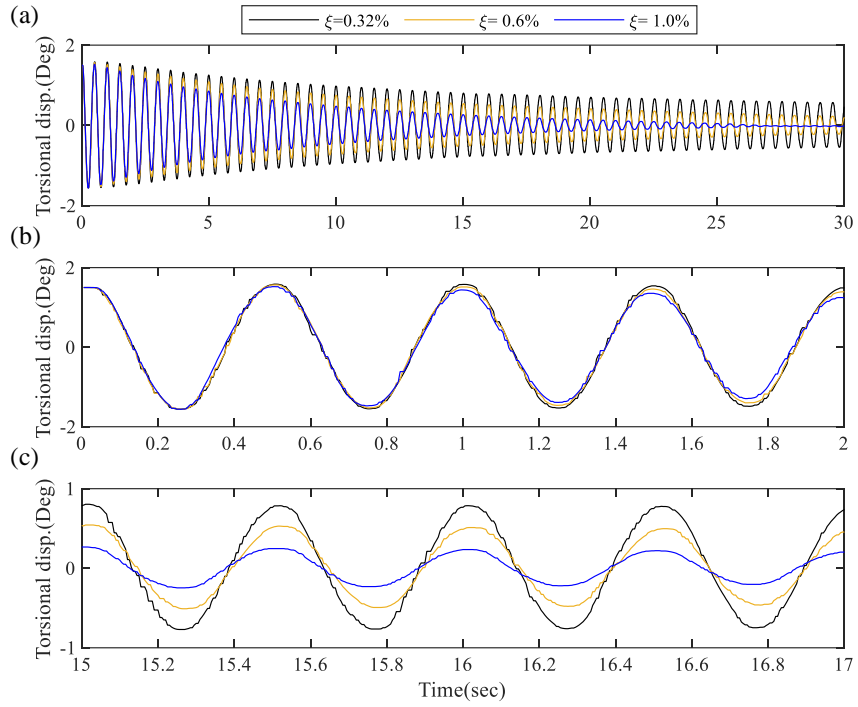


Figure 44. Responses in Displacements for Different Target Damping Ratios in the Torsional Direction

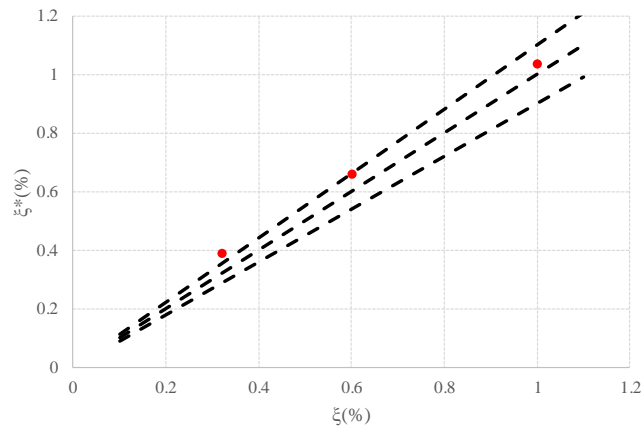


Figure 45. Realized Damping Ratios for Different Target Damping Ratios in the Torsional Direction

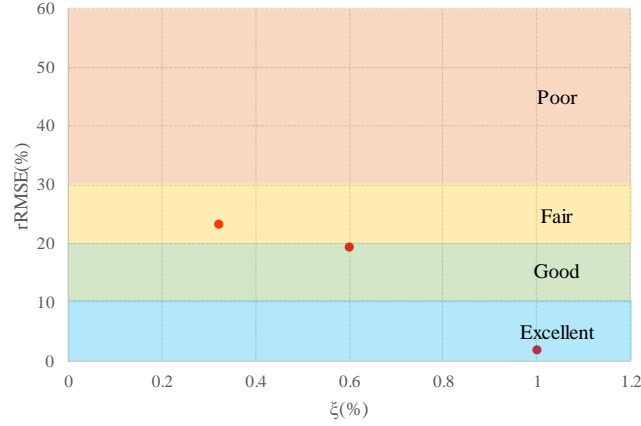


Figure 46. rRMSE Values for Different Target Damping Ratios in the Torsional Direction

4.2.4 Experimental Results with Given Target Frequencies

To understand the impact of the target natural frequency, the target frequency of the system is varied for the vertical/torsional direction while other parameter values are fixed.

Firstly, the vertical direction experiments are performed with the following input parameter values; $m_E = 4$ kg, $\bar{m}_N = 96$ kg, $m_R = 4$ %, $\bar{\xi}_h = 0.6$ %, and the initial displacement= 3 m.

For the given parameter values as described above, the target natural frequency is changed within the range of 2~5 Hz. All the results for the displacements are illustrated in Figure 47. For the fair comparison of the time series data attained with different natural frequencies, the values in the x axis are normalized with cycles. All the results for the realized damping ratios and the rRMSE values are depicted in Figure 48 and Figure 49. Results show that the

proposed RTHS system is well functioned for the values of \bar{f}_h up to the 3 Hz level.

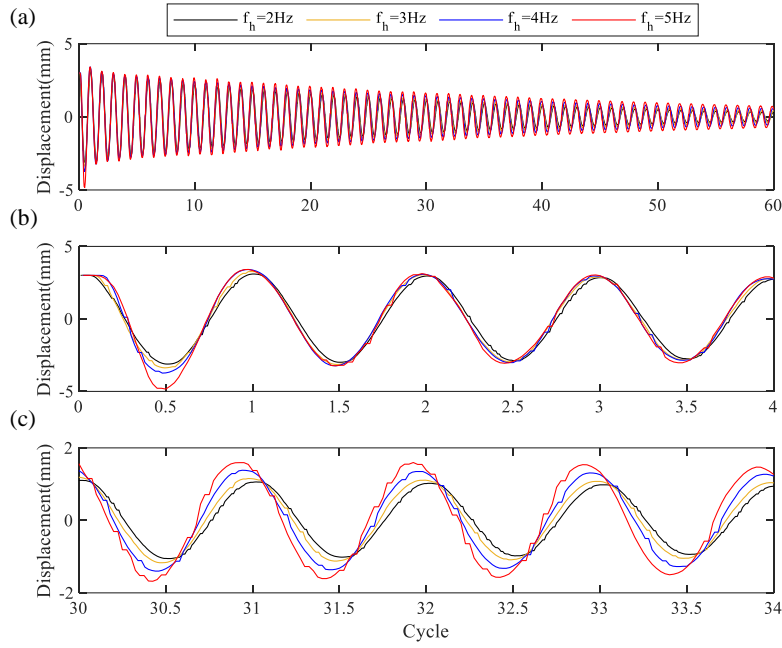


Figure 47. Responses in Vertical Displacements for Different Target Vertical Frequencies

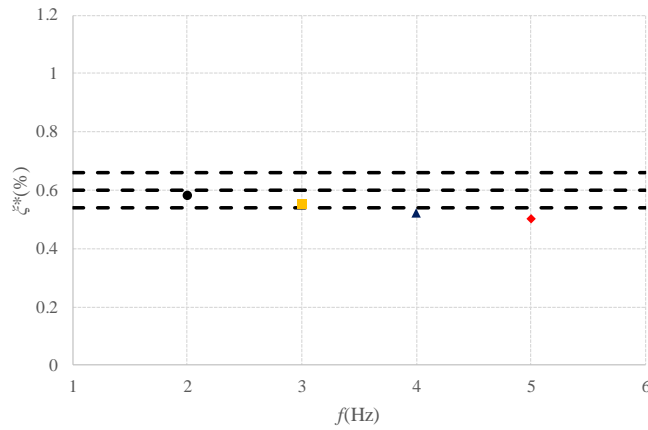


Figure 48. Realized Damping Ratios for Different Target Frequencies in the Vertical Direction for a Given Target Damping Ratio of 0.6 %

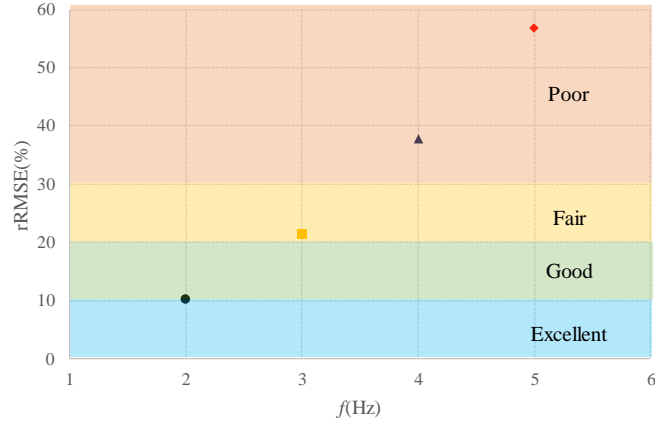


Figure 49. rRMSE Values for Different Target Frequencies in the Vertical Direction for a Given Target Damping Ratio of 0.6 %

Secondly, the torsional direction experiments are performed while varying the value of the target natural frequencies within the range of 2 to 5 Hz with the following input parameter values; $I_E = 0.041 \text{ kg} \cdot \text{m}^2$, $\bar{I}_N = 0.959 \text{ kg} \cdot \text{m}^2$, $I_R = 4.1 \%$, $\bar{\xi}_\alpha = 0.6 \%$, and the initial displacement = 1.5° .

Results are illustrated in Figure 50 to Figure 52. As shown in Figure 50, the stable frequency values are maintained within the target frequency range up to the 4 Hz. Figure 51 and Figure 52 show that the proposed system functions stably well with the target frequency up to 4 Hz. This 4 Hz value is lower than the values of $f_\alpha = 2 \sim 5 \text{ Hz}$ predetermined in the Section 4.1. This limitation of the proposed RTHS system in both vertical/torsional directions under the high target frequency conditions comes from the significantly higher values of the time-delay, around 34 ms, compared with the time step of 5 ms in the proposed RTHS system.

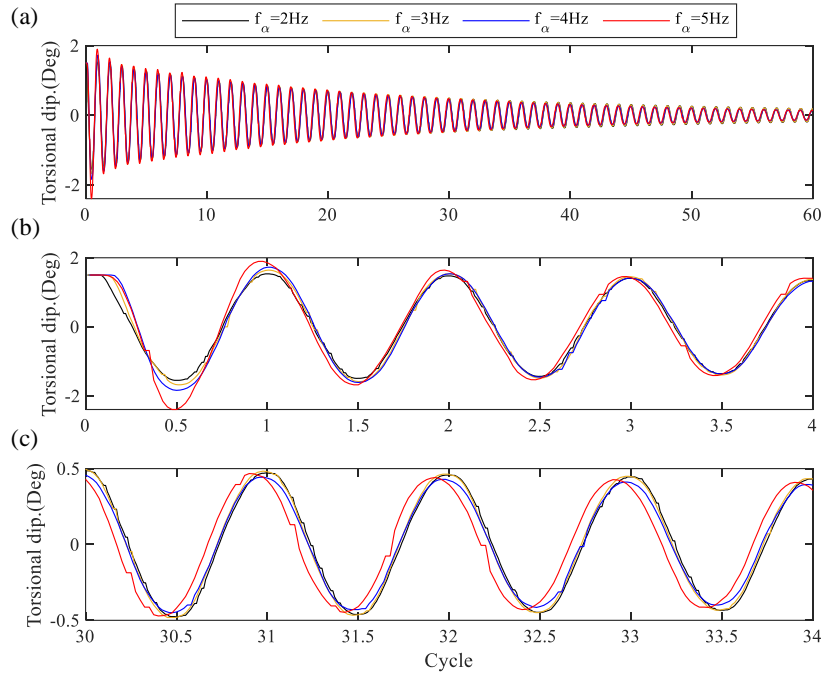


Figure 50. Responses in Displacements for Different Target Frequencies in the Torsional Direction

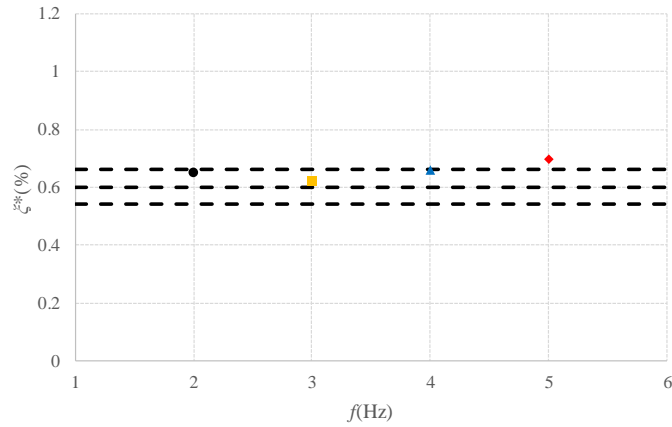


Figure 51. Realized Damping Ratios for Different Target Frequencies in the Torsional Direction for a Given Target Damping Ratio of 0.6 %

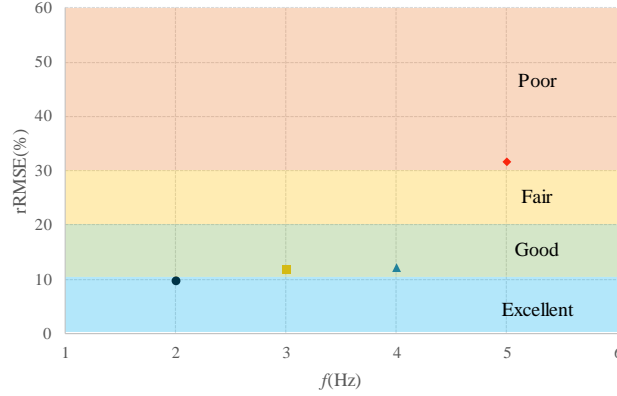


Figure 52. rRMSE Values for Different Target Frequencies in the Torsional Direction for a Given Target Damping Ratio of 0.6 %

This discrepancy inevitably creates the big initial error creating the side impact of the accumulation of error on the adaptive values. When the time-delay in the proposed system by three factors described in the previous section is properly reduced, the proposed system is to be adequately operated.

4.2.5 Experimental Results with Different Values of Frequency Ratio in the 2DOF Movement

The final experiments are set up to understand the impact of the ratio of the target natural frequency f_R in the two-dimensional Degree of Freedoms (2DOF) set-ups. The following input parameter values are used for the experiments; $m_E = 4$ kg, $\bar{m}_N = 96$ kg, $m_R = 4$ %, $\bar{\xi}_h = 0.6$ %, the initial vertical displacement = 5 mm, $I_E = 0.043$ kg·m², $\bar{I}_N = 0.957$ kg·m², $I_R = 4.3$ %, $\bar{\xi}_\alpha = 0.6$ %, and the initial torsional displacement = 0.5°.

All results of the responses are illustrated in Figure 53 to Figure 56.

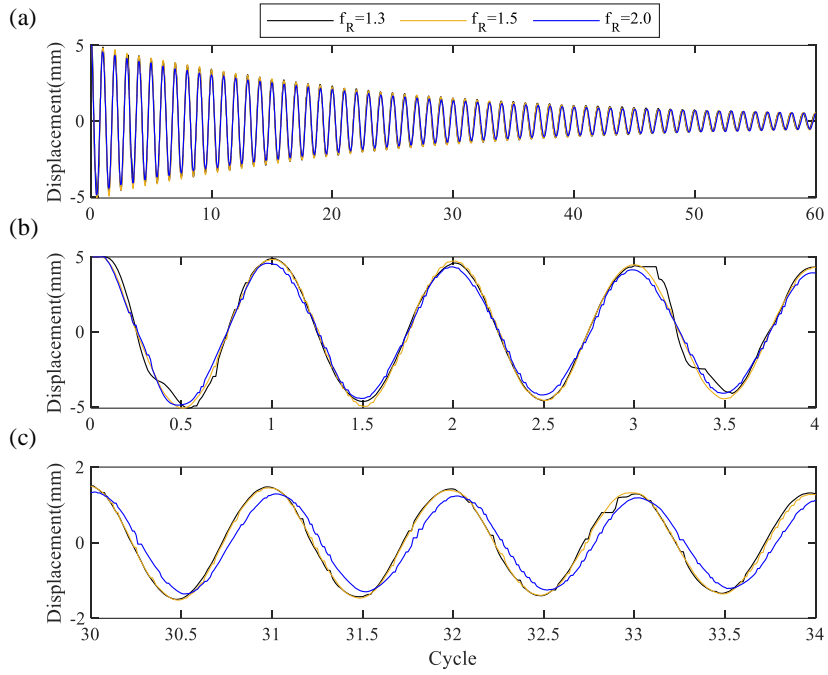


Figure 53. Responses in Displacements for Different f_R in the Vertical Direction

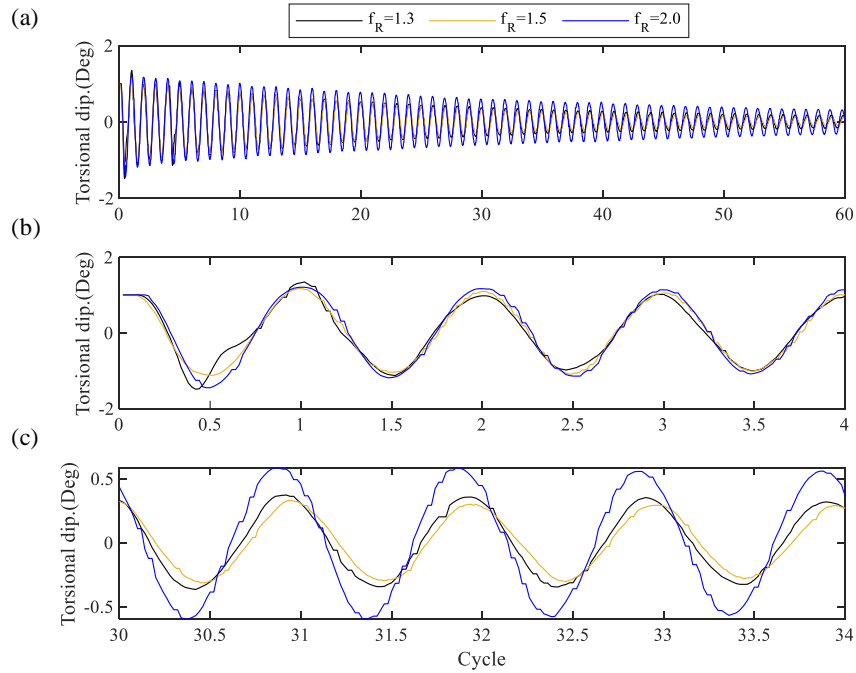
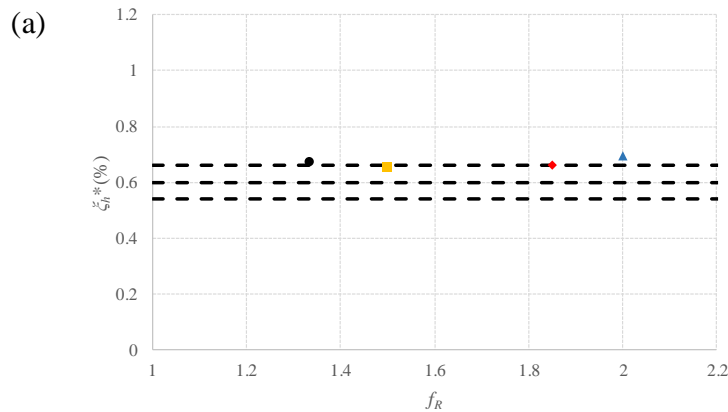


Figure 54. Responses in Torsional Displacements for Different f_R

As illustrated in Figure 53 and Figure 54, there is an error in frequencies in the vertical/torsional direction for the case of $f_R = 2.0$. For the case of $f_R = 1.3$, the results show the system response with staircase behaviors. These abnormal phenomenon does not occur for the high prescribed target frequency ratio such as the case of $f_R = 1.5$. Therefore, it is concluded that this abnormality comes from the problems of the transmissibility between the cDAQ and the host PC communication, not from the intrinsic problems of the proposed RTHS system. From the viewpoint of the realized damping ratio and the rRMSE values as illustrated in Figure 55 and Figure 56, the data values are turn out to be unstable for the case of f_R greater than 1.5. Especially, the data values are not stable for the cases of the torsional direction measurements. When the values of the target torsional frequency increase, it creates the system instability, resulting in an error with the improper positioning of a linear motor to the proposed target values. This shows a certain discrepancy in the graphs. In conclusion, the proposed RTHS system shows limitation in the practical application when the value of f_R goes beyond 1.5.



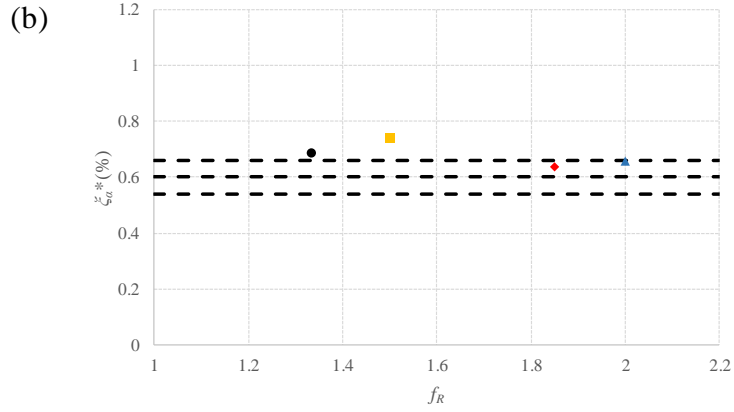


Figure 55. Realized Damping Ratios for Different f_R Frequencies for a Given Target Damping Ratio of 0.6 % (a) in the Vertical Direction and (b) in the Torsional Direction

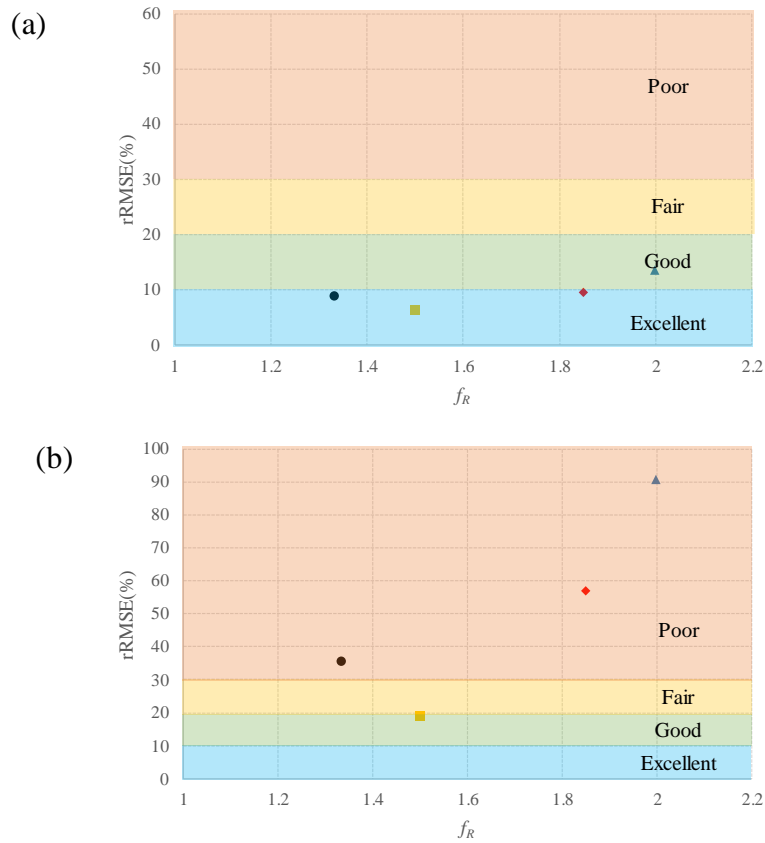


Figure 56. rRMSE Values for Different f_R Frequencies for a Given Target Damping Ratio of 0.6 % (a) in the Vertical Direction and (b) in the Torsional Direction

4.2.6 Analyses of the Results in Terms of the Velocity of the RTHS System

The self-excited term in the wind-induced force is divided into two terms; the stiffness term and the damping one. Since the damping term is related to the velocity of the system, to accurately simulate the real wind tunnel experiments, not only the displacement but also the velocity is precisely adjusted. However, only the information of the displacement is available in the proposed RTHS system. To find out the velocity of the system, the proper mathematical tool is required. In reality, the simple approach using the derivatives of the displacement with respect to time creates the errors without giving the accurate displacement values. To overcome this issue, the FDM-FIR filter (Cha, 2015) is used to reconstruct the velocity of the system. The reconstruction is done for the target accuracy α_T of 0.97 and the \tilde{p}_0 of 1.26. The vertical displacement values from the mass ratio experiments described in Section 4.2.2 and the target damping ratio experiments described in Section 4.2.3 are used to reconstruct the vertical velocity.

Figure 57 and Figure 58 illustrate the reconstructed velocity for each experimental case. Since the reconstruction process utilizes the window technique, the reconstruction process is not performed at the front and the back of the data as much as the half the size of the window size. Comparing the results of the reconstructed velocity data with the results of displacement as illustrated in Figure 35 and Figure 41, it is confirmed that the aspects are the same.

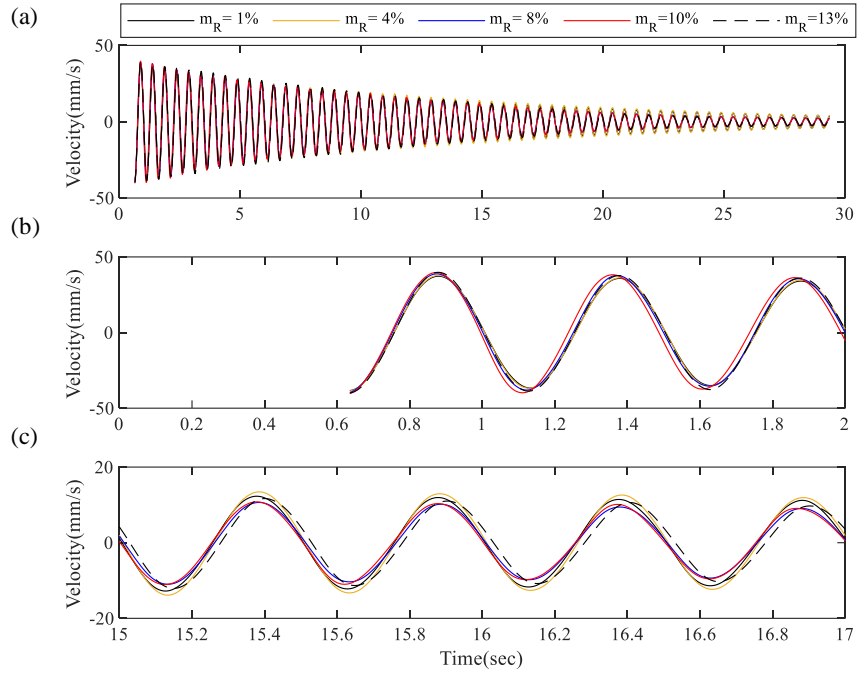


Figure 57. Velocities in the Vertical Direction for Different Values of m_R

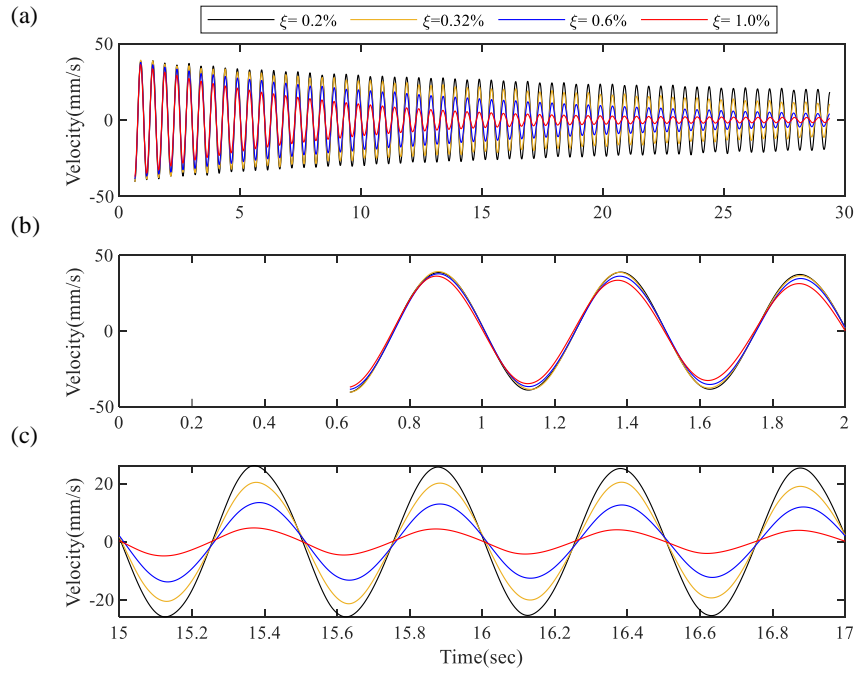


Figure 58. Responses in Velocities for Different Target Damping Ratios in the Vertical Direction

Rather, the abnormality in the displacement data such as the staircase behavior is smoothed out. Since the reconstructed velocity is estimated by the displacement, it is natural that its trend and the rRMSE values in Figure 59 and Figure 60 are similar to the results of the displacement data. Ideally, the actual velocity of the system is directly measured. However, the results from this approach show that the proposed RTHS system is also describing the velocity properly.

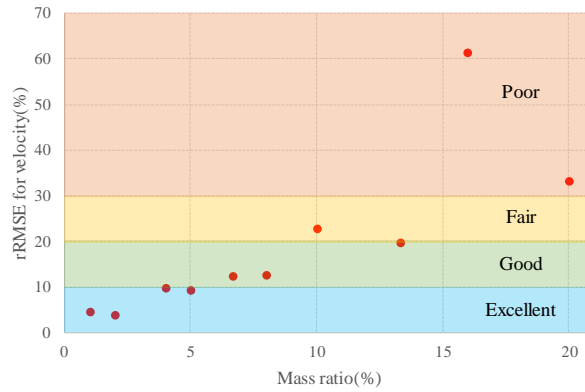


Figure 59. rRMSE Values in Terms of Velocities for Different Values of m_R for a Given Target Damping Ratios of 0.6 % in the Vertical Direction

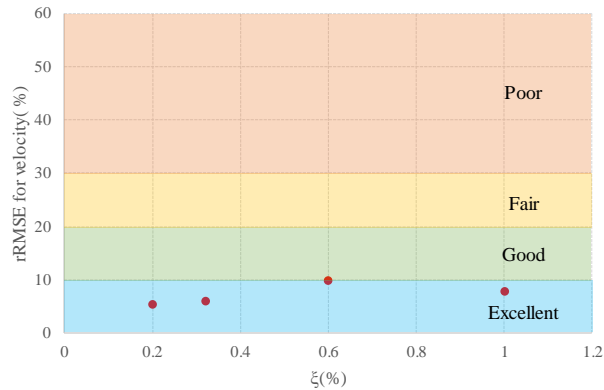


Figure 60. rRMSE Values in Terms of Velocities for Different Target Damping Ratios in the Vertical Direction

CHAPTER 5

SIMULATION OF THE VIBRATION IN WIND TUNNEL TESTS

5.1 Design of Three Experimental Cases for Simulating the Vibration in Wind Tunnel Tests

Before the real implementation of the proposed RTHS system in the wind tunnels, the final confirmation is needed to find out whether the proposed system successfully simulates the wind-induced vibrations. The typical behaviors of the bridges by wind are summarized in Figure 61.

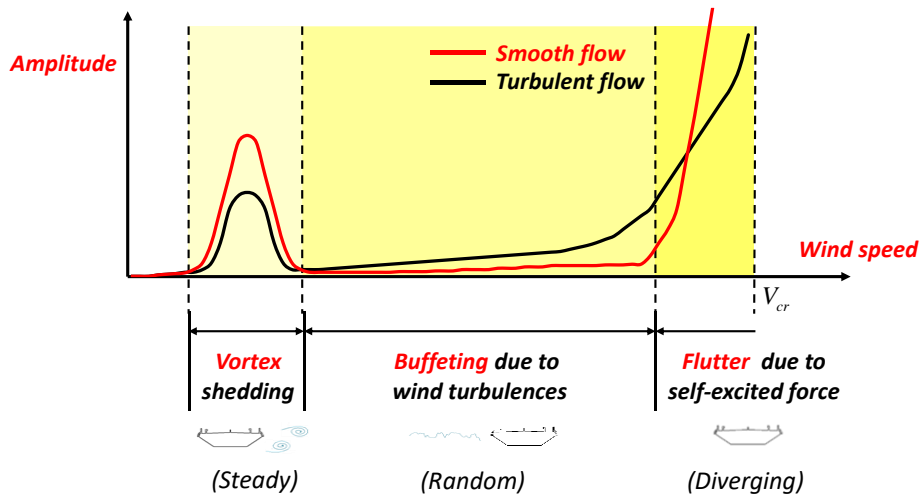


Figure 61. General Velocity-Amplitude Curves Attained in the Wind Tunnel Experiments

The simulation of the flutter phenomenon is not easy because this phenomenon is divergent vibration. However, the impact of the other vibrations such

as the VIV and the random vibration by the buffeting force are to be simulated by pre-defined force data. To check the validity of the proposed RTHS system, the following three different types of tests are proposed with proper instrument installations as depicted in Figure 62;

- 1) Free-vibration tests,
- 2) Sinusoidal force excitation tests, and
- 3) White noise force excitation tests.

The forced tests such as types (2) and (3) are expressed by the additional external force, \mathbf{F}_{ex} , in the right hand side of Eq. (38). Here the external force, \mathbf{F}_{ex} is not the actual force acting on the system. It is the imaginary force in the control program.

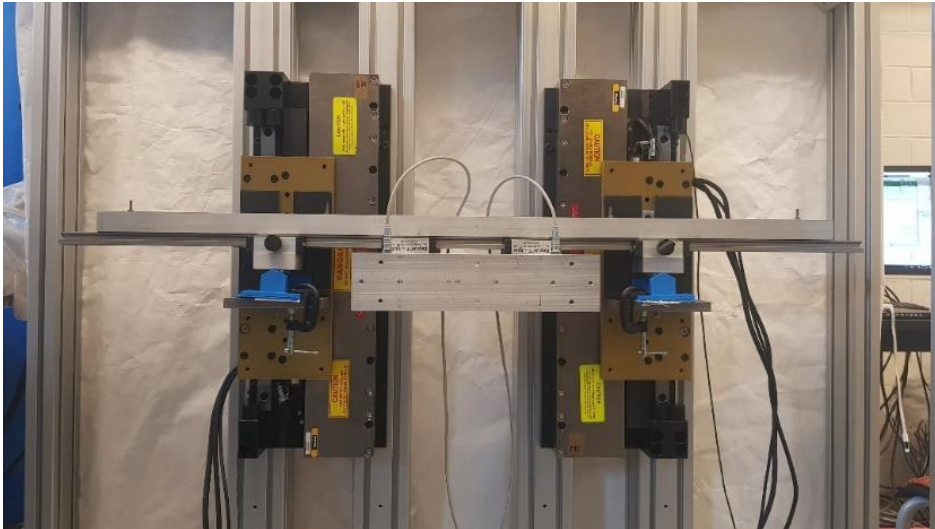


Figure 62. Setup for Simulation Tests

Throughout the proposed free-vibration tests, the general behaviors of the system by the wind are checked. The proposed second tests, the sinusoidal force excitation tests are developed to confirm the vibration behaviors of the proposed RTHS system in the steady-state after the end of transient-state vibrations. This phenomenon is studied to simulate the VIV in the wind tunnel tests. The third proposed tests, the white noise force excitation tests are designed to understand the buffeting responses by turbulent components. All the results from these tests are compared with the results from the theoretical analytical approaches with the pre-defined inputs values of \mathbf{F}_{ex} .

5.2 Simulation Cases (1): Free-vibration Tests

As explained in the previous section, to understand the general behaviors by wind, the free-vibration tests are firstly designed. Two different test cases are studies for the cases with the initial displacement and then with the initial velocity. The input parameters prescribed in the Section 4 of this study are applied for the tests.

For the case with the initial displacement, the following input parameter values are used; $m_E = 0.52 \text{ kg}$, $\bar{m}_N = 9.48 \text{ kg}$, $m_R = 5.2\%$, $\bar{\xi}_h = 0.6 \%$, $\bar{f}_h = 2 \text{ Hz}$, $I_E = 0.003 \text{ kg} \cdot \text{m}^2$, $\bar{I}_N = 0.097 \text{ kg} \cdot \text{m}^2$, $I_R = 2.5\%$, $\bar{\xi}_\alpha = 0.6 \%$, $\bar{f}_\alpha = 3 \text{ Hz}$ and $f_R = 1.5$.

The vertical initial displacement is set to be 3 mm. And for the torsional direction, its value is set to be 1 degree. The responses in the vertical and the torsional direction are illustrated in Figure 63 and Figure 64, respectively. Results show that there is good agreement between the analytical predictions and the measured values for both directions. It leads to the conclusion that the proposed RTHS system simulates the experimental environment well for the case with the initial displacement in the free-vibration tests.

For the cases with the initial velocities, the free-vibration tests are implemented with the same parameter value data set used for the cases with the initial displacements. The values of the initial velocities for this comparison tests are 30 mm/s in the vertical direction and the 28.6 deg/s in the torsional one.

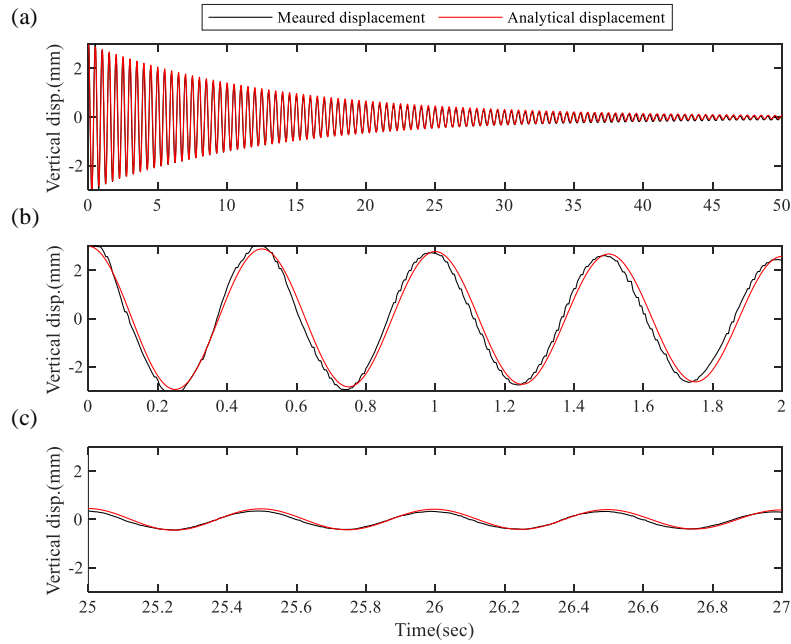


Figure 63. Comparison of Analytical and Measured Vertical Displacements in the Free-Vibration Tests (Initial Displacement)

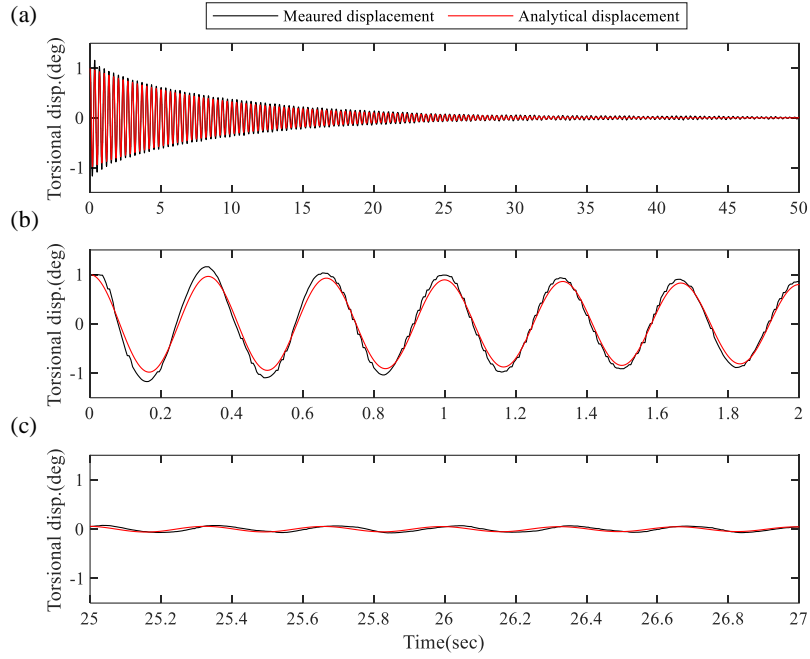


Figure 64. Comparison of Analytical and Measured Torsional Displacements in the Free-Vibration Tests (Initial Displacement)

Due to the time-delay at the early time stage, the discrepancy is witnessed between the analytical and actual measured displacements. However, when the proposed adaptive time-delay compensation method is properly functioned at the later time domain, this discrepancy disappears to eventually produce the correct results. This also confirms the validity of the proposed RTHS system is comprehensively supported by the cases with the initial velocities for the given tests.

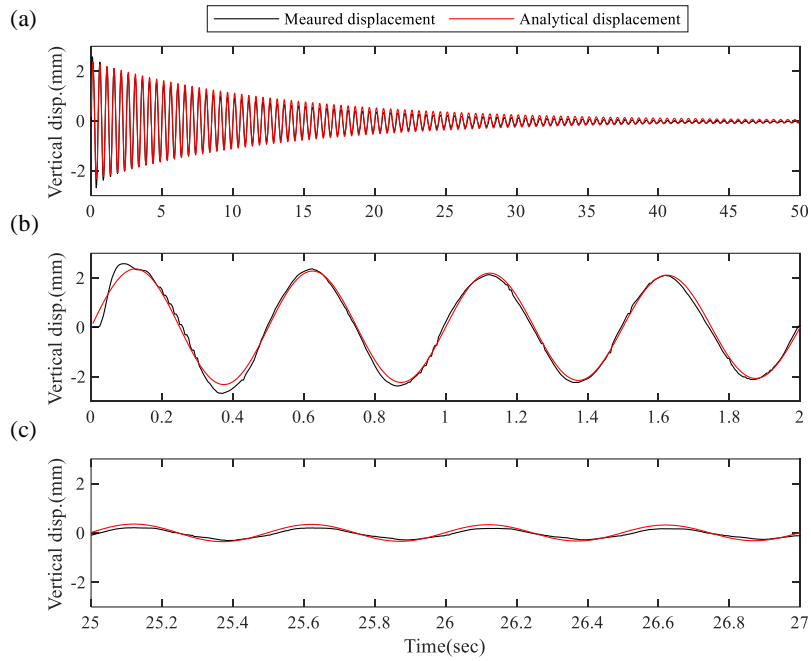


Figure 65. Comparison of Analytical and Measured Vertical Displacements in the Free-Vibration Tests (Initial Velocity)

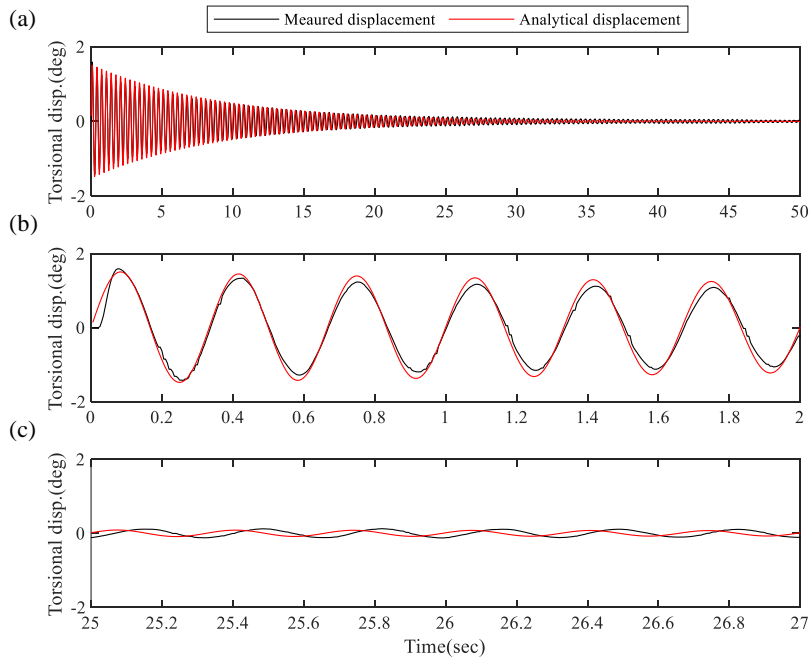


Figure 66. Comparison of Analytical and Measured Torsional Displacements in the Free-Vibration Tests (Initial Velocity)

5.3 Simulation Cases (2): Sinusoidal Force Excitation Tests

To fully confirm whether the proposed RTHS system works well to simulate the behaviors in the steady and transient states, the following sinusoidal force excitation tests are proposed. For the analytical simulations over the displacements in both vertical and torsional directions, the sinusoidal force is expressed in the term for \mathbf{F}_{ex} in the governing equation of the proposed RTHS framework system as described in Eq.(40).

$$\bar{\mathbf{M}}_N \ddot{\mathbf{U}} + \bar{\mathbf{C}} \dot{\mathbf{U}} + \bar{\mathbf{K}} \mathbf{U} = \mathbf{F}_M + \mathbf{F}_{ex} \quad (40)$$

Here the following input parameter values are used for the system analysis; $m_E = 0.52 \text{ kg}$, $\bar{m}_N = 9.48 \text{ kg}$, $m_R = 5.2 \text{ \%}$, $\bar{\xi}_h = 0.6 \text{ \%}$, $\bar{f}_h = 2 \text{ Hz}$, $I_E = 0.003 \text{ kg} \cdot \text{m}^2$, $\bar{I}_N = 0.047 \text{ kg} \cdot \text{m}^2$, $I_R = 5.0\%$, $\bar{\xi}_\alpha = 0.6 \text{ \%}$, $\bar{f}_\alpha = 3 \text{ Hz}$ and $f_R = 1.5$.

For the proper analytical simulations, the following values are added to describe the term of \mathbf{F}_{ex} in Eq.(40);

For the vertical direction, $L_{ex} = \sin(2\pi(2.5)t) \text{ [N]}$ and,

For the torsional direction, $M_{ex} = 0.05 \sin(2\pi(3.5)t) \text{ [N} \cdot \text{m]}$.

Results are depicted in Figure 67 and Figure 68. The graph (a) illustrates the results for all time domains, while the graphs in (b) and (c) are for the transient and the steady-state behaviors respectively. Results show the good agreements between the analytical and actual measured responses for both

steady and transient states. This also leads to the conclusion that the proposed RTHS system is good enough to simulate the VIV in the proposed test cases.

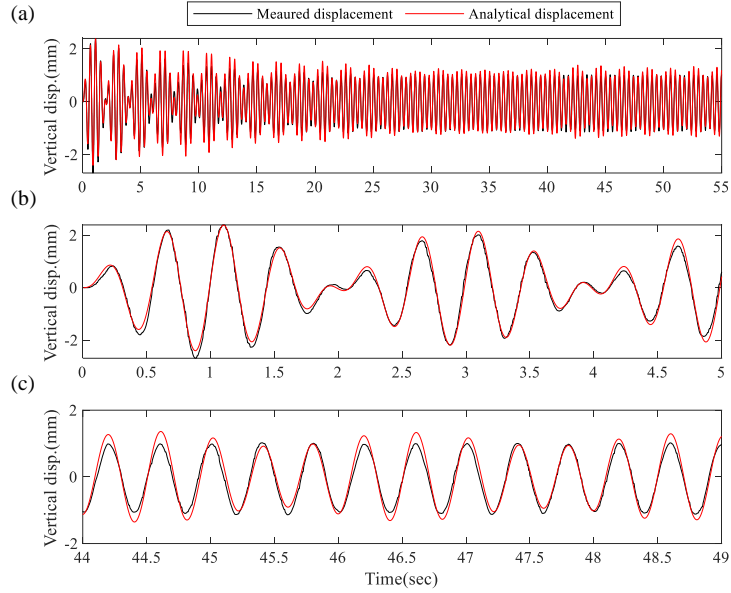


Figure 67. Comparison of Analytical and Measured Vertical Displacements in the Sinusoidal Excitation Tests

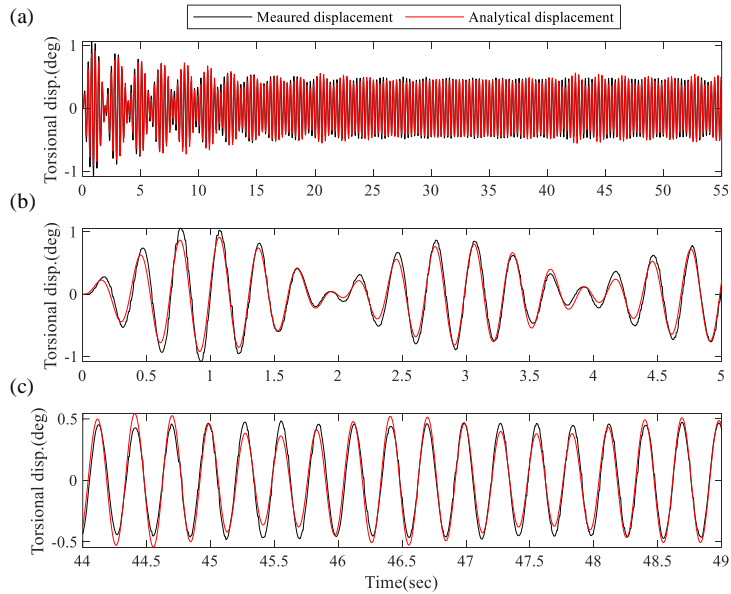


Figure 68. Comparison of Analytical and Measured Torsional Displacements in the Sinusoidal Excitation Tests

5.4 Simulation Cases (3): White Noise Force Excitation Tests

Finally, the white noise excitation tests are performed to assure the validity of the proposed RTHS system to simulate the system buffeting responses.

The following input parameter values are also used for the analytical approached; $m_E = 0.52$ kg, $\bar{m}_N = 4.48$ kg, $m_R = 2.6$ %, $\bar{\xi}_h = 0.6$ %, $\bar{f}_h = 2$ Hz, $I_E = 0.003$ kg·m², $\bar{I}_N = 0.997$ kg·m², $I_R = 0.3$ %, $\bar{\xi}_\alpha = 0.6$ %, $\bar{f}_\alpha = 3$ Hz and $f_R = 1.5$.

Similar to the approach in the Section 5.3, the pre-defined white noise force is included in the term of \mathbf{F}_{ex} . For the vertical direction, the magnitude of the white noise signal is normalized as 2 N, and for the torsional direction, the value for the signal is given as 0.5 N·m.

The general shapes of the white noise forces are illustrated in Figure 69. Results from both analytical and the actual measurements are summarized in Figure 70 and Figure 71. As expected, there is no significant discrepancy between the analytical and the measured data for both vertical and torsional directions.

The final conclusions from the series of the three test cases with three different forces support the validity of the proposed RTHS system for the actual simulations of the future wind tunnel tests.

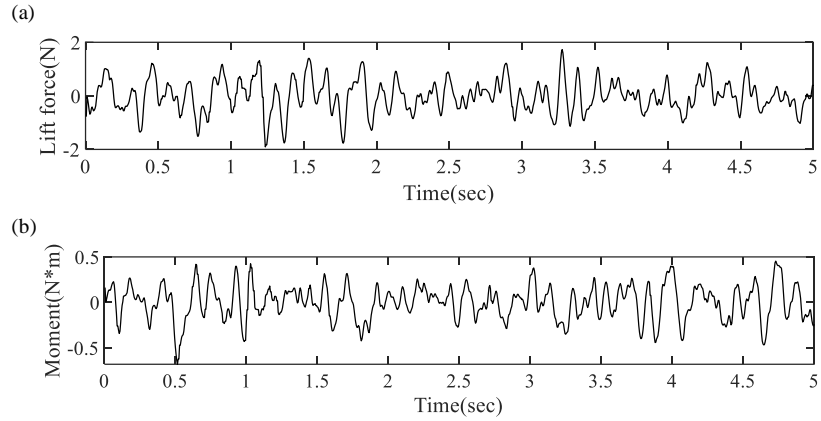


Figure 69. White Noise Signals for Simulation Case 3 (a) Lift Force (b) Moment

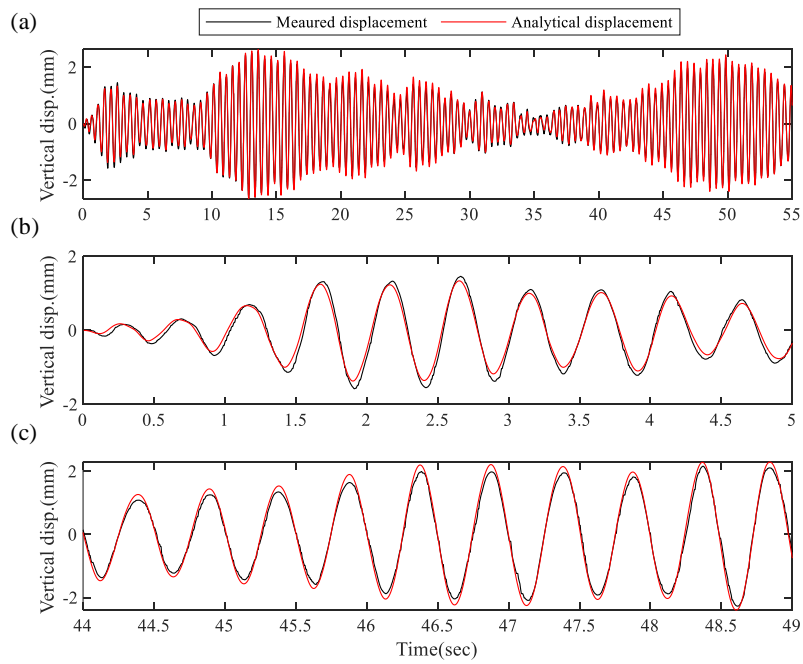


Figure 70. Comparison of Analytical and Measured Vertical Displacements in the White Noise Excitation Tests

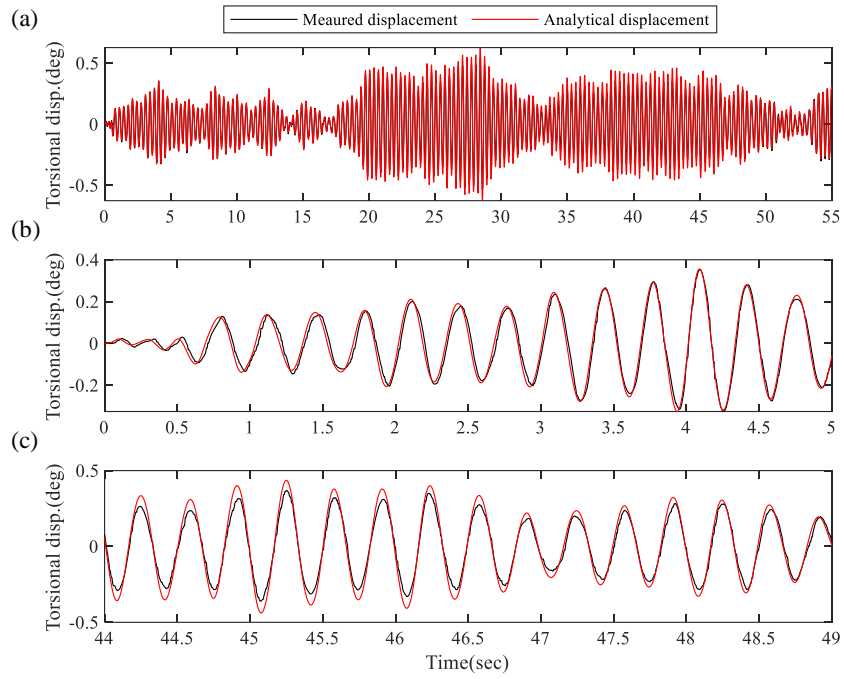


Figure 71. Comparison of Analytical and Measured Torsional Displacements in the White Noise Excitation Tests

CHAPTER 6

CONCLUSIONS AND RECOMMENDATIONS FOR FURTHER STUDY

The concepts of the proposed RTHS system are valuable to overcome the limitations in the existing wind tunnel tests. The proposed RTHS system in this dissertation is the practical solution to simulate the wind tunnel experiments. It has two distinct features. Firstly, by applying the RTHS system to the wind tunnel experiments, the actual precise values of the wind-induced forces are directly measured through the vibration tests without any assumptions. Secondly, the dynamic parameter values are precisely prescribed without traditional trial-error approaches.

To verify whether the proposed RTHS system is the viable option for simulations of the wind tunnel tests, the numerical simulations are performed. The feasibility of the procedure of the RTHS system is checked by the results from the traditional aeroelastic analysis. The proper capacity of the experimental apparatus is determined by the results from numerical analysis for the worst-case scenarios. In this analysis, the time-delay of the total system is compensated with the adaptive time-delay compensation method proposed by Chen et al. This approach is applied to compensate the effect of the systematic time-delay at the level of 34 ms in the proposed RTHS system.

For the real applications of the RTHS system, it is necessary to identify the available range of system input parameter values. In this mission, the series

of experiments are performed. Experiment results show that the proposed RTHS system works adequately well with consistent stabilities with the parameters value ranges of $M_R=6.1$ to 8% , $I_R = 0.4$ to 7.0% , $\bar{\xi}=0.2$ to 1.0% , $\bar{f}_h=2$ to 3 Hz, $\bar{f}_\alpha= 3$ to 4 Hz, and f_R up to 1.5 .

To assure whether the proposed RTHS system simulates the wind-induced vibrations for given parameter value ranges, the following three cases are examined; (1) Free-vibration test cases, (2) Sinusoidal force excitation test cases, and (3) White noise force excitation test cases. In these three case studies, the free vibration, VIV, and the buffeting responses are assumed for each study to find out whether the RTHS system simulates the wind-induced vibration correctly. Results clearly show that the proposed RTHS system is a viable approach to accurately simulate the wind tunnel tests.

Many potential applications of the RTHS system are proposed. Firstly, the new approach is practical to simulate the actual damper, traditionally known to be difficult to be simulated by the proper experimental apparatus. Secondly, the new concept is applicable to simulate the responses from the wind tunnel tests under the multi-mode conditions. Thirdly, the new system is valid to assess the responses from the multi-mode buffeting responses in association with the application of an Active Turbulence Generator (ATG).

To improve the performance of the proposed RTHS system analysis, the following subjects are recommended for the future studies.

Firstly, it will be ideal to eliminate all non-deterministic aspects in the system. By connecting a cDAQ and a motor driver directly, the removal of the non-deterministic elements in the computer system is needed while assuring the stabilization of the experimental systems.

Secondly, as discussed in the main text of this dissertation, it is highly recommended to minimize the values of three factors in the time-delay. Among the three factors that cause the time-delay, the one initiated by the LabVIEW program and the connection between the cDAQ and the host PC is easily reduced. If the time-delay is reduced, a higher target natural frequency is applicable in the proposed RTHS system.

Thirdly, it is important to reduce the impact of the inertia forces. If the pressure, instead of the load, is measured, the inertia forces do not affect the responses from the RTHS system. Measuring the net wind-induced force enhances the more precise simulations of the proposed RTHS system analysis for the wind tunnel tests.

Fourthly, it is recommended to switch the motor control method from the position control one to the velocity/acceleration control one. When the motor is adjusted with the position control, the actual speed and the acceleration are not rigorously simulated. Since the aeroelastic damping term is related to the velocity, it is necessary to change the control loop to avoid any further side effect from the time-delay.

REFERENCES

- Agar, T. J. A. (1989). Aerodynamic Flutter Analysis of Suspension Bridges by a Modal Technique. *Engineering Structures*, 11(2), 75-82.
- Bisplinghoff, R. L., & Ashley, H. (2013). *Principles of aeroelasticity*: Courier Corporation.
- BogunovićJakobsen, J., & Hjorth-Hansen, E. (1995). Determination of the aerodynamic derivatives by a system identification method. *Journal of Wind Engineering and Industrial Aerodynamics*, 57(2-3), 295-305.
- Borri, C., & Hoffer, R. (2000). Aeroelastic wind forces on flexible bridge girders. *Meccanica*, 35(1), 1-15.
- Brownjohn, J. M. W., & Jakobsen, J. B. (2001). Strategies for aeroelastic parameter identification from bridge deck free vibration data. *Journal of Wind Engineering and Industrial Aerodynamics*, 89(13), 1113-1136.
- Bucher, C. G., & Lin, Y. K. (1988). Stochastic Stability of Bridges Considering Coupled Modes. *Journal of Engineering Mechanics-Asce*, 114(12), 2055-2071.
- Cao, B. C., & Sarkar, P. P. (2012). Identification of Rational Functions using two-degree-of-freedom model by forced vibration method. *Engineering Structures*, 43, 21-30.
- Cha, S. H. (2015). *Extraction of Flutter Derivatives Based on the Force Controlled Forced Vibration Test*. Seoul National University,
- Chae, Y., et al. (2013). Adaptive time series compensator for delay compensation of servo-hydraulic actuator systems for real-time hybrid

- simulation. *Earthquake Engineering & Structural Dynamics*, 42(11), 1697-1715.
- Chen, C., & Ricles, J. M. (2009). Analysis of actuator delay compensation methods for real-time testing. *Engineering Structures*, 31(11), 2643-2655.
- Chen, C., & Ricles, J. M. (2010). Tracking Error-Based Servohydraulic Actuator Adaptive Compensation for Real-Time Hybrid Simulation. *Journal of Structural Engineering-Asce*, 136(4), 432-440.
- Chen, C., et al. (2012). Improved Adaptive Inverse Compensation Technique for Real-Time Hybrid Simulation. *Journal of Engineering Mechanics-Asce*, 138(12), 1432-1446.
- Chen, X. H., et al. (2000). Aerodynamic coupling effects on flutter and buffeting of bridges. *Journal of Engineering Mechanics-Asce*, 126(1), 17-26.
- Chen, X. Z., & Kareem, A. (2002). Advances in modeling of aerodynamic forces on bridge decks. *Journal of Engineering Mechanics-Asce*, 128(11), 1193-1205.
- Chen, Z. Q., et al. (2005). Wind-induced self-excited loads on bridges. *Journal of Structural Engineering-Asce*, 131(12), 1783-1793.
- Chowdhury, A. G., & Sarkar, P. P. (2003). A new technique for identification of eighteen flutter derivatives using a three-degree-of-freedom section model. *Engineering Structures*, 25(14), 1763-1772.

- Costa, C., & Borri, C. (2006). Application of indicial functions in bridge deck aeroelasticity. *Journal of Wind Engineering and Industrial Aerodynamics*, 94(11), 859-881.
- Davenport, A. G. (1962). Buffeting of a suspension bridge by storm winds. *Journal of the Structural Division*, 88(3), 233-270.
- Despotovic, M., et al. (2016). Evaluation of empirical models for predicting monthly mean horizontal diffuse solar radiation. *Renewable & Sustainable Energy Reviews*, 56, 246-260.
- Diana, G., et al. (2004). Forced motion and free motion aeroelastic tests on a new concept dynamometric section model of the Messina suspension bridge. *Journal of Wind Engineering and Industrial Aerodynamics*, 92(6), 441-462.
- Diana, G., et al. (2010). Aerodynamic instability of a bridge deck section model: Linear and nonlinear approach to force modeling. *Journal of Wind Engineering and Industrial Aerodynamics*, 98(6-7), 363-374.
- Diana, G., et al. (2014). Wind tunnel: a fundamental tool for long-span bridge design. *Structure and Infrastructure Engineering*, 11(4), 533-555.
- Ding, Q., & Lee, P. K. K. (2000). Computer simulation of buffeting actions of suspension bridges under turbulent wind. *Computers & Structures*, 76(6), 787-797.
- Dowell, E. H., et al. (1989). *A modern course in aeroelasticity* (Vol. 3): Springer.

- Falco, M., et al. (1992). Nonlinear Effects in Sectional Model Aeroelastic Parameters Identification. *Journal of Wind Engineering and Industrial Aerodynamics*, 42(1-3), 1321-1332.
- Han, Y., et al. (2014). Experimental study on aerodynamic derivatives of a bridge cross-section under different traffic flows. *Journal of Wind Engineering and Industrial Aerodynamics*, 133, 250-262.
- Hirata, I., et al. (2003). *New Hybrid Vibration Technique for Simulating Aerodynamic Vibration of Structures in a Wind Tunnel*: Nihon University.
- Huang, L., et al. (2009). Numerical simulation for aerodynamic derivatives of bridge deck. *Simulation Modelling Practice and Theory*, 17(4), 719-729.
- Jain, A., et al. (1996). Coupled flutter and buffeting analysis of long-span bridges. *Journal of Structural Engineering-Asce*, 122(7), 716-725.
- Jensen, A. G. (1997). Fluid dynamic derivatives: Marine and wind engineering approaches. *Journal of Wind Engineering and Industrial Aerodynamics*, 71, 777-793.
- Jung, K., et al. (2011). Evaluation of impulse response functions for convolution integrals of aerodynamic forces by optimization with a penalty function. *Journal of Engineering Mechanics*, 138(5), 519-529.
- Kanda, M., et al. (2006). "Numerical integration scheme for hybrid vibration technique—explicit scheme equivalent to unconditionally stable. *Journal of Wind Engineering and Industrial Aerodynamics*, 31, 1.

- Kato, Y., & Kanda, M. (2014). Development of a modified hybrid aerodynamic vibration technique for simulating aerodynamic vibration of structures in a wind tunnel. *Journal of Wind Engineering and Industrial Aerodynamics*, 135, 10-21.
- Katsuchi, H., et al. (1999). Multimode coupled flutter and buffeting analysis of the Akashi-Kaikyo bridge. *Journal of Structural Engineering-Asce*, 125(1), 60-70.
- Kim, H. K., et al. (2004). Geometrically nonlinear buffeting response of a cable-stayed bridge. *Journal of Engineering Mechanics*, 130(7), 848-857.
- Larsen, A., & Walther, J. H. (1998). Discrete vortex simulation of flow around five generic bridge deck sections. *Journal of Wind Engineering and Industrial Aerodynamics*, 77-8, 591-602.
- Li, M.-F., et al. (2013). General models for estimating daily global solar radiation for different solar radiation zones in mainland China. *Energy conversion and management*, 70, 139-148.
- Li, Q. C. (1995). Measuring Flutter Derivatives for Bridge Sectional Models in Water Channel. *Journal of Engineering Mechanics-Asce*, 121(1), 90-101.
- Lin, Y. K., & Yang, J. N. (1983). Multimode Bridge Response to Wind Excitations. *Journal of Engineering Mechanics-Asce*, 109(2), 586-603.
- Mannini, C., & Bartoli, G. (2008). *Investigation on the dependence of bridge deck flutter derivatives on steady angle of attack*. Paper presented at the Proc., BBAA VI Int. Colloquium on Bluff Bodies Aerodynamics and Applications.

- Matsumoto, M. (1996). Aerodynamic damping of prisms. *Journal of Wind Engineering and Industrial Aerodynamics*, 59(2-3), 159-175.
- Matsumoto, M., et al. (1993). Aerodynamic Derivatives of Coupled/Hybrid Flutter of Fundamental Structural Sections. *Journal of Wind Engineering and Industrial Aerodynamics*, 49(1-3), 575-584.
- Mercan, O., & Ricles, J. M. (2007). Stability and accuracy analysis of outer loop dynamics in real-time pseudodynamic testing of SDOF systems. *Earthquake Engineering & Structural Dynamics*, 36(11), 1523-1543.
- Mosqueda, G., et al. (2007). Real-time error monitoring for hybrid simulation. Part II: Structural response modification due to errors. *Journal of Structural Engineering-Asce*, 133(8), 1109-1117.
- Neuhaus, C., et al. (2009). *Identification of 18 Flutter Derivatives by Forced Vibration Tests: A New Experimental Rig*. Paper presented at the 5th European & African conference on wind engineering: Florence Italy, July 19th-23rd 2009: conference proceedings.
- Noda, M., et al. (2003). Effects of oscillation amplitude on aerodynamic derivatives. *Journal of Wind Engineering and Industrial Aerodynamics*, 91(1-2), 101-111.
- Ogawa, K., et al. (2002). Aerodynamic characteristics of a 2-box girder section adaptable for a super-long span suspension bridge. *Journal of Wind Engineering and Industrial Aerodynamics*, 90(12-15), 2033-2043.
- Park, J., et al. (2013). Exact Enforcement of the Causality Condition on the Aerodynamic Impulse Response Function Using a Truncated Fourier Series. *Journal of Engineering Mechanics*, 140(5), 04014017.

- RH Scanlan, J. T. (1971). Airfoil and bridge deck flutter derivatives.
- Sarkar, P. P., et al. (2009). Comparative and sensitivity study of flutter derivatives of selected bridge deck sections, Part 1: Analysis of inter-laboratory experimental data. *Engineering Structures*, 31(1), 158-169.
- Sarkar, P. P., et al. (1994). Identification of Aeroelastic Parameters of Flexible Bridges. *Journal of Engineering Mechanics-Asce*, 120(8), 1718-1742.
- Sarwar, M. W., et al. (2008). Prediction of aerodynamic characteristics of a box girder bridge section using the LES turbulence model. *Journal of Wind Engineering and Industrial Aerodynamics*, 96(10-11), 1895-1911.
- Scanlan, R. (1978a). The action of flexible bridges under wind, I: flutter theory. *Journal of Sound and Vibration*, 60(2), 187-199.
- Scanlan, R. (1978b). The action of flexible bridges under wind, II: Buffeting theory. *Journal of Sound and Vibration*, 60(2), 201-211.
- Scanlan, R. H. (1993). Problematics in Formulation of Wind-Force Models for Bridge Decks. *Journal of Engineering Mechanics-Asce*, 119(7), 1353-1375.
- Scanlan, R. H., & Jones, N. P. (1990). Aeroelastic Analysis of Cable-Stayed Bridges. *Journal of Structural Engineering-Asce*, 116(2), 279-297.
- Scanlan, R. H., & Tomo, J. (1971). Air foil and bridge deck flutter derivatives. *Journal of Soil Mechanics & Foundations Div.*
- Siedziako, B., et al. (2017). An enhanced forced vibration rig for wind tunnel testing of bridge deck section models in arbitrary motion. *Journal of Wind Engineering and Industrial Aerodynamics*, 164, 152-163.

Strømmen, E. (2010). *Theory of bridge aerodynamics*: Springer Science & Business Media.

Thang, N. D., et al. (2008). Effects of approximation of self-excited forces by rational function on wind-induced response of a long-span bridge. *Journal of Structural Engineering, A*, 54, 420-428.

Theodorsen, T., & Mutchler, W. (1935). General theory of aerodynamic instability and the mechanism of flutter.

von Karman, T. (1948). Progress in the Statistical Theory of Turbulence. *Proc Natl Acad Sci U S A*, 34(11), 530-539.

Wu, T., & Song, W. (2019). Real-time aerodynamics hybrid simulation: Wind-induced effects on a reduced-scale building equipped with full-scale dampers. *Journal of Wind Engineering and Industrial Aerodynamics*, 190, 1-9.

Zhu, Z. W., et al. (2007). Wind tunnel and CFD study on identification of flutter derivatives of a long-span self-anchored suspension bridge. *Computer-Aided Civil and Infrastructure Engineering*, 22(8), 541-554.

초 록

황유찬

건설환경공학부

서울대학교 대학원

장대 교량의 내풍 안정성을 평가하기 위한 방법으로 일반적으로 해석적/실험적 방법이 사용된다. 해석적 방법은 바람에 의한 힘을 정의하기 위해 Scanlan 이 정의한 플러터 이론과 같은 가정을 사용하게 된다. 그러나, 가정으로 인한 부정확성과 문제점이 발견되고 있어 정확한 내풍안정성 평가를 위해 풍동 실험이 추천된다. 하지만, 풍동 실험 또한 진동 실험 당시의 힘을 동시에 측정하지 못하고 시스템의 동적 특성치를 정확하게 세팅하지 못하는 한계를 지니고 있다.

실시간 하이브리드 시스템은 기존의 풍동 실험이 가지고 있는 한계를 극복할 수 있는 방안을 제시한다. 풍동에 적용되는 제안하는 실시간 하이브리드 시스템은 수치 모델로 구성하기 힘든 바람에 의한 힘은 직접 실험을 통해 측정하고 나머지 부분은 수치적으로 구현하는 방식을 사용한다. 이렇게 함으로써 바람에 의해 발생하는 힘은 정확히 측정할 수 있으며 시스템의 동적 특성치 또한 정확하게 세팅할 수 있다.

실시간 하이브리드 시스템 장치를 직접 구성하기 전에 하이브리드 시스템 자체가 유효한지를 수치 시뮬레이션을 통해 검증하였다. 제 2 진도대교 단면을 활용하여 공탄성 해석과 수치 시뮬레이션을 통해 장치의 유효성을 검증하였다.

실제 실시간 하이브리드 시스템 장치는 네 개의 리니어 모터와 로드셀, 프레임 시스템과 구동 프로그램으로 구성된다. 극한 케이스 해석을 통해 리니어 모터, 로드셀의 용량을 결정하였다. 시스템 구동을 위한 프로그램은 수치 적분 프로그램, 시간지연 보상 프로그램, PID 컨트롤 프로그램을 합쳐서 구성하였다. 장치의 총 시간 지연은 34 ms 으로 측정되었으며 adaptive compensation approach 를 사용하여 보정하였다.

실제 구성한 실시간 하이브리드 시스템 장치가 기존의 풍동 실험에서 사용하는 동적 특성치를 어디까지 구현할 수 있는지 확인하는 실험을 진행하였다. 질량, 감쇠, 고유 진동수 수치를 바꿔가며 실험을 진행하였다. 시스템의 시간 지연 정도가 34 ms 로 크기 때문에 기존의 풍동에서 사용하던 동적 특성 범위를 모두 만족시키지는 못하지만 실험 가능한 범위 내에서 수치 해석 결과에 상응하는 움직임은 보이는 것을 확인하였다.

자유 진동, 주기 함수 힘 가진, 랜덤한 힘 가진 실험을 통해 풍동내에서의 교량데크의 일반적인 거동, 와류 진동, 버페팅

진동을 묘사하는 실험을 하였으며 이 또한 변위 결과가 수치 해석 결과와 다르지 않은 움직임을 보이는 것을 확인하였다. 따라서, 개발한 실시간 하이브리드 실험 장치가 확인한 범위내에서 2 차원 풍동 실험을 잘 묘사할 수 있음을 확인하였다.

주요어: 실시간 하이브리드 시스템; 교량데크; 풍동실험; 공탄성해석; 시간지연 보상

Student Number: 2011-21008